Université de Montréal

Atlas numérique spatio-temporel des artères coronaires

par

Denis Sherknies

Département d'informatique et de recherche opérationnelle
Faculté des arts et des sciences

Thèse présentée à la Faculté des études supérieures
en vue de l'obtention du grade de
Philosophiae Doctor (Ph.D.)
en informatique

Décembre, 2003

Université de Montréal

Faculté des études supérieures

Cette thèse intitulée :

Atlas numérique spatio-temporel des artères coronaires

présentée par

Denis Sherknies

a été évaluée par un jury composé des personnes suivantes:

Sébastien Roy
(président-rapporteur)

Jean Meunier
(directeur de recherche)

Jean-Claude Tardif
(codirecteur)

Neil Stewart
(membre du jury)

Denis Laurendeau
(examinateur externe)

Gilles Beaudoin
(représentant du doyen de la FES)

RÉSUMÉ

Le présent travail de recherche tente de répondre à la question : comment réaliser une reconstruction vasculaire tridimensionnelle à partir d'une seule vue ? Traditionnellement, la reconstruction 3D est réalisée à partir d'appareil d'imagerie biplan, mais ces appareils sont coûteux, de manipulation difficile et de disponibilité limitée en milieu clinique. Bien que l'information de profondeur soit inexistante sur une image bidimensionnelle, notre approche permet de la récupérer à l'aide de connaissances *a priori* du sujet à l'étude. La reconstruction 3D est abordée dans deux contextes différents.

Premièrement, dans un contexte où l'on réalise une reconstruction 3D des artères coronaires à partir de cinéangiographies monoplans. L'information *a priori* servant à la reconstruction 3D provient ici d'un modèle de l'arbre coronarien établi à l'aide de mesures biométriques réalisées par Dodge *et al.* (J.T. Dodge *et al.*, 1986, 1992). En ajoutant une composante temporelle à la reconstruction spatiale, on peut ainsi suivre et quantifier l'amplitude des contractions cardiaques à partir du mouvement de l'arbre coronarien.

Deuxièmement, la reconstruction 3D à partir d'une seule vue, est réalisée dans un contexte de fusion de deux modalités d'imagerie médicale, à savoir l'imagerie par ultrason IVUS (IntraVascular UltraSound) et l'angiographie. On se sert de l'information sur la forme du transducteur IVUS, l'information *a priori*, afin de reconstruire en 3D le chemin emprunté par la caméra IVUS à partir des images angiographiques monoplans. Une fois le chemin connu, les images IVUS peuvent être alignées de façon absolue, ce qui permet de faire des mesures précises sur l'étendue des plaques d'athérosclérose, par exemple.

Mots clés : Angiographie monoplan, coronarographie, fraction d'éjection, IVUS, modèle 3D, reconstruction 3D.

ABSTRACT

This thesis tries to answer the question : how to carry out a three-dimensional vascular reconstruction from a single view only ? Traditionally, 3D reconstructions are realized from biplane imagery apparatus, but these apparatus are complicated to operate and are not always available in many clinical centres. Although depth information is non-existent on a two-dimensional image, by using *a priori* knowledge of the subject under study our approach makes it possible to recover it. Two different contexts are addressed for 3D reconstruction.

Firstly, we consider the context where 3D reconstruction is applied to coronary arteries from single-plane cineangiography. In this case, the *a priori* information comes from a model of the coronary tree created from biometric measurements carried out by Dodge *et al.* (J.T. Dodge *et al.*, 1986, 1992). By adding a temporal component to the spatial reconstruction, it becomes possible to follow and quantify the amplitude of cardiac contractions from the coronary tree movements.

Secondly, single-plane 3D reconstruction is carried out in the fusion of two medical imaging modalities context, namely IVUS (IntraVascular UltraSound) and angiography imaging. The shape of the IVUS transducer, which is known *a priori*, is used to do the 3D reconstruction of the IVUS catheter pullback path from single-plane angiography. Once geometrically aligned perpendicularly to the catheter path, precise measures on atherosclerotic plaque extents can be made on the IVUS images.

Keywords : 3D model, 3D reconstruction, coronarography, ejection fraction, IVUS, single-plane angiography.

TABLE DES MATIÈRES

LISTE DES FIGURES

LISTE DES TABLES

REMERCIEMENTS

Je souhaite grandement remercier mon directeur Monsieur Jean Meunier pour son appui, ses encouragements et ses conseils judicieux tout au long de cette thèse. Je remercie beaucoup mon codirecteur Monsieur Jean-Claude Tardif pour son aide et son efficacité.

Je désire remercier le personnel de ICM (Institut de Cardiologie de Montréal) : les techniciennes Colette Desjardins et Joanne Vincent, l'ingénieur Pierre Le Guyader et sans oublier le Dr Jacques Lesperance sans qui l'acquisition d'images médicales n'aurait pas été possible.

Je remercie spécialement le Dr J. Theodore Dodge Jr., pour avoir si généreusement partagé ses données qui représentent un des principaux éléments de la présente thèse.

Un merci immense va à ma famille, que j'ai dû délaisser quelque peu pour effectuer ce travail. Mes enfants Lydia et Alexis, et ma conjointe Pauline, sans qui cette thèse n'aurait pas vu le jour.

À mes parents et

à ma famille Lydia, Alexis et Pauline.

Chapitre 1

INTRODUCTION

Le leitmotiv qui sous-tend ce travail de recherche consiste en la recherche d'un moyen qui redonnerait à un sujet apparaissant sur une image photographique, ses caractéristiques tridimensionnelles. Plus spécifiquement, le sujet est le réseau vasculaire des artères coronaires et les images photographiques sont des radiographies.

La preuve n'est plus à faire quant à l'utilité de la représentation 3D en imagerie médicale. Que ce soit par la conception de nouveaux appareils d'imagerie 3D, comme l'IVUS 3D, la résonnance magnétique 3D ou par l'importance de la recherche dans ce domaine.

Dans la littérature, la grande majorité des méthodes de reconstruction 3D reposent sur l'utilisation de caméras biplan ou de caméra monoplan à rotation. Dans ces cas on réalise la reconstruction 3D en faisant la correspondance entre 2 ou plusieurs images à l'aide de la géométrie épipolaire développée par Faugeras [21]. Ce qui est novateur dans le présent travail de recherche, c'est la réalisation de reconstructions 3D vasculaires fait uniquement à partir d'une seule vue.

L'approche utilisée pour réaliser une reconstruction 3D à partir d'images 2D, consiste en l'utilisation de connaissances *a priori* du sujet. Cette approche est appliquée dans 2 contextes différents : la reconstruction 3D du réseau coronarien et la reconstruction 3D du chemin parcouru lors du retrait d'une caméra IVUS des artères coronaires.

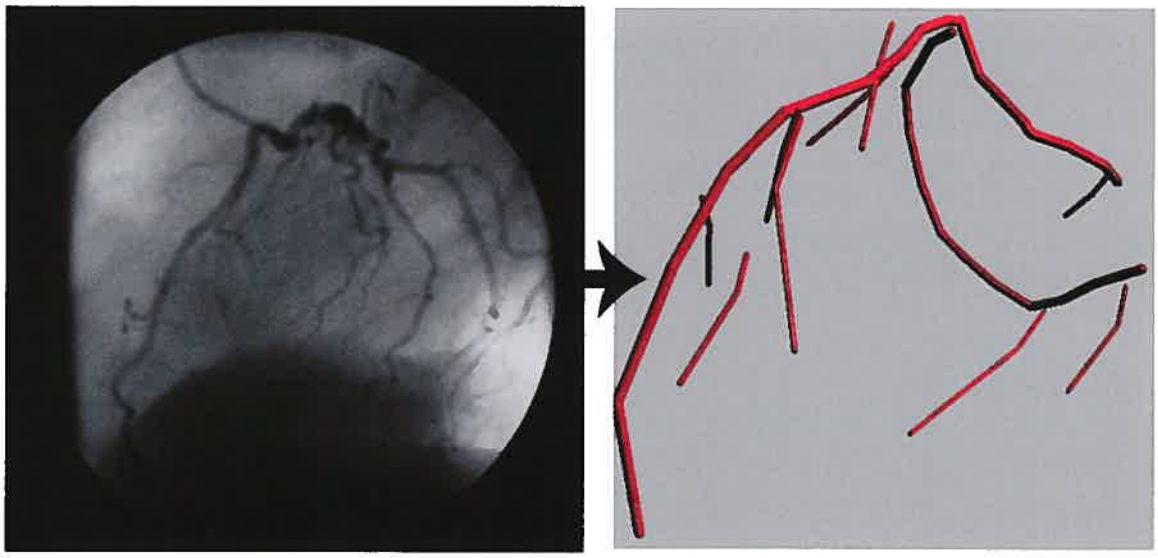

FIG. **1.1. Reconstruction 3D des artères coronaires.**

Reconstruction 3D du réseau coronarien

Dans cette section, la reconstruction 3D des artères coronaires (Fig. 1.1) faite à partir d'images cinéangiographiques monoplans, est réalisée à l'aide d'un modèle de l'arbre coronarien. Le modèle représente une généralisation d'un ensemble de mesures réalisées par Dodge *et al.* [17, 16] sur la localisation 3D de divers points de repère anatomiques sur l'arbre coronarien.

En réalisant une reconstruction 3D de chacune des images cinéangiographiques, on peut suivre l'évolution des amplitudes des contractions cardiaques dans le temps. Un parallèle est ainsi fait entre notre méthode du suivi des contractions et la fraction d'éjection, mesure déterminée grâce à la ventriculographie pour caractériser la fonction cardiaque.

Reconstruction 3D du chemin de caméra IVUS

L'imagerie ultrasonore endovasculaire présente une information complémentaire à ce que peut apporter l'angiographie, quant à l'état du réseau vasculaire. Faire la

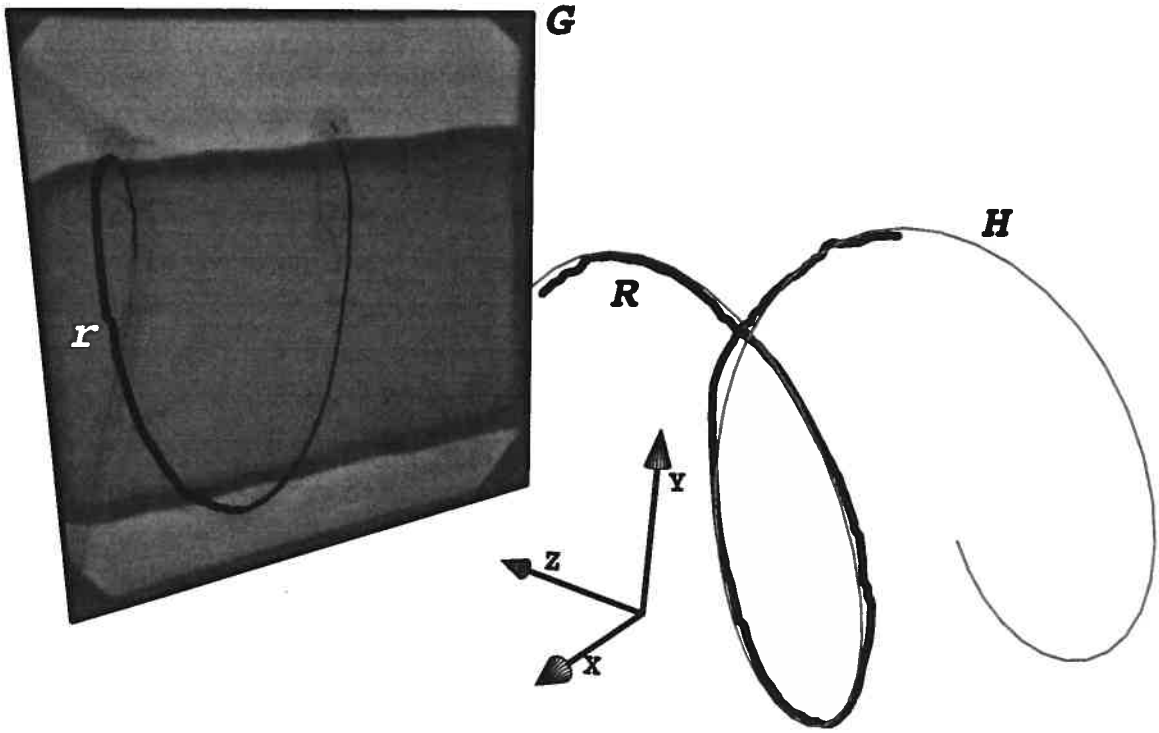

FIG. 1.2. **Reconstruction 3D du chemin parcouru par la caméra IVUS. G : angiogramme ; H : modèle hélicoïdal ; r : mesures 2D du déplacement du transducteur ; R : reconstruction 3D.**

reconstruction 3D du chemin parcouru par la caméra permet d'orienter de façon absolue les images IVUS en prenant en considération la courbure des vaisseaux. Les mesures effectuées à partir des images IVUS en sont ainsi d'autant plus précises.

La reconstruction 3D du chemin de la caméra IVUS ce fait ici aussi à partir d'images cinéangiographiques monoplans, où l'on enregistre le retrait de la caméra IVUS, Fig. 1.2. L'information *a priori*, permettant la reconstruction 3D, provient de la taille réelle de la caméra. Cette dernière, comparée à la projection observée sur les angiogrammes permet de restituer l'orientation 3D de la caméra.

Organisation de la thèse

Voici en ordre séquentiel, les diverses sections qui composent le présent document.

Le chapitre 2 introduit les modalités d'imagerie vasculaire abordées dans ce document, à savoir l'angiographie et l'imagerie ultrasonore endovasculaire. Une description des appareillages, de leur fonctionnement, ainsi qu'une modélisation mathématique sont présentés.

Le chapitre 3 introduit le premier contexte de reconstruction 3D abordé dans cette thèse, la reconstruction 3D vasculaire à l'aide de l'angiographie, en faisant une revue de littérature du sujet.

Le chapitre 4 présente l'article *3D Heart Motion from Single-Plane Angiography of the Coronary Vasculature : a Model-Based Approach* soumis à la revue *IEEE Transactions on Medical Imaging*, où l'on présente notre méthode de reconstruction spatio-temporelle de l'arbre coronarien à l'aide d'une seule vue.

Le chapitre 5 introduit le second aspect de reconstruction 3D développé dans cette thèse, on parle ici de reconstruction 3D servant à l'orientation absolue d'image IVUS dans un contexte de fusion des modalités ultrasonore et angiographique d'imagerie vasculaire.

Le chapitre 6 présente l'article *Trajectory Assessment of an IVUS Transducer from Single-Plane Cineangiograms : a Phantom Study* soumis à la revue *IEEE Transactions on Bio-Medical Engineering.*

Finalement, le chapitre 7 discute des contributions apportées par cette thèse dans le domaine de la reconstruction 3D vasculaire en imagerie médicale.

Chapitre 2

IMAGERIE VASCULAIRE

Il existe deux grandes modalités d'imagerie vasculaire : l'imagerie angiographique et l'imagerie ultrasonore endovasculaire (IVUS). Une brève description de ces modalités ainsi qu'une modélisation mathématique de caméra, nécessaire pour leur étude dans le cadre du présent travail de recherche, seront ici présentées.

2.1 L'imagerie angiographique

Bien que de caractère invasif, l'angiographie demeure le standard de référence (“*golden standard*”) pour l'imagerie vasculaire [26]. L'angiographie est une technique d'imagerie médicale qui utilise les rayons X pour projeter une représentation des vaisseaux sanguins. Même si les rayons X sont découverts par le physicien allemand Wilhelm Conrad Röntgen en 1895, l'invention de l'angiographie date du milieu des années 1920, où le neurologue portugais Antonio Egas Moniz propose d'injecter un produit de contraste dans les artères en complément d'une radiographie pour visualiser les vaisseaux. Lorsque l'examen angiographique se compose d'une séquence de plusieurs images par seconde, l'on parle de cinéangiographie. Une angiographie appliquée aux artères coronaires se nomme une coronarographie.

Le coefficient d'absorption des rayons X entre les artères et les tissus environnants est trop similaire et est trop faible pour permettre une visualisation de la vascularisation. Pour ce faire, on injecte dans les vaisseaux un agent contrastant radio-opaque, à l'aide d'un cathéter. Dans le cas de coronarographie, l'injection se fait habituellement à partir de l'artère fémorale, Fig. 2.1.

L'angiographie permet, entre autres, d'étudier la morphologie du réseau vasculaire

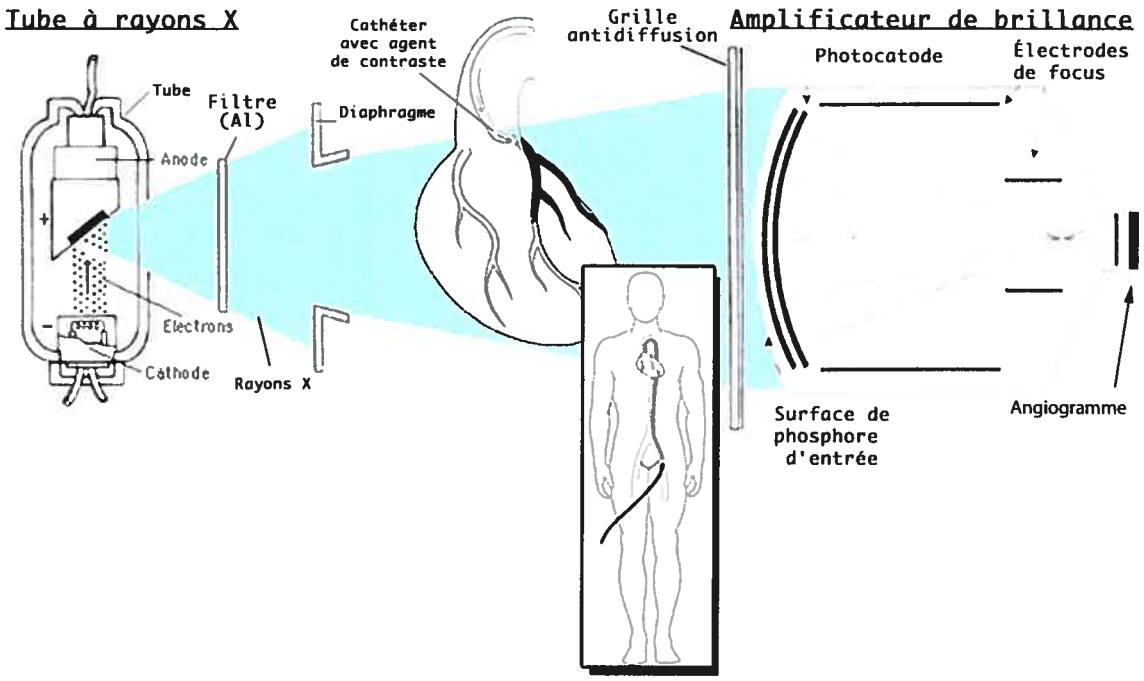

FIG. 2.1. **Système angiographique. Schématisation d'une coronarographie où les artères coronaires sont rendues opaques aux rayons X grâce à l'injection de l'agent de contraste.**

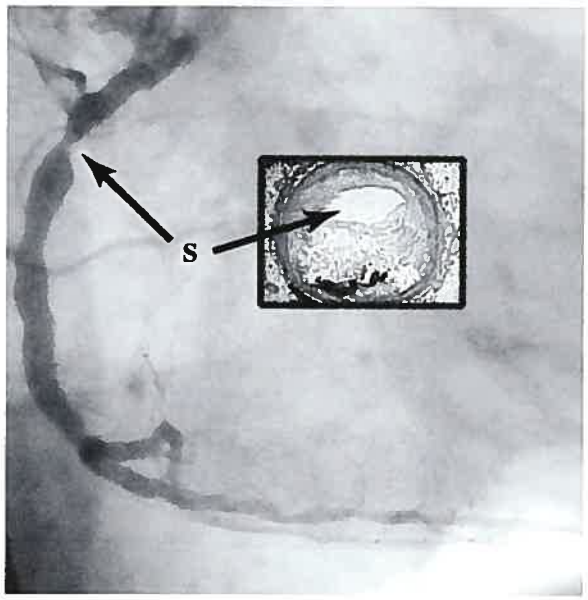

FIG. 2.2. **Exemple de sténose. S : Sténose, vue angiographique et en coupe. D'après Tafforeau [77].**

ainsi que la détection de sténoses [10], Fig. 2.2. La cinéangiographie quant à elle permet de réaliser un examen fonctionnel du réseau vasculaire. Par exemple, en faisant un suivi de l'écoulement du bolus composé de l'agent de contraste radio-opaque, on peut établir le débit sanguin [63].

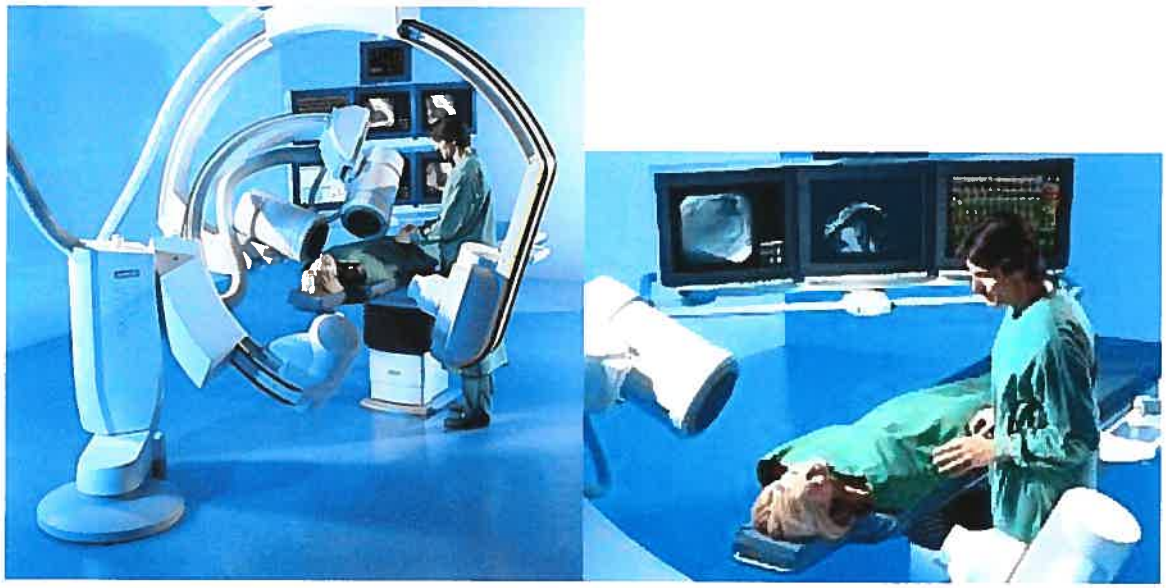

(a) *Système biplan* (b) *Système monoplan*

FIG. **2.3. Systèmes angiographiques. D'après Siemens Axiom Artis [73].**

L'appareil d'imagerie angiographique est composé d'une source de rayons X et d'un amplificateur de brillance entre lesquels le patient est placé. L'amplificateur de brillance convertit les rayons X en longueurs d'onde visibles qui permettent l'exposition des capteurs CCD (charge-coupled device), Fig. 2.1. L'angle relatif entre le patient et le système peut être modifié afin d'obtenir des images où la projection des vaisseaux est optimale. Lorsque le système angiographique est composé de 2 sources de rayons X et de 2 amplificateurs de brillance, on dit que le système est biplan ; en présence d'une seule source et amplificateur, le système est monoplan, Fig. 2.3.

Le principal mode d'acquisition d'image de ce travail de recherche est la ciné-

angiographie. En effet, les méthodes de reconstruction 3D présentées reposent sur l'information spatiale que procurent les images, c'est-à-dire la localisation d'éléments anatomiques dans un espace euclidien, mais aussi sur l'information temporelle obtenue par l'acquisition séquentielle des images.

L'autre mode d'imagerie utilisée dans le présent travail de recherche, l'imagerie échographique endovasculaire a un intérêt, non pas pour ses images comme telles, mais pour la fusion de ces deux modes d'imageries lors de reconstruction 3D, c'est-à-dire l'imagerie échographique et l'imagerie à rayon X. Un bref survol des particularités de l'imagerie IVUS est présenté à la section suivante, tandis que la fusion utilisée pour la reconstruction 3D sera abordée dans le chapitre 5.

2.2 L'imagerie échographique endovasculaire

L'utilisation de l'imagerie par ultrason remonte à la fin des années 1950. Son principe repose sur le fait que les ultrasons émis sont réfléchis de façon différente lors du passage de tissus à un autre ayant des propriétés échogènes (densités, compressibilités) différentes. En mesurant les variations des quantités d'énergie réfléchie, il est donc possible de détecter une discontinuité dans un milieu.

L'imagerie échographique endovasculaire est rendue possible par la miniaturisation de la caméra (le transducteur) qui est fixée à l'extrémité d'un cathéter, Fig. 2.4. Ce dernier est inséré dans une artère et c'est durant le retrait de la caméra, le long d'un fil guide, que les images des parois vasculaires sont captées. La vitesse du retrait varie typiquement de 0.5 à 1 mm/sec.

L'échographie endovasculaire génère des images en coupe des vaisseaux par rotation d'un traducteur à ultrasons. Les images présenteront des variations d'intensité en fonction de la composition du tissu des vaisseaux, Fig. 2.5. L'avantage qu'a l'échographie endovasculaire par rapport à l'angiographie est au niveau de la précision de la localisation des plaques artérielles [48]. Certains inconvénients de cette méthode

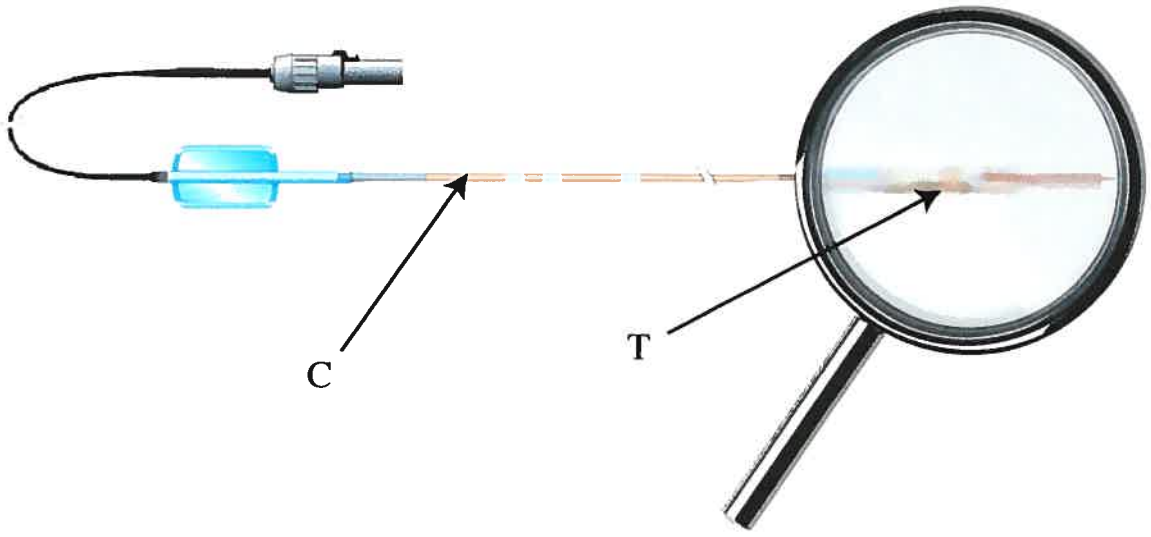

FIG. **2.4. Cathéter IVUS. À l'extrémité du cathéter se trouve le transducteur. C : Cathéter, 150** cm **x 1** mm **(longueur x épaisseur) ; T : transducteur. D'après JOMED [33].**

consistent en l'absence de repères globaux de positionnement, ainsi que les effets de torsion subis par le transducteur lors du retrait.

2.3 Modélisation mathématique de caméra

Afin de permettre une manipulation informatique des images produites par le système d'imagerie angiographique une modélisation mathématique de caméra est requise. Deux modèles sont utilisés dans cette thèse et seront décrits dans la section suivante : le modèle de caméra à sténopé qui est un modèle de projection perspective et sa simplification par le modèle projectif à perspective faible.

La formulation employée pour différencier les deux modèles de projection est la suivante : le *modèle de projection à perspective entière, pleine ou forte* fait référence

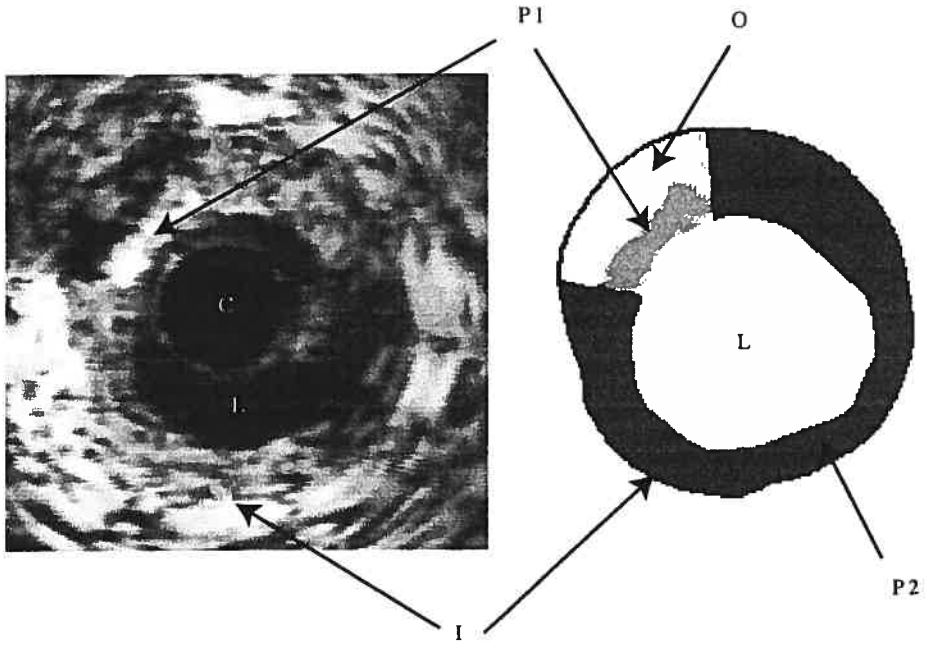

FIG. **2.5. Exemples d'image IVUS. Image IVUS présentant une plaque d'athérosclérose. C : cathéter ; L : lumière ; P 1 : Plaque calcifiée ; P 2 : Plaque cellulaire, fibreuse ; O : Zone d'ombre ; I : Interface média - adventice. D'après Wahle, 2001 [88].**

à la nomenclature anglophone *full perpective projection model*, tandis que le *modèle de projection à perspective faible* est l'équivalent au *weak perpective projection model.*

2.3.1 Modèle de projection à perspective entière

Le modèle de caméra à sténopé dans un système projectif à perspective entière est représenté à la Figure 2.6. On peut y voir que le plan de projection est centré et perpendiculaire à l'axe Z et que le centre de projection est situé à l'origine.

En définissant $\mathbf{P}_i = [X_i, Y_i, Z_i]$ en tant que point 3D et $\mathbf{p}_i = [x_i, y_i]$ comme point 2D, la relation entre $\mathbf{P}_i$ et sa projection $\mathbf{p}_i$, pour une caméra à sténopé est définie par

$$x_i = f\frac{X_i}{Z_i} \tag{2.1}$$

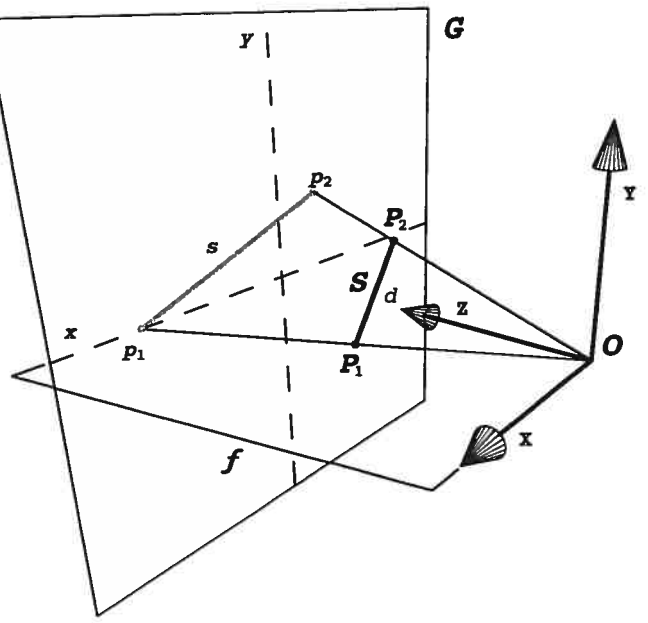

FIG. **2.6. Modèle de projection à perspective entière. Le segment $\mathbf{S} = [\mathbf{P}_1, \mathbf{P}_2]$ dans l'espace 3D est projeté sur le plan de projection G en tant que segment $\mathbf{s} = [\mathbf{p}_1, \mathbf{p}_2]$. G : plan de projection ; O : centre de projection ; S : segment 3D ; s : segment 2D.**

et

$$y_i = f\frac{Y_i}{Z_i}, \tag{2.2}$$

où f est la distance focale, la distance entre le centre de projection et le plan de projection.

Le système d'angiographie monoplan peut donc être modélisé mathématiquement suivant le modèle de projection à perspective entière en adaptant ce dernier aux caractéristiques de l'appareillage angiographique 2.7. Par exemple,

- la source des rayons X est coïncidente au centre de projection ;
- l'angiogramme correspond au plan de projection ;
- le système d'axe est orienté de telle sorte que l'axe Z est placé dans la prolongation entre la source des rayons X et le centre de l'angiogramme. Les axes X et Y correspondent aux axes X et Y de l'angiogramme ;

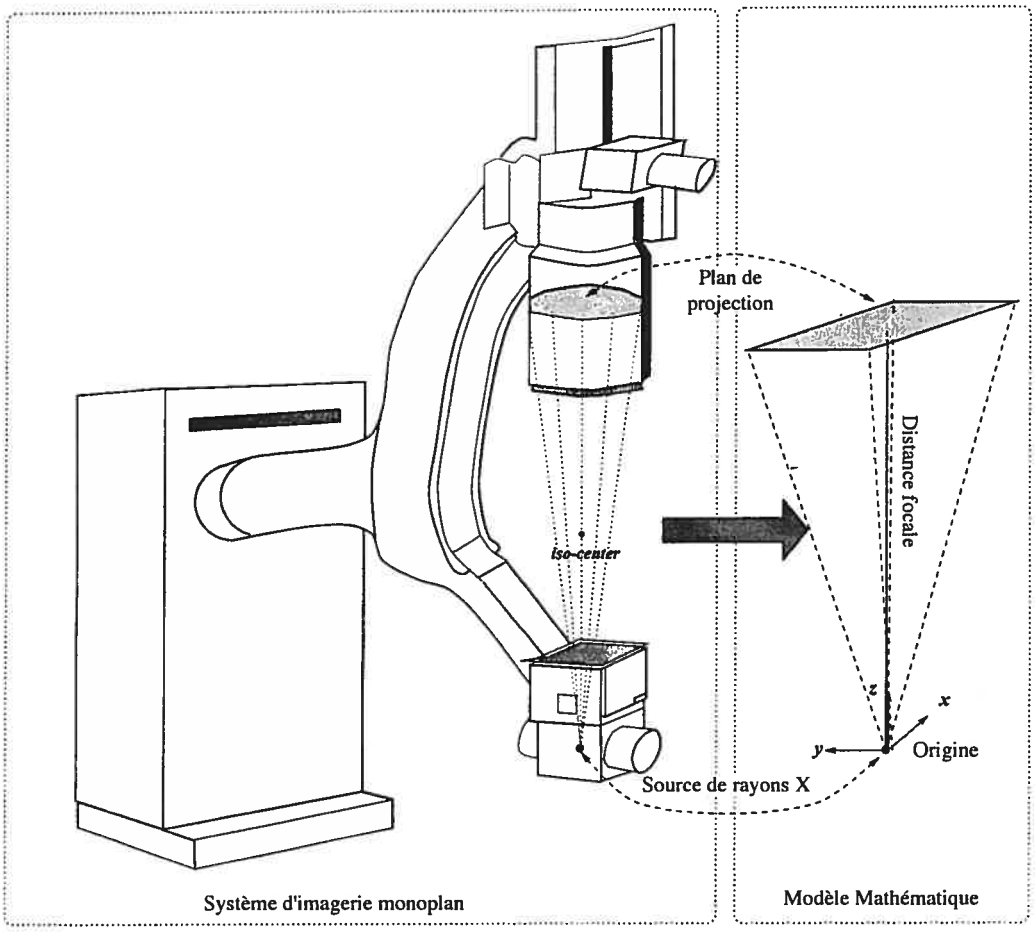

FIG. **2.7. Modèle mathématique d'un système angiographique. Dans la présente figure, un parallèle est présenté entre un système angiographique et une modélisation mathématique. Les divers éléments tels que l'origine de projection, le plan de projection, l'orientation des axes et la distance focale de la caméra sont ici représentés. D'après Chen, 2000 [10].**

– l'objet projeté est toujours placé entre le centre de projection et le plan de projection.

2.3.2 Modèle de projection à perspective faible

Le modèle de projection à perspective faible est une simplification du modèle de projection à perspective entière, Fig. 2.8. Son avantage réside dans le fait que les

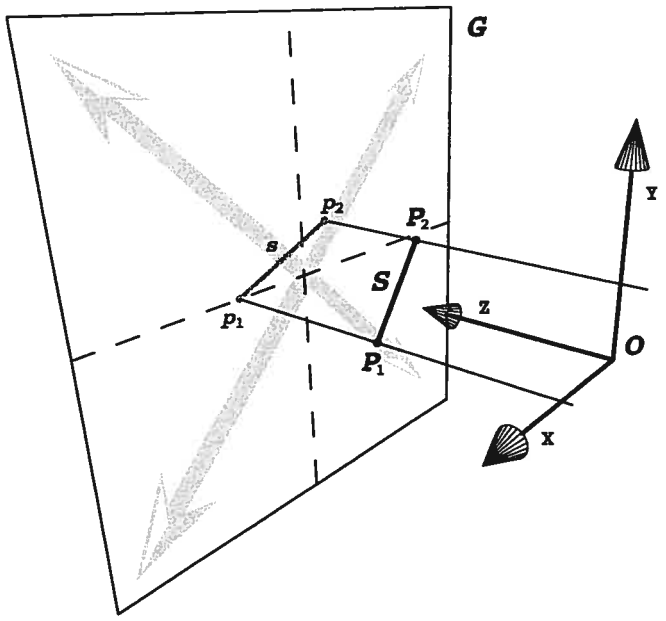

FIG. **2.8. Modèle de projection à perspective faible. La projection à perspective faible est définie comme étant une projection orthogonale suivie d'une mise à l'échelle. La mise à l'échelle est représentée par les flèches diagonales grises. En perspective faible, les projecteurs sont parallèles entre eux.**

équations de projection (2.1) et (2.2) sont linéarisées, ce qui permet à des calculs de minimisation de converger dans certaines circonstances.

En projection à perspective faible la projection des points 3D ne dépend pas de la profondeur de chacun des points, mais plutôt de la moyenne des profondeurs de l'objet. Les équations (2.1) et (2.2) deviennent alors

$$x_i = f' X_i \tag{2.3}$$

et

$$y_i = f' Y_i, \tag{2.4}$$

où $f' = \frac{f}{\overline{Z}}$, $\overline{Z} = \frac{1}{n} \sum_{i=1}^{n} Z_i$ et n est le nombre de points.

Le facteur d'erreur dû à la simplification de la perspective faible devient négligeable

lorsque la profondeur de la scène $\overline{Z}$ est environ 20 fois plus grande que la profondeur de l'objet [79].

En utilisant des valeurs réalistes, avec une profondeur de la scène moyenne de 80 *cm*, un retrait de caméra IVUS réalisé sur un segment de coronaires ayant une profondeur de 4 *cm* est tout à fait possible. Par contre, si l'on considère l'arbre coronarien en entier, sa profondeur peut atteindre 10 *cm* selon certaines angulations, ce qui implique la présence de distorsions dues au modèle de caméra à perspective faible.

Lorsqu'une modélisation de projection à perspective faible est utilisé pour représenter un système angiographique, la correspondance et l'orientation des paramètres reste les mêmes que pour une modélisation à perspective entière, c'est seulement la méthode de projection qui change.

Chapitre 3

RECONSTRUCTION 3D ET SUIVI DE L'ARBRE CORONARIEN

L'étude de la reconstruction 3D et du suivi des mouvements cardiaques peut être réalisée par l'entremise de divers modes d'acquisition d'images, chacun ayant ses avantages et inconvénients.

3.1 Modes d'acquisition

La plus ancienne des techniques, qui est sans contredit l'angiocardiographie[1], utilise le rayon X pour photographier le coeur. Mais comme le coefficient d'absorption des tissus cardiaques et du sang sont très faibles, on utilise un agent de contraste que l'on injecte dans les ventricules ou les artères coronaires à l'aide d'un cathéter. Le cathéter est en général introduit par l'artère fémorale. L'agent opacifiant quant à lui, est à base d'iode.

L'échocardiographie utilise les ultrasons et grâce à l'effet Doppler, permet de représenter l'anatomie et les mouvements cardiaques de façon non invasive [65]. Récemment deux nouvelles techniques à base d'ultrasons ont fait leur apparition : la coloration cinétique (*color kinesis*) et l'échocardiographie 3D. La coloration cinétique, basée sur la quantification acoustique, permet une segmentation et le suivi automatique de l'endocarde [50] tandis que l'échocardiographie 3D permet une représentation 3D de la géométrie cardiaque [43].

La tomographie spiralée assistée par ordinateur (*spiral computed tomography*) permet une reconstruction 3D à partir d'images multiples obtenues grâce au rayon X [8].

[1] Technique utilisé par Forsmann sur lui-même en 1928 ([51] pp. 43).

La qualité des images est un compromis entre la résolution spatiale, temporelle et les niveaux de contraste de l'image [60].

L'imagerie à résonance magnétique (*MRI, magnetic resonance imaging*) mesure, entre autres, la densité spatiale des protons des tissus et permet de forts contrastes entre les tissus mous. L'appareil mesure la variation de la résonance magnétique des protons entre le moment où l'on aligne leur spin par un champ magnétique et leur retour à l'équilibre. Une technique introduite par Zerhouni, l'imagerie à résonance magnétique à repères (*tagged MRI*) [92], crée des zones de saturation magnétique ce qui produit des plans foncés disposés de façon orthogonale au plan de projection. Ces zones d'ombre suivent la déformation des tissus dans le temps et dans l'espace.

Un autre type d'imagerie, l'imagerie par isotope, consiste à injecter un agent radioactif et à cartographier le bolus dans le corps du sujet. On reconstitue le volume par la saisie de plusieurs coupes. Les techniques employées sont la tomographie par émission de positons (*PET, positron emission tomography*) et la tomographie monophotonique (*SPECT, single photon emission tomographie*) [25].

3.2 Quantification du mouvement cardiaque

Indépendamment du mode d'acquisition, la quantification du mouvement cardiaque peut être réalisée à partir de la segmentation de l'endocarde, ce qui permet de suivre la déformation du ventricule, ou à partir du suivi de repères. Ces derniers peuvent être, soit des repères implantés chirurgicalement comme des repères métalliques [40], soit des repères anatomiques [35, 56, 42] comme les points de bifurcation des artères coronaires, ou soit des repères induits à l'aide de l'imagerie à résonance magnétique à repères [49].

Lorsque l'on fait le suivi de repères disposés sur l'épicarde, on peut se demander si ces derniers reproduisent correctement les mouvements de l'endocarde. Liu *et al.* y répondent par l'affirmative, en constatant des coefficients de corrélation des moyennes

de direction, vitesse et déplacement entre l'épicarde et l'endocarde de 0.86, 0.79 et 0.78 respectivement.

Dans le cas du suivi des points de bifurcation des artères coronaires comme repères anatomiques, Kong *et al.* ont vérifié si les déplacements de repères anatomiques correspondaient aux déplacements de repères métalliques suturés sur l'épicarde près des bifurcations des coronaires. Ils ont obtenu un coefficient de corrélation de 0.89 [35].

Frangi *et al.* rapportent les préoccupations rencontrées dans la littérature concernant les influences qu'ont les repères métalliques sur la qualité des images et la modification des mouvements [23].

L'étude du mouvement cardiaque peut se faire dans un espace 2D ou 3D. Lorsque l'étude du mouvement cardiaque se fait à partir d'imagerie à résonance magnétique ou à partir d'une reconstruction angiographique biplan, on est en présence d'un référentiel 3D. On est en présence d'un référentiel 2D lorsque le mouvement cardiaque est représenté par des mesures de déplacements prises directement à partir d'images angiographiques monoplan. L'analyse du mouvement cardiaque dans un espace 2D peut apporter une certaine information quantitative, par contre la composante de profondeur se trouve fusionnée avec les déplacements horizontaux et verticaux [32].

Kong *et al.* furent dans les premiers à analyser les déformations du myocarde [35]. Entre 10 à 20 points de bifurcations coronariennes sur 11 sujets, normaux et anormaux, furent localisés à partir d'images cinéangiographiques biplans durant plusieurs cycles cardiaques (figure 3.1 et 3.2). Ils utilisaient les coordonnées u, v de l'image antéropostérieure comme coordonnées X, Y 3D et les coordonnées u, v de l'image latérale comme coordonnées Y, Z 3D. Ce qui équivaut en fait à une projection orthographique. Les variations de la distance euclidienne 3D entre les points de référence furent représentées graphiquement (figure 3.3). On peut constater une similitude dans les variations des longueurs de segments dans le cas de sujets normaux (figure 3.3, graphique de gauche). Et au contraire, les sujets anormaux, souffrant d'occlusions plus ou moins sévères des coronaires, présentent des courbes de variations qui sont

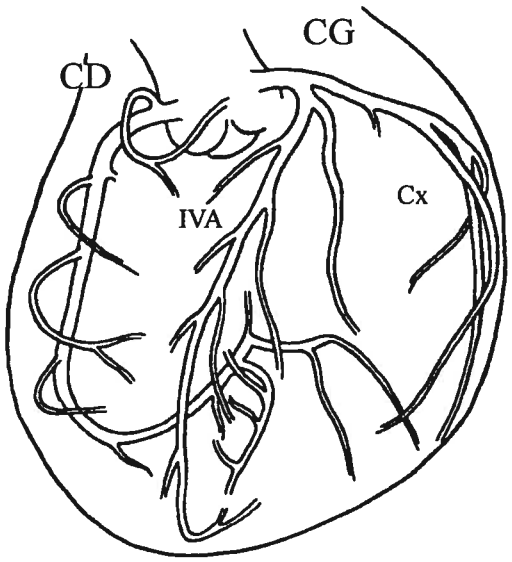

FIG. **3.1. Schématisation des artères coronaires principales et secondaires. CD : Coronaire droite ; CG : Coronaire gauche ; IVA : Interventriculaire antérieure ; Cx : Circonflexe. D'après Dodge *et al.* [17].**

très différentes des sujets normaux (figure 3.3, graphique de droite). Donc, l'étude des variations des segments coronariens est un indicateur du bon fonctionnement cardiaque.

Potel *et al.* [56, 55] étudièrent par la suite les mouvements du ventricule gauche par l'entremise du suivi des coronaires. Ils utilisèrent une technique [42] qui reconstruit les points de bifurcation des artères coronaires à partir de cinéangiographies biplan et à l'aide d'un modèle de projection à perspective complète. Leur attention fut portée vers la caractérisation des mouvements locaux : tels le déplacement maximum des points de références, le déplacement moyen, les vecteurs de déplacements ainsi que la localisation du centre de contraction. À la figure 3.4, on peut voir le déplacement 3D maximum en *cm* de 28 points de bifurcations. Le déplacement de la paroi postérieure (partie de droite, figure 3.4) est de 1.5 à 2 fois supérieur au déplacement de la paroi antérieure. De plus, les déplacements maximums décroissent le long de l'IVA (artère InterVentriculaire Antérieure) et des branches diagonales lorsque l'on se déplace de

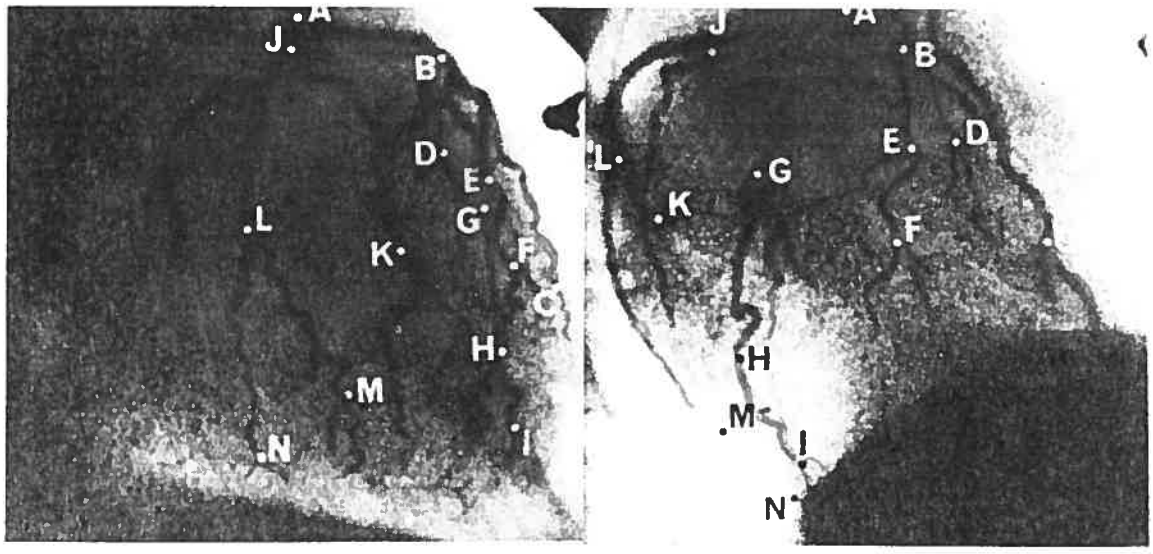

(a) *Incidence oblique antérieure droite* (b) *Incidence oblique postérieure droite*

FIG. **3.2. Exemple de coronarographie biplan avec identification des points de bifurcations vasculaires.** $A - N$ **: Points de bifurcations. D'après Kong** *et al.* **[35].**

la base vers l'apex (de haut en bas, figure 3.4).

Concernant le centre de contraction, Potel *et al.* constatent qu'il se déplace le long du grand axe reliant la base à l'apex. À la télédiastole (dilatation maximale) la position du centre de contraction est à 49 % du grand axe (C_2, figure 3.4). À la mi-systole, le centre de contraction se déplace vers l'apex pour être à 78 % du grand axe (C_1). À la télésystole (contraction maximale), le centre de contraction se situe de nouveau au centre du ventricule (C_2) et à la mi-diastole, il retourne vers la position C_1.

Plus récemment Puentes *et al.* ont cherché des paramètres qui pouvaient décrire le mouvement global et local des artères coronaires [59]. Ils se basent sur la ligne centrale des coronaires et indiquent, un peu comme Potel *et al.*, la longueur des déplacements, l'amplitude, les composantes radiale/perpendiculaire, la composante de rotation, de

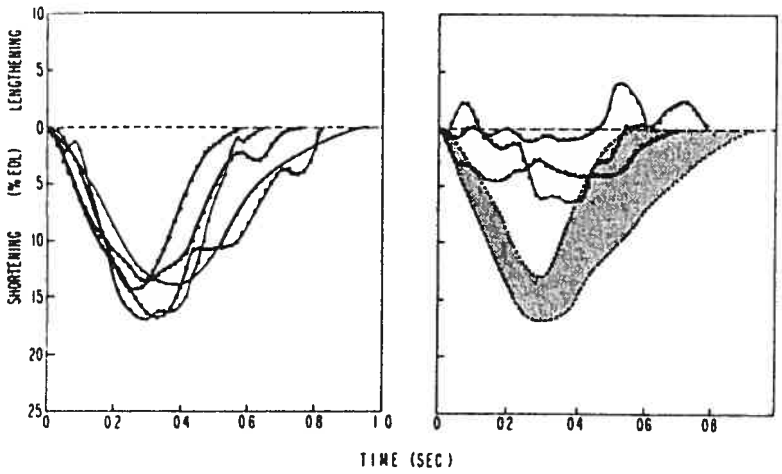

FIG. **3.3. Comparaisons des variations de longueur de segments le long de l'artère Interventriculaire antérieure. À gauche, sujets normaux. À droite, sujets anormaux. D'après Kong** *et al.* **[35].**

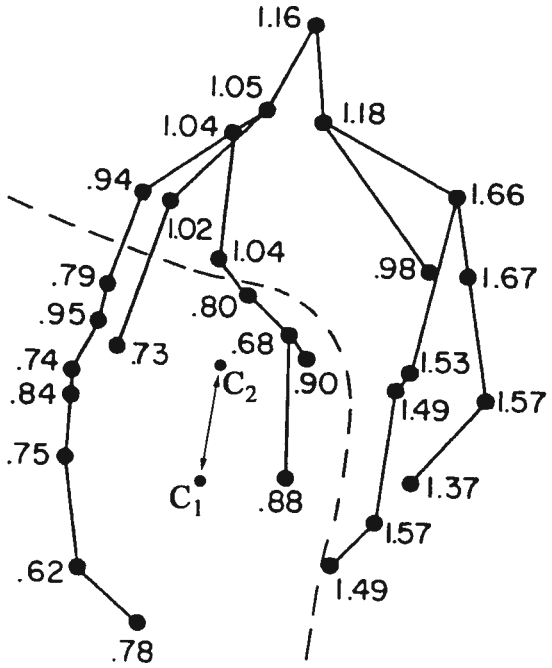

FIG. **3.4. Déplacements maximums en cm de 28 points de bifurcations.** C_1 **: centre de contraction à la mi-systole et à la mi-diastole ;** C_2 **: centre de contraction à la télédiastole et à la télésystole. D'après Potel** *et al.* **[56].**

torsion, etc.

Cette recherche des caractéristiques de déformation de la paroi cardiaque, a poussé Meier *et al.* à emprunter au cadre théorique de la cinématique [46]. Bien que la surface complète du coeur se déforme de façon non linéaire, la déformation de surfaces infinitésimales peut toujours être décrite par une expression linéaire. Meier *et al.* décrivent les déformations par des vecteurs de rotation et d'étirement.

La modélisation et l'analyse fonctionnelle tridimensionnelle en l'imagerie cardiaque est un champ d'intérêt croissant. Frangi *et al.* passent en revue plus de 200 articles parus depuis les deux dernières décennies portant sur le sujet. Ils catégorisent, indépendamment du mode d'acquisition, les modèles en tant que modèles de surfaces, modèles volumétriques et modèles de déformations [23].

D'ailleurs, Aggarwal *et al.*, dans un cadre encore plus englobant, subdivise l'analyse du mouvement en tant que mouvement rigide et non rigide. Ce dernier pouvant être qualifié selon le degré de déformation de l'objet à l'étude soit par mouvement articulé, mouvement élastique ou mouvement fluide. Le mouvement cardiaque est bien entendu classé comme mouvement élastique [1].

Avant de pouvoir modéliser les déformations des parois cardiaques, on doit en saisir l'information. Dans le cas des techniques d'imagerie 3D, comme la tomographie SPECT ou la résonance magnétique (IRM), la reconstruction est obtenue directement et on peut synchroniser leurs intrants avec l'électrocardiogramme afin d'obtenir une séquence temporelle d'images 3D, i.e. 4D [20]. Par contre, dans le cas des images angiographiques par rayons X que nous utilisons, l'information est bidimensionnelle, on doit donc la traiter afin d'en extraire une information 3D.

3.3 Reconstruction 3D en angiographie

La récupération de l'information 3D peut-être réalisée à partir d'une, deux ou plusieurs images.

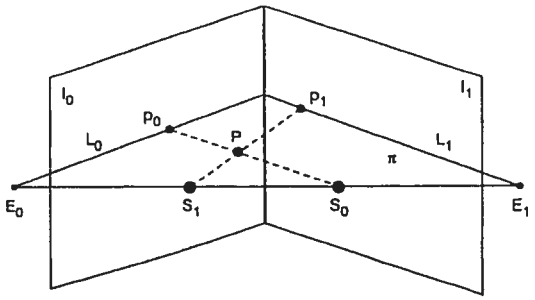

FIG. **3.5. Géométrie épipolaire. D'après Windyga *et al.* [90].**

3.3.1 Images stéréoscopiques

La reconstruction de l'arbre coronarien à partir de deux images est sans contredit la méthode la plus étudiée [35, 55, 63, 13, 90, 64, 11, 91, 37]. La technique classique de reconstruction 3D à partir de deux vues consiste à calibrer les caméras par l'utilisation d'un cube de calibrage dont la position relative des points est connue. En connaissant la position 3D des points et en comparant cette position aux coordonnées correspondantes sur les deux images, il est possible d'obtenir les paramètres internes (distance focale, facteur de mise à l'échelle) et les paramètres externes de rotation et de translation.

Cheriet [14] décrit une méthode d'autocalibrage de système cinéangiographique biplan. Sa méthode trouve les paramètres internes et externes à partir d'une estimation initiale qui est par la suite raffinée à l'aide de l'algorithme itératif de Levenberg-Marquardt. La fonction objective cherche à minimiser la distance quadratique entre les projections analytiques et les projections observées.

Une fois le calibrage obtenu, l'exploitation de la géométrie épipolaire permet de réduire l'espace de recherche pour réaliser l'appariement des points provenant des deux images. Selon la géométrie épipolaire (figure 3.5) les sources de projection S_0 et S_1 avec un autre point P, définissent le plan épipolaire π. Les intersections entre chacun des plans de projection (I_0, I_1) et le plan épipolaire définissent les droites

épipolaires (L_0, L_1). Les points E_0 et E_1 sont connus comme étant les épipoles. Connaissant la position des sources et la projection d'un point sur un des plans de projection, la zone de recherche du point correspondant sur l'autre plan de projection se limite à une droite. Chen *et al.* [12], utilisent cette méthode pour faire la reconstruction 3D des artères coronaires.

Blondel *et al.* [6] vont plus loin en réalisant en quelque sorte, une double recherche épipolaire. En effet, ils utilisent une troisième image afin de valider les ambiguïtés qui pourraient rester en n'utilisant la correspondance qu'entre seulement deux images.

Il est aussi possible d'obtenir une information relative, i.e. une reconstruction à un facteur d'échelle prêt, en n'utilisant que la géométrie épipolaire sans calibrage de caméra [21].

3.3.2 Images monoculaires

La reconstruction de l'information 3D à partir d'une seule vue nécessite l'utilisation d'un modèle qui décrit la position relative dans un espace 3D des points rencontrés sur le plan de projection. De plus, l'on doit connaître l'appariement entre les points 3D et leur projection.

Il existe une multitude de techniques permettant de retrouver les transformations rigides (rotation et translation) nécessaires afin de faire correspondre un ensemble de points 3D d'un référentiel à un autre. Certaines méthodes utilisent une solution itérative qui minimise une fonction de coût ou une méthode analytique. Arun *et al.* [2] utilisent une méthode itérative de minimisation de distance quadratique basée sur la décomposition en valeurs singulières. Horn quant à lui trouve une solution analytique en représentant les rotations par des quaternions [30] ou en utilisant des matrices orthonormales [31].

Lorsque l'on recherche l'orientation d'un ensemble de points 3D à partir d'une projection 2D, la métrique de similarité peut se faire à partir d'un référentiel 2D ou 3D. Basri [3] définit la métrique de similarité dans l'espace 2D comme étant la *métrique*

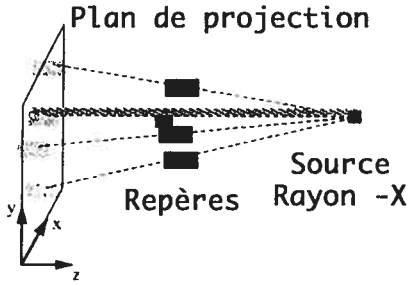

FIG. **3.6. Géométrie de l'image. D'après Tang *et al.* [78].**

image et par *métrique de transformation* la mesure de similarité dans l'espace 3D. Dans le cas d'un référentiel 2D, on projette les points 3D d'un modèle dans l'espace 2D et on réalise par la suite un calcul de distance, comme par exemple la distance euclidienne moyenne [41].

Pour obtenir une métrique de similarité dans l'espace 3D, on fait une projection inverse (*back-projection*) des points 2D pour obtenir un ensemble de *droites* 3D (figure 3.6). Par la suite, on cherche à minimiser les distances entre les points 3D du modèle et les droites [78, 28]. Tang *et al.* [78] adaptent l'algorithme itératif du point le plus prêt (*ICP, iterative closest point algorithm*) de Besl et McKay [4] en modifiant l'algorithme original qui est très général, au cas particulier de la recherche de l'orientation à partir d'une seule image angiographique. La recherche de l'orientation peut être décrite comme un problème de minimisation des moindres-carrés où la fonction objective est basée sur une métrique de distance euclidienne entre une série de points 3D et un ensemble de droites. Les modifications apportées par Tang *et al.*, sont de deux ordres. Premièrement, ces derniers constatent qu'il existe des relations entre les points et les droites qui permettent d'obtenir des valeurs initiales pour la translation et la rotation. Deuxièmement, la mise en correspondance réalisée entre les points et les droites est conservée pour la suite des itérations, ce que n'effectue pas l'algorithme original de Besl et McKay.

Esthappan *et al.*, quant à eux, utilisent une méthode intitulée *technique de pro-*

jection simple (SPT, single projection technique) afin de retrouver l'orientation d'un cathéter, décrit par une série de points 3D, à partir d'une projection de ces points. Leur métrique de similarité, la distance quadratique moyenne, se réalise dans l'espace image 2D. À partir de valeurs initiales de transformations rigides, 3 paramètres de rotation $(\theta_{xy}, \theta_{xz}, \theta_{yz})$ et 3 paramètres de translation $(t_x, t_y, t_z,)$, ils cherchent, de façon itérative, à minimiser la distance quadratique moyenne. C'est en fait, la méthode de Lowe [41] appliquée au problème de l'orientation de cathéters. Esthappan *et al.* [18] rapportent que l'orientation et la position d'un cathéter de 0.18 *cm* de diamètre peuvent être établies avec une erreur de 1.6 ° et de 0.8 *cm* respectivement. Aucun mouvement n'est impliqué dans cette méthode de reconstruction 3D.

Nguyen et Sklansky [52] décrivent un système qui permet de réaliser une reconstruction 3D et de faire le suivi de l'arbre coronarien à partir uniquement d'une séquence angiographique monoplan. Étant les premiers à proposer une méthode complète de reconstruction 3D et ayant été une source d'inspiration pour la présente thèse, une description détaillée est présentée à la section suivante.

Description de l'algorithme de Nguyen et Sklansky

La méthode de reconstruction 3D et le suivi de l'arbre coronarien de Nguyen et Sklansky se fait dans un premier temps par l'appariement de points le long de l'arbre coronarien d'une image à l'autre, et dans un deuxième temps par un suivi 3D.

L'appariement est réalisé en 4 étapes. Premièrement, on simplifie les branches du squelette de l'arbre coronarien en y ajustant des courbes polynomiales du 4e ou 5e degré. Deuxièmement, on calcule la tangente aux différents points le long de la courbe polynomiale. Par la suite, on réalise la différence absolue des tangentes successives pour obtenir une liste des *changements angulaires* : $\triangle\theta_i = |\theta_{i+1} - \theta_i|$. Finalement, en utilisant la méthode de programmation dynamique, on effectue l'appariement des points le long de l'arbre coronarien entre 2 images successives. Cet appariement est basé sur la minimisation de la somme des différences absolues entre les *changements*

angulaires de 2 images successives.

Une fois l'appariement réalisé, Nguyen et Sklansky passent à l'autre partie de leur méthode qui consiste à déformer un modèle 3D pour l'ajuster aux images successives d'une séquence cinéangiographique monoplan.

L'algorithme de Nguyen et Sklansky permet de faire une reconstruction 3D à partir d'une séquence d'images 2D représentant un objet en mouvement. Il repose sur quelques hypothèses simplificatrices, par exemple, le péricarde (surface externe du coeur) a une forme ellipsoïdale, les mouvements contractiles se font à partir d'un centre de contraction fixe qui correspond au centre de l'ellipsoïde.

Nguyen et Sklansky rapportent plusieurs auteurs corroborant la validité du modèle radial [34, 74] et Potel en fait de même [55]. Par contre, Potel fait remarquer, contrairement à l'hypothèse de Nguyen et Sklansky, que le centre de contraction se déplace au cours de la contraction le long du grand axe reliant la racine au sommet du coeur.

La résultante de ces hypothèses permet de tirer une hypothèse d'invariance qui dicte que l'angle formé par deux droites reliant deux points sur la surface de l'ellipsoïde avec le centre de contraction au temps t_i reste le même pour le temps t_{i+1}, voir figure 3.7. Donc, l'angle θ_{ij}, formé par la droite (P_i, O) et la droite (P_j, O), est égal à l'angle ϕ_{ij}, formé par les droites (Q_i, O) et (Q_j, O), voir figure 3.7. Le point O, correspondant au centre de contraction, est connu et est fixe tout au long de l'algorithme. L'objet V_m contient les point P dont les coordonnées u, v et incidemment la profondeur w, sont connues au temps m dans la séquence des contractions cardiaques. En ce qui nous concerne, en posant $m = 0$ alors l'objet V_0 correspondra au modèle de Dodge ajusté et déformé (voir le chapitre suivant). Quant à l'objet V_n, où $n = m + 1$, les coordonnées des points Q sont inconnues. Puisque Nguyen et Sklansky supposent une projection orthographique, les coordonnées x et y des points Q sont les coordonnées x et y mesurées sur l'image angiographique au temps n. À ce moment, les seules inconnues sont les coordonnées z des points Q, que l'on recherche tout en minimisant les variations entre les angles θ_{ij} et ϕ_{ij}. Une fois que l'on a obtenu

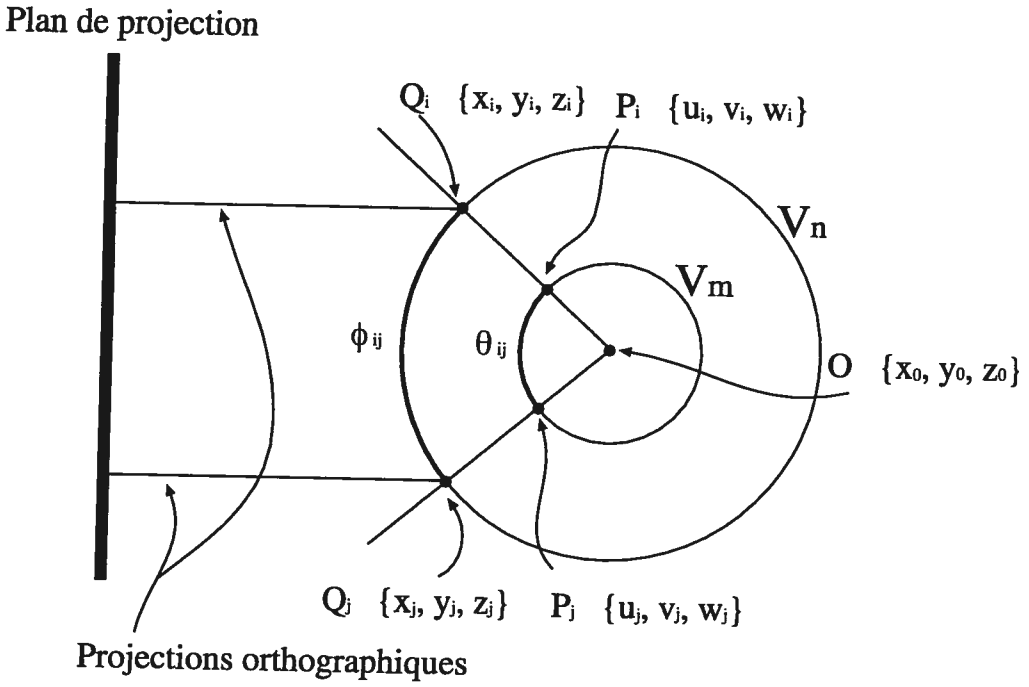

FIG. **3.7. Représentation des divers éléments impliqués dans le suivi du mouvement. Voir le texte pour la description des éléments. D'après Nguyen et Sklansky [52].**

la valeur des z, on réutilise cette information pour l'objet V_n afin de trouver l'état subséquent où, $m \leftarrow m + 1$.

La fonction objective est donc

$$f(z) = \sum_{i=0}^{N-2} \sum_{j=i+1}^{N-1} (\rho_{ij} - \lambda_{ij})^2 \tag{3.1}$$

où N est le nombre d'images dans la séquence angiographique d'une contraction cardiaque, $\lambda_{ij} = \cos\phi_{ij}$ et $\rho_{ij} = \cos\theta_{ij}$.

Le calcul des angles est réalisé à partir de deux droites définies par leurs cosinus directeurs. Puisque que les solutions à $\cos\phi_{ij}$ et à $\cos\theta_{ij}$ sont obtenues de façon similaire, nous n'élaborerons ici que la solution à $\cos\phi_{ij}$. Donc $\cos\phi_{ij}$ est défini par deux droites ayant respectivement comme cosinus directeur $\alpha_i, \beta_i, \gamma_i$ et $\alpha_j, \beta_j, \gamma_j$, soit

$$\cos\phi_{ij} = \cos\alpha_i \cos\alpha_j + \cos\beta_i \cos\beta_j + \cos\gamma_i \cos\gamma_j \tag{3.2}$$

où les cosinus directeurs sont obtenus pour le segment $P_i(x_i, y_i, z_i)$ à $O(x_0, y_0, z_0)$ par

$$\cos\alpha_i = \frac{x_i - x_0}{d_i}, \cos\beta_i = \frac{y_i - y_0}{d_i}, \cos\gamma_i = \frac{z_i - z_0}{d_i} \tag{3.3}$$

où d_i est la distance euclidienne entre les deux points, soit

$$d = \sqrt{(x_i - x_0)^2 + (y_i - y_0)^2 + (z_i - z_0)^2}. \tag{3.4}$$

Un processus similaire appliqué aux autres droites, $(P_j, O), (Q_i, O), (Q_j, O)$, suivi d'une recombinaison des équations (3.2, 3.3, 3.4), nous permet d'obtenir

$$\cos\phi_{ij} = \frac{(x_i - x_0)(x_j - x_0) + (y_i - y_0)(y_j - y_0) + (z_i - z_0)(z_j - z_0)}{\sqrt{[(x_i - x_0)^2 + (y_i - y_0)^2 + (z_i - z_0)^2][(x_j - x_0)^2 + (y_j - y_0)^2 + (z_j - z_0)^2]}}$$

$$\cos\theta_{ij} = \frac{(u_i - x_0)(u_j - x_0) + (v_i - y_0)(v_j - y_0) + (w_i - z_0)(w_j - z_0)}{\sqrt{[(u_i - x_0)^2 + (v_i - y_0)^2 + (w_i - z_0)^2][(u_j - x_0)^2 + (v_j - y_0)^2 + (w_j - z_0)^2]}}$$

Le problème de minimisation ayant comme fonction objective l'équation (3.1), peut être solutionné selon différentes méthodes comme Newton, Levenberg-Marquardt, recuit simulé, algorithmes génétiques, etc.

Selon la méthode de Nguyen et Sklansky, l'information de profondeur repose sur une modélisation radiale des contractions cardiaques, ce qui est sans contredit une sur-simplification. Prenant en considération ce fait, notre méthode de reconstruction 3D utilise un modèle de l'arbre coronarien afin d'apporter une information supplémentaire sur la profondeur.

Modèle des coronaires

Le présent travail de recherche repose sur un modèle tridimensionnel de points de référence disposés sur les artères coronaires. Ce modèle sert à la reconstruction 3D

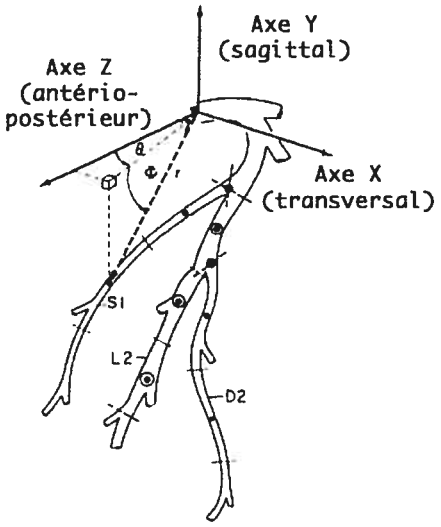

FIG. **3.8. Relation trigonométrique des angles et axes utilisés pour définir la positions des points de référence dans le modèle de Dodge (d'après [17]).**

de mouvements cardiaques à partir d'angiographies monoplans.

Le modèle est constitué de données provenant d'études réalisées par Dodge *et al.* [17, 16], qui consistait à mesurer la position 3D de 120 points de référence le long des artères coronaires provenant de 37 sujets normaux (31 hommes, 6 femmes). Les données furent mesurées en coordonnées polaires (ρ, θ, ϕ) (figure 3.8) à partir de la racine aortique. Les différents points de référence furent déterminés à partir de repères morphologiques comme les bifurcations des coronaires.

Les données colligées par Dodge *et al.* consistent en la moyenne et l'écart type des coordonnées de chaque point de référence. Pour compenser l'effet de distorsion des angiographies, les données furent normalisées, en appliquant le rapport entre le diamètre réel et le diamètre apparent du cathéter.

Dodge *et al.* ont constaté que la position des points de référence ne varie pas significativement selon le sexe, sauf que le nombre de sujets féminins dans cette étude est faible. Ceci est intéressant, puisque nous pouvons utiliser le même modèle autant pour les hommes que pour les femmes.

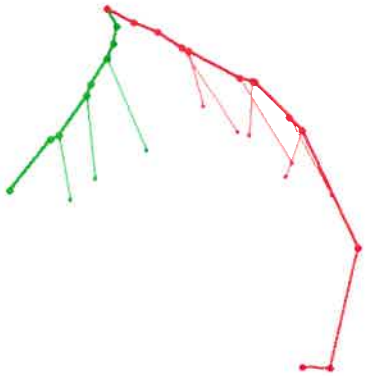

FIG. **3.9. Vue latérale de l'artère Cx (à gauche) et de l'IVA (à droite) provenant du modèle de Dodge.**

Il existe des méthodes de normalisation qui permettent de corriger les mesures de diamètre ou de longueur des coronaires, selon la taille du sujet (le BSA, *body surface area*) ou selon la fraction d'éjection [2] du ventricule gauche ($LVEDV^{0.33}$ *left ventricular end-diastolic volume*), mais Dodge *et al.* n'ont pas remarqué que leur utilisation apportait des corrections significatives.

Bien que Dodge ait mesuré la position de points de référence sur les trois artères principales, soit la coronaire droite (CD), l'artère interventriculaire antérieure (IVA) et l'artère circonflexe (Cx), nous n'avons conservé que l'IVA et la Cx (figure 3.9). Ceci est motivé par le fait que l'angiographie de la CD doit être faite séparément de l'angiographie de l'IVA et de l'artère Cx, ce qui nécessiterait une étape additionnelle de recalage des images. De plus, l'incidence donnant la meilleure vue est différente pour la CD et l'IVA. C'est donc ce modèle, qui sera maintenant ajusté aux points de repère sur l'angiogramme du sujet afin d'en trouver l'orientation.

En s'inspirant de la littérature en reconstruction 3D et du suivi du mouvement des artères coronaires le chapitre suivant décrit et valide une méthode qui utilise

[2] La fraction d'éjection est le pourcentage du volume sanguin éjecté lors de la systole par rapport au volume télédiastolique [80].

une information *a priori*, qu'est le modèle coronarien réduit de Dodge, pour faire la reconstruction 3D de l'arbre coronarien.

Chapitre 4

HEART CONTRACTION DETERMINATION USING 3D CORONARY RECONSTRUCTION FROM SINGLE-PLANE ANGIOGRAPHY

Cet article a été soumis le 2 mai 2004, aux fins de publication dans la revue IEEE Transactions on Medical Imaging.

Denis Sherknies, Jean Meunier et Jean-Claude Tardif

Soumis à : IEEE Transactions on Medical Imaging

Abstract

Two standard procedures to evaluate the heart contraction amplitude are echocardiography and ventriculography. In both cases, estimating the volume variation an ejection fraction coefficient can be established. We propose a method that computes a contraction index, similar to the ejection fraction, based only on the information obtained from single-plane coronarography. Our method first reconstructs in 3D, selected points on the angiogram, using a 3D model devised from data published by Dodge *et al.* [17, 16] We then follow the point displacements through a complete heart contraction cycle. The objective function, minimizing the RMS distances between the angiogram and the model, relies on affine transformations, i.e. translation, rotation and isotropic scaling. We validate our method on simulated projections using cases from Dodge *et al.* data. In order to avoid any bias, a leave-one-out strategy was used, which excludes the reference case when constructing the 3D coronary heart model. The simulated projections are created by transforming the reference case, with sca-

ling, translation and rotation transformations, and by adding random 3D noise for each frame in the contraction cycle. Comparing the true scaling parameters to the reconstructed sequence, our method is quite robust ($R^2 = 96\%, P < 1\%$), even when noise error level is as high as 1 *cm*. Using 10 clinical cases we then proceeded to reconstruct the contraction sequence for a complete cardiac cycle starting at end-diastole. A simple heart contraction mathematical model permitted us to link the measured ejection fraction of the different cases to the maximum heart contraction amplitude ($R^2 = 57\%$ with $P < 1\%$) determined by our method.

Keywords : 3D model, 3D reconstruction, coronarography, ejection fraction, single-plane angiography.

4.1 INTRODUCTION

The 3D representation of the coronary arteries is an effervescent research topic aiming at morphological and functional analysis. The 3D reconstruction usually involves two or more views. The views can be acquired simultaneously by biplane X-ray acquisition apparatus [55, 44, 66] or sequentially by rotating a single-plane acquisition device [47, 10, 6]. Some reconstructions have also been done by using only non-rotating single-plane angiograms [52].

Reconstructions made with multiple views are mainly realized by finding feature correspondences between images using the epipolar geometry constraint [63, 29].With non-rotating single-view reconstruction, since the depth information is lost, the process must rely on other means. In the work of Nguyen *et al.* the depth information was extrapolated by fitting together angular local features with a center of contraction constraint assuming a known initial 3D reconstruction. The method we propose, infers depth information by using a 3D coronary tree model. Even if variations exist in the tortuosity and localization of coronary arteries, certain structural characteristics exist, as illustrated by the existence of an anatomical heart atlas [51]. These structu-

ral characteristics can also be used in the 3D reconstruction process [24, 90, 9]. Our 3D reconstruction method relies on inter-patient similarities for fitting the projection of a coronary tree model to selected points along arteries.

Kong *et al.* [35] were the first to propose the use of variations in the coronary tree length, measured from 3D reconstruction, to quantify heart contractions. Potel *et al.* [56, 55], amongst others, studied the heart wall motion from coronarography. These methods all relied on biplane angiography. We realize the 3D reconstruction from single-plane cineangiography which enables us to extract a contraction amplitude index, similar to the ejection fraction index used in the diagnostic of overall heart health. The conception of the model and the method used to acquire a contraction index from simulated and clinical data is presented and discussed.

4.2 MATERIAL AND METHODS

4.2.1 3D coronary tree model

The central element in our reconstruction method from single-plane images is the *3D coronary tree model.* This coronary tree model is based on the data used in two articles by Dodge *et al.* [17, 16] where the 3D locations, obtained using biplane angiography, of 102 points along the coronary tree of 37 normal subjects, were measured. The point locations are based on trisected artery segments. The segments are delimited by anatomical landmarks like artery bifurcations. The different reference points were distributed along the right and left coronary arteries and also along the main branches and their secondary tributaries.

We constructed our 3D coronary tree model using a subset of the Dodge *et al.* data. Only the reference points along the major left coronary branches (LCA) and right coronary branches (RCA) were considered because the selected points had to be present for every subject. We ended up with 26 subjects matching our selection criteria, which we will refer to as the *subject models* . Using the nomenclature defined

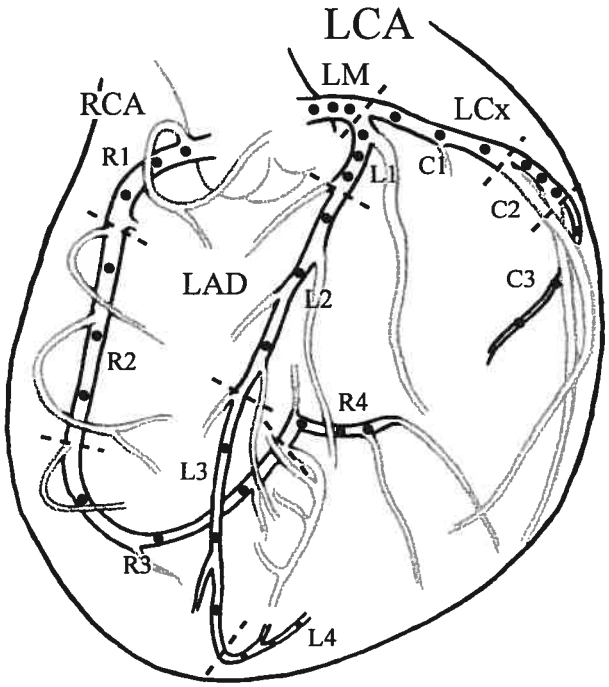

FIG. 4.1. **Reference point locations along the right and left primary coronary arteries. From Dodge *et al.* original data (gray section), only the right coronary artery (RCA), the left main (LM), left circumflex (LCx) and left anterior descending (LAD) arteries were considered in our 3D coronary tree model (dark section). See text for details.**

by Dodge *et al.* the distribution of the 36 points along the coronary branches is as follows, Fig. 4.1 :

- 12 points on the RCA subdivided into the R1, R2, R3 and R4 segments;
- 3 points on the left main artery (LM), the joint base between the left anterior descending artery (LAD) and the left circumflex artery (LCx);
- 12 points on the LAD subdivided into the L1, L2, L3 and L4 segments;
- and 9 points on the LCx subdivided into the C1, C2 and C3 segments.

Refining the method described in a previous article [69], the model definition of the 3D coronary tree model is normalized using global and local components. The global

component refers to a transformation that is applied to all the points composing the model, while the local component is a more subtle transformation specific to each of the model points.

Global component

The global component attenuates inter-subject variations, like heart size, and relative body position during data acquisition. The steps involved in the elaboration of the global component can be described as follows :

A well-formed subject is chosen as a *reference subject*, where well-formed is defined as a subject with clearly defined arterial branches.

The *reference subject* is fitted, with affine transformations (translation, rotation and scaling), to each of the other subjects, the *target subjects*. We use a simulated annealing technique to minimize the sum of the euclidean distances between corresponding points of the *reference subject* and the *target subject*. The objective function used is $\sum_{i=1}^{n} \|\mathbf{M} \cdot \mathbf{P}_i^r - \mathbf{P}_i^t\|^2$, where $\mathbf{P}_i^r$ and $\mathbf{P}_i^t$ are respectively the 3D *reference subject* and *target subject* points, and n is the total number of 3D reference points. The matrix $\mathbf{M}$ is the transformation matrix made up of the rotation matrices around the x, y and z axes, an isotropic scaling parameter and a translation vector along the 3 orientation axes [22].

The global component in the definition of our model is obtained by applying to the *reference subject* the average rotation, scaling and translation parameters found in the minimization process. This gives us the *adjusted reference subject*.

For instance, by selecting subject number 12 as the *reference subject*, we found rotation parameters around the x, y and z axes of -0.02, 0.09 and -0.30 radian respectively (-0.87, 5.06, -17.27 degrees). The scaling factor was 1.02 and the translation along the x, y and z axes have values of 0.54, 0.28 and 0.13 *cm* respectively. The transformation parameter values are generally rather small, depicting the fact the variance of the *subject models* is low.

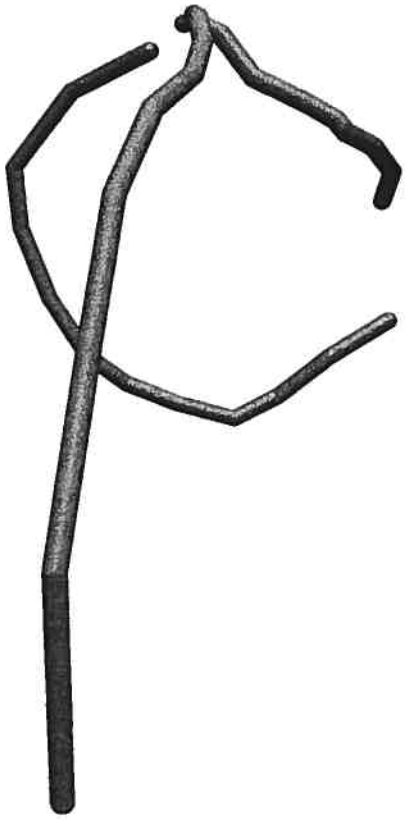

FIG. 4.2. **3D coronary tree model. 3D coronary tree model obtained when using subject number 12 as the reference subject with an angle of view similar to the one in Fig. 4.1**

Local component

The local component attenuates the specific characteristics caused by the choice of the *reference subject*. The local component in our 3D coronary tree model is obtained by applying a specific displacement for each point of the model. This displacement corresponds to the average residual error found between the *adjusted reference subject* and the *target subjects*.

Figure 4.2 shows the final 3D coronary tree model when subject number 12 is chosen as the *reference subject*. Notice that using the global and local components in

the elaboration of the final model makes it very little sensitive to the choice of the *reference subject.*

4.2.2 Heart contraction simulation

To test our 3D heart motion reconstruction, we did some simulations. To simulate an angiogram, we first used one of the 26 *subject models*, the *simulated case.* The *3D coronary tree model* used to recover the 3D heart motion was then defined (see section 4.2.1) using a leave-one-out strategy, excluding the *simulated case* from the case pool.

The *simulated case* was then transformed by rotation, scaling and translation transformations varying in time, to produce a simulated contraction. Different values were used, based on Potel *et al.* [55] findings, ranging from $0 - 30°$ for rotations, $1 - 0.8$ for the scaling factor and $0 - 0.5$ *cm* for translation. This dynamic *simulated case* was projected frame by frame giving the *simulated case projection*, which was the starting point for our recovery method. To stress our recovery method, uniformly distributed random noise varying from $0 - 1$ *cm* was also added around each reference point.

4.2.3 Angiographic images

The clinical cases used to test our 3D reconstruction method came from the Montreal Heart Institute ; they consist of 7 men and 3 women between 55 and 80 years old (65 average) and with ejection fraction varying from 24% to 75% (50.6% average) ; see Tab. 4.1 for details. The single-plane cineangiograms were taken on two different X-ray imaging systems. Three cases were obtained with the Siemens AXIOM-Artis and seven with an Electromed Imaging system. The digital images were saved in the DICOM format. For each case, a complete contraction cycle starting at end-diastole was isolated visually with the help of a custom program, using slow-motion

TAB. **4.1. Clinical cases demographic details**

Patient	Sex	Age	Height (m)	Weight (kg)	Ejection fraction (%)
JO	M	80	1.58	59.5	24
ME	F	58	1.45	60	25
RA	M	65	1.71	80	32
MA	M	61	1.72	87	50
LE	F	61	1.58	77	55
BI	M	79	1.68	66.7	60
EL	M	60	1.78	93.5	60
AL	M	62	1.78	112.5	60
CL	F	70	1.58	70	65
CH	M	55	1.59	84.5	75

and scrubbing (back and forth) techniques, since no synchronized ECG recording was available. During a coronarography examination, the injection of the contrast agent bolus is done separately for the left and right coronary angiogram. To use both the LCA and RCA together, the images must be registered. Since no registration was done with our clinical case angiograms, only images of the LCA were considered.

In all cases, the reference points used to track the epicardial surface movements were located along the LM, LAD (excluding segment L4) and LCx arteries, giving a total of 21 reference points; see Fig. 4.1. In some angiograms, camera movement was detected and was corrected by lateral translations.

4.2.4 3D heart contraction recovery method

To follow the 3D heart movement from the projected reference points along the coronaries, some assumptions are made about camera parameters. The center of projection is placed at the center of the projection plane, the angiogram.The focal distance

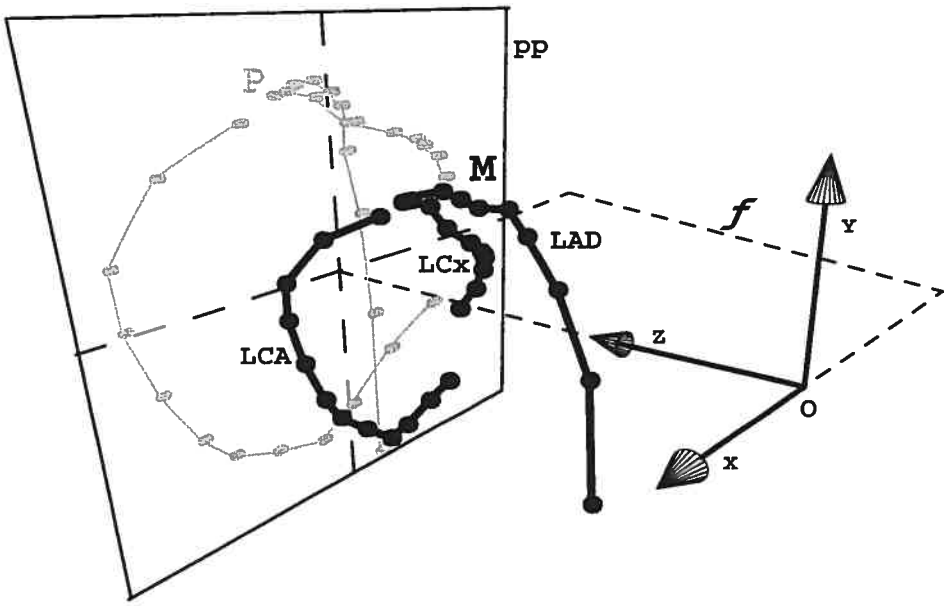

FIG. 4.3. **Projection geometry of heart contraction recovery method. The 3D model (M), composed of the RCA, LAD and LCx, is placed between the source of projection (O) and the projection plane (pp), on which the reference points projection (P) is found. f is the focal distance. See text for details.**

f, the distance between the projection plane and the X-ray source, is determined using information either from the DICOM format, when available, or from specifications of the angiography apparatus, see Fig. 4.3. The projection plane was also scaled to remove heart size differences or magnification adjustments used on the angiographic apparatus. The projection plane scaling value was chosen so that the first frame in the contraction sequence had the same size as the projection of the *3D coronary tree model.*

In order to follow the heart motion, the projection of the model is fitted to the clinical cases with the simulated annealing technique. The objective function used is

$$\sum_{i=1}^{n} \mathbf{p^c}_i - \mathbf{p'}_i = 0, \tag{4.1}$$

where n represents the number of reference points of a simulated or clinical image,

$\mathbf{p^c}_i$ is the measured point location on the angiogram of case i and $\mathbf{p'}_i$ is a projected point location of the *3D coronary tree model*. Two geometric projection models were tested : the full-perspective camera model (FP) or pinhole model

$$\mathbf{p'^{FP}}_i = [fX'_i/Z'_i, fY'_i/Z'_i]^T, \tag{4.2}$$

and the weak-perspective camera model (WP) [79],

$$\mathbf{p'^{WP}}_i = [f/\overline{Z'}X'_i, f/\overline{Z'}Y'_i]^T. \tag{4.3}$$

In both equations, points $\mathbf{P'}_i = [X'_i, Y'_i, Z'_i]^T$ are the results of the transformation $\mathbf{P'}_i = \mathbf{M}\cdot\mathbf{P}_i$, $\mathbf{P}_i$ being the *3D coronary tree model* point locations. The transformation matrix, $\mathbf{M} = \mathbf{R}\cdot\mathbf{T}\cdot\mathbf{S}$, is the composition of the rotation, translation and scaling matrices. Contrary to FP, in WP the location of projected points do not depends on individual depth coordinates but rather on the average depth information, $\overline{Z'}$ is defined as $\frac{1}{n}\sum_{i=1}^{n} Z'_i$. Even if this is an approximation, the WP has the advantage of linearizing the FP equation. Besides, when reconstructing the heart movement in FP using rotation, translation and scaling, the depth translation parameter $\mathbf{T}_z$ must be set to zero. This is because translating a point away or toward the center of projection gives the same result than applying a decreasing or increasing scaling factor respectively. For these reasons, the WP projection model was preferred over the FP model.

4.3 RESULTS

4.3.1 Heart contraction simulation

As explained in Sect. 4.2.2, we created *simulated case projections*. Our goal is to recover the scaling parameter, which is our contraction index. Therefore, comparing the scaling factor, used in the construction of the *simulated cases*, to the recovered scaling parameter found by our method, gives a quantitative evaluation on the efficacy of our reconstruction method. For each of the 25 *subject models* (one of the

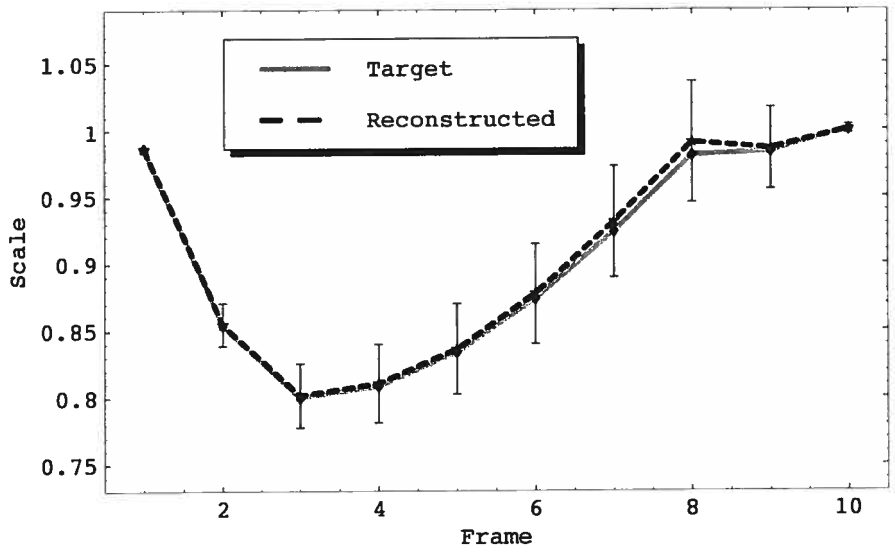

FIG. **4.4. Reconstructed scaling parameter. Comparison between the simulated and the average reconstructed scaling parameter of 25 of the** *subject models.* **The error bar represents two standard deviations.**

subjects constituted the *3D coronary tree model*), we created different *simulated case projections.* The simulated contractions were spread over 10 frames and were obtained by varying the value in the following parameter ranges : $\mathbf{R}_x : \ 0-5°; \mathbf{R}_y : \ 0-30°; \mathbf{R}_z : \ -5-0°; \mathbf{T}_x, \mathbf{T}_y, \mathbf{T}_z : \ 0-0.5 \ cm$ and $\mathbf{S} : \ 1-0.8$. Figure 4.4 represents the average and the standard deviation of the reconstructed scaling parameter compared to the simulated scaling parameter. The quality of fit is expressed by an R^2 of 99.8% ($P < 1\%$).

To stress the reconstruction method we added random noise to every point in the *simulated case.* Using the same transformation parameters, the noise was spread over an increasing spherical volume : from 0 to 1 *cm* in diameter around the reference points along the coronaries. Figure 4.5 represents the variation, over increasing noise levels, of the regression coefficient between the simulated and the average reconstructed scaling parameter. It can be seen that R^2 goes from 99.8% to 96.6% as the noise

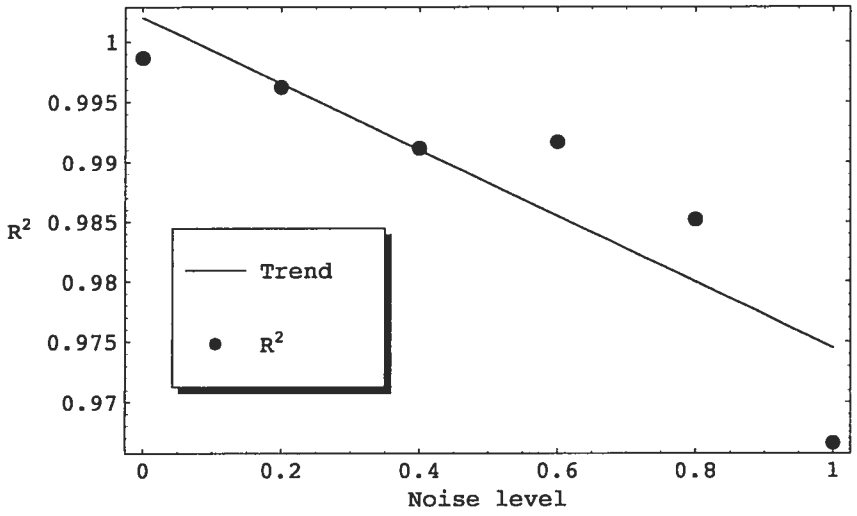

FIG. **4.5. Evolution of the average reconstructed scaling parameter over different noise level. The regression coefficient between the average reconstructed and simulated scaling parameter is plotted against increasing noise level. The average is done over the 25** *subject models.* **As expected, the trend of the regressions decreases as the noise level increases.**

level goes from 0 to 1 *cm.*

4.3.2 Clinical cases

The application of our heart motion reconstruction method on clinical cases was similar to the simulated cases except for certain specific differences described below.

During a coronarography examination, the injection of the contrast agent bolus is done separately for the left and right coronary angiogram. To use both the LCA and RCA together, the images must be registered. Since no registering was done with our clinical case angiograms, only the LCA was used when reconstructing the scaling parameter.

With clinical cases, the scaling parameter responsible for the heart contraction, is unknown, hence it cannot be directly compared to the reconstructed scaling pa-

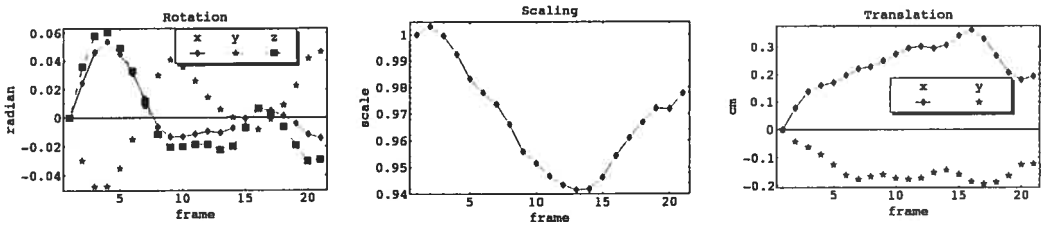

FIG. **4.6. Typical reconstruction of rotation, scaling and translation parameters. Reconstruction of patient** AL**, see Tab. 4.1**

rameter. To get an estimate of the clinical case scaling parameter we used instead the ejection fraction measured by a physician for each case during a ventriculography examination. Using a simple *mathematical contraction model* we were able to linearize the relation between the ejection fraction and the scaling parameter. In our *mathematical contraction model* the heart is represented by an hollow ellipsoid and the pericardium volume is kept constant throughout the contraction cycle; see Appendix 4.6 for details.

Using rotation, translation and scaling transformation parameters, the reconstruction of the clinical-cases heart movement was realized, giving satisfactory results for 5 out of 10 cases; see Fig. 4.6. However, in two cases the scaling was reversed : instead of having a concave curve shape, contraction followed by dilation, the curve was convex, see Fig. 4.7(a). In the three other cases, the scaling curve follows an erratic pattern, see Fig. 4.7(b).To alleviate such problems and considering that translation and rotation are usually small, a second round of reconstructions was undertaken by dropping the rotation and translation parameters to reduce the number of degrees of freedom, using only the scaling parameters. Since the minimization process depends on the location of the center of contraction, it was placed in the left ventricle slightly shifted toward the apex of the heart, as in Potel *et al.* [56, 55]. When using only the scaling parameter in the reconstruction process, every reconstructed cases presented

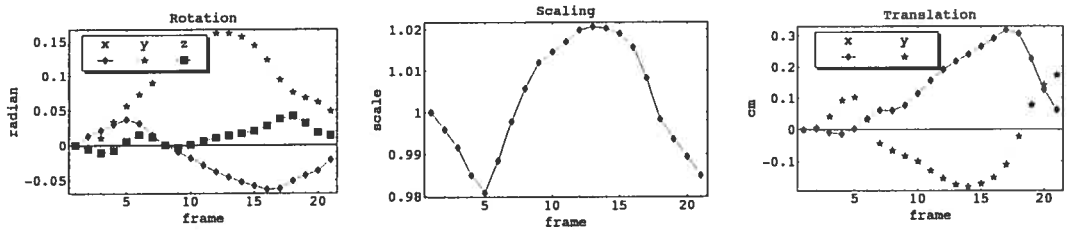

(a)

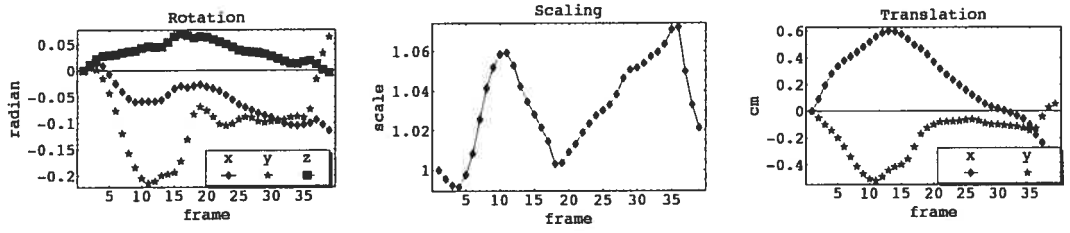

(b)

FIG. **4.7. Atypical scaling curve reconstruction. When the reconstruction is done using the parameters from scaling, rotation and translation transformations the scaling curve presents an atypical shape. For the reconstruction of patient JO the scaling curve presents more of a dilation than a contraction, (a). In the reconstruction of patient BI the scaling curve presents an erratic variation, (b).See Tab. 4.1 for a description of the patients.**

a typical contraction curve, see Fig. 4.8.

Figure 4.9 represents the relation between the (minimum) reconstructed scaling parameter and the ejection fraction with the theoretical trend based on our heart contraction mathematical model. By linearizing the relation between the reconstructed scaling parameter and the measured ejection fraction, using a *mathematical contraction model*, we were able to obtain a correlation of $R^2 = 57\%$ with $P < 1\%$.

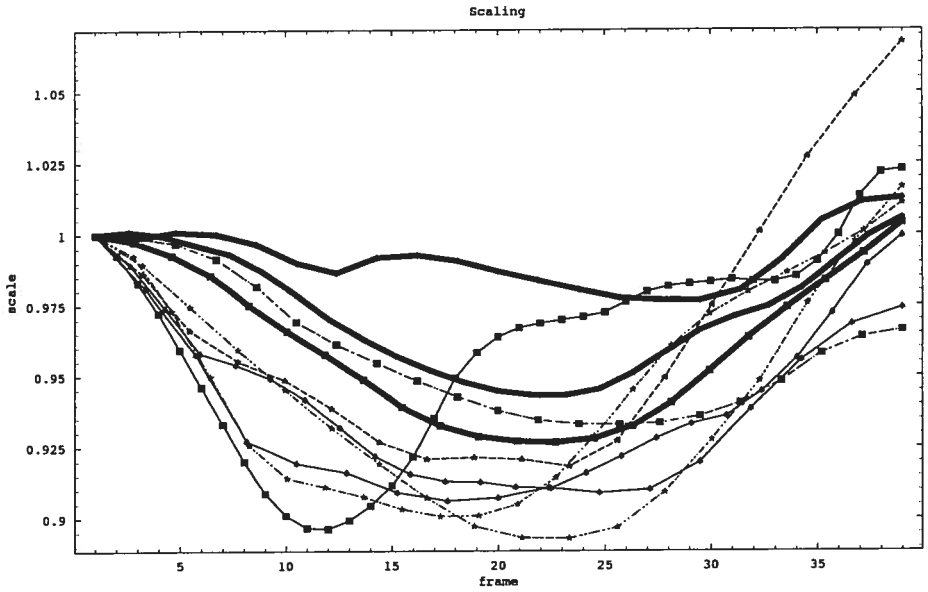

FIG. **4.8. Contraction curves reconstruction. The curves represent the reconstructed contraction of the 10 clinical cases. The thick curves correspond to the 3 cases having an ejection fraction less than 50%.**

4.4 DISCUSSION

4.4.1 Heart contraction simulation

As expected, the correlation, between the scaling factor used for the simulated contraction and the one obtained by the reconstruction, decreases with the noise level, from $R^2 = 99.8\%$ to 96.6% ($P < 1\%$); see Fig. 4.5. The average of the scaling parameters over the 25 *subject models* might explain partially the high correlation even in the presence of relatively high noise, due to the average smoothing out individual variations.

Since only the LCA was considered in the clinical cases, we also tested the effects of reconstructing from the LCA versus RCA-LCA. Without adding noise, the correlation between the average reconstructed scaling parameter and the simulated

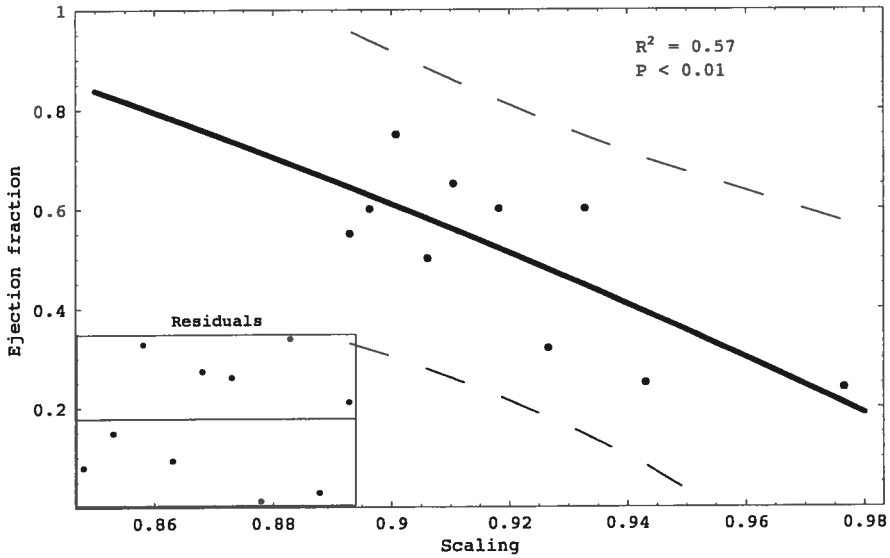

FIG. **4.9. Correlation between the reconstructed scaling parameter and the ejection fraction. The thick line represents the relation according to our** *mathematical contraction model.* **Dashed lines delimit the 95% confidence region.**

target remains still high ($R^2 = 98\%, P < 1\%$) when using only the LCA, compared to $R^2 = 99.8\%$ ($P < 1\%$) when using the LCA-RCA.

4.4.2 Clinical cases

The difficulties encountered during the reconstruction process undertaken from clinical cases, when using all 6 parameters from rotation, translation and scaling transformations, might be explained by the misregistration of reference points. In some cases, anatomical landmarks were difficult to identify. It might also be noted that the spatial distribution of reference points is not uniform over the epicardium, being more concentrated near the root of the arterial tree than the apex (see Fig. 4.1), probably creating an ill-conditioned reconstruction process.

During the reconstruction process, each of the 6 parameters has the same weight. Although constraints were imposed (for example, rotations were limited to $\pm\pi/8$

radians and the scaling parameter was positive), no *a priori* information on the behavior of the parameters was given. In specific cases, it has been observed that a shift in one parameter, inverts the scaling curve until the system finds a new stable configuration. It is as if, at a certain point a parameter becomes dominant in the minimization process. This is typical of what happens when over-parameterizing a model. In such cases, it is well known that reducing the number of parameters may improve the conditioning of the problem and the robustness of the solution. This is why we focused on the scaling parameter afterward. As previously noted, since the minimization process depends on the center of contraction, we obtained the best scaling curve shapes and the best relation between the scaling parameter and ejection fraction, Fig. 4.9, by placing it in the left ventricle slightly shifted toward the apex of the heart Although Potel *et al.* found that using a moving center of contraction best describes the radial heart wall motion, we used a fixed center of contraction.

4.5 CONCLUSION

We have presented a model-based method to recover a heart contraction index, similar to the ejection fraction index, from single-plane coronary cineangiograms. The method relies on the minimization of the RMS distances from reference points along the main arteries and the projected points of a model.

In simulations, our method recovered more than 95% of the original contraction, expressed as a scaling parameter. Using 10 clinical cases, we compared our contraction index to the measured ejection fraction and found a coefficient of determination of 57% ($P < 1\%$).

Difficulties were encountered while reconstructing the 3D heart contraction of clinical cases. They were resolved by using an isotropic scaling transformation to explain the observed motion. Other solutions might come from the use of more reference points on the epicardium, with more LCA branches and/or a registered RCA.

A moving-center-of-contraction model could also mimic more accurately the heart contraction. However we believe that more complex deformation models (e.g. with torsion or other extensions) would probably not be suitable because of the poor conditioning of this problem.

Our heart contraction index is somewhat related to the ejection fraction measure, both expressing an heart contraction variation, but they differ by the fact that the ejection fraction represents the endocardial volume variation and our heart contraction index represents the epicardial contraction variation. Both of these indices might present complementary information. Furthermore, our heart contraction index proposes a new usage for the information contained in coronarography.

4.6 APPENDIX

In order to compare our reconstructed heart movement, expressed by a scaling factor S of the epicardium, with the ejection fraction of the different clinical cases, which represents a measure of volume variation of the endocardium, a *mathematical contraction model* was devised. It is based on simple assumptions (see Fig. 4.10) :

- the heart can be represented by a hollow thick ellipsoid ;
- the myocardium is of constant volume throughout the contraction cycle.

Let us rewrite the ellipsoid volume formula [7] expressed according to an isotropic scaling factor S,

$$V_S = \frac{4}{3}\Pi abcS^3, \tag{4.4}$$

a, b and c being the ellipsoid semi-axis lengths at end-diastole. The heart left ventricle is represented as a thick ellipsoid shell, representing the myocardium. Its initial volume represents the difference between the epicardial and the endocardial volumes at end-diastole, with scaling factors of $S_d = 1$ and S_m respectively. Using Eq. (4.4) we find the volume of the myocardium expressed in terms of the scaling factors to be $V_m = \frac{4}{3}\Pi abc(1 - S_m^3)$. It is this value that is kept constant throughout the contraction

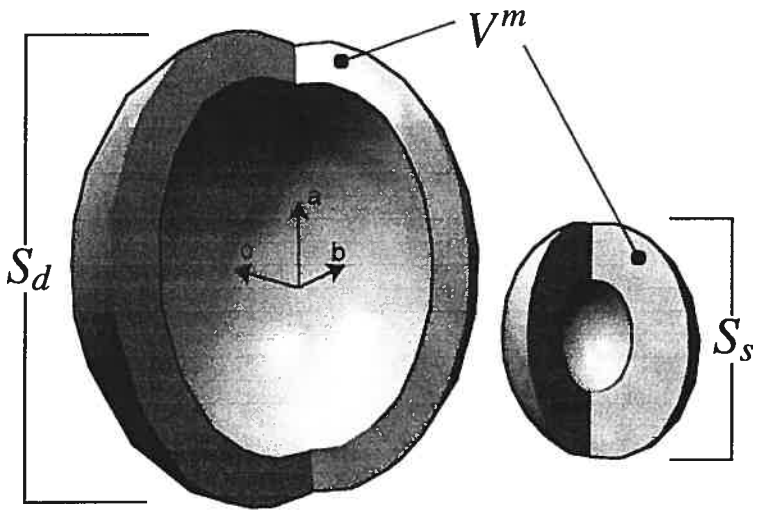

FIG. **4.10. Heart contraction mathematical modelization. In our heart** *mathematical contraction model*, **the heart is represented by an ellipsoid and as the heart contracts from end-diastole to end-systole, the volume of the myocardium (V^m) is kept constant. S_d, endocardial scaling factor at end-diastole. S_s, endocardial scaling factor at end-systole. a, b, c, ellipsoid semiaxes.**

cycle. Next, we define the endocardial volume according to the epicardial scaling factor as $V'_S = V_S - V_m$. Finally, we substitute it in the classical ejection fraction formula to obtain

$$EF = \frac{V'_{S_d} - V'_{S_s}}{V'_{S_d}} \tag{4.5}$$

$$= \frac{1 - S_s^3}{S_m^3} \tag{4.6}$$

where V'_{S_d} is the volume expressed as the scaling factor S_d at the end-diastole and V'_{S_s} is the volume expressed as the scaling factor S_s at the end-systole.

Equation 4.6 represents the cubic relation between the ejection fraction EF and the scaling factor S_s at the end-systole, moderated by the myocardial scaling factor fixed at end-diastole S_m.

ACKNOWLEDGMENTS

The authors thank Dr. Jacques Lesperance of the Montreal Heart Institute, for his help in the selection of the clinical case images. The authors also express their gratitude to Dr. J. Theodore Dodge Jr for having so generously shared his data used in the construction of the model.

Chapitre 5

RECONSTRUCTION 3D DU CHEMIN DU CATHETER IVUS

L'étude de la reconstruction 3D du chemin du cathéter IVUS, est abordée dans la présente section par une revue de littérature.

Les images IVUS étant de nature tomographique, présentent les vaisseaux en coupe ; Fig. 2.5. Il est donc difficile d'avoir une vue d'ensemble du segment imagé. Puisque durant le retrait du cathéter une séquence d'images est enregistrée, un empilement des images peut produire une reconstruction 3D. Au début des années '90, Rosenfield *et al.* et Roetland *et al.* réalisaient de telles reconstructions 3D du chemin parcouru durant le retrait du cathéter lors d'une échographie endovasculaire [62, 61] ; Fig. 5.1. Le problème de cette méthode tient du fait que l'empilement ne tient pas compte de la courbure du vaisseau, ce qui génère des variations volumétriques. Le volume d'un fragment placé au côté intérieur d'une courbure sera surestimé, tandis que le volume d'un fragment placé sur le côté extérieur sera sous-estimé.

Afin de donner aux images IVUS un volume qui tient compte de la tortuosité des vaisseaux, l'utilisation de l'angiographie fut entreprise simultanément par plusieurs groupes de recherche. Les images angiographiques permettent de positionner dans un référentiel 3D global le chemin du retrait de la caméra IVUS. Les images échographiques sont par la suite alignées suivant ce chemin.

Evans *et al.* réalisent une reconstruction 3D en considérant la courbure des vaisseaux en utilisant l'angiographie pour placer les images IVUS dans un espace 3D global. Leur méthode exige un enregistrement continu du retrait du cathéter IVUS sur un système angiographique biplan ainsi que l'utilisation d'un cube de calibrage [19], Fig. 5.2.

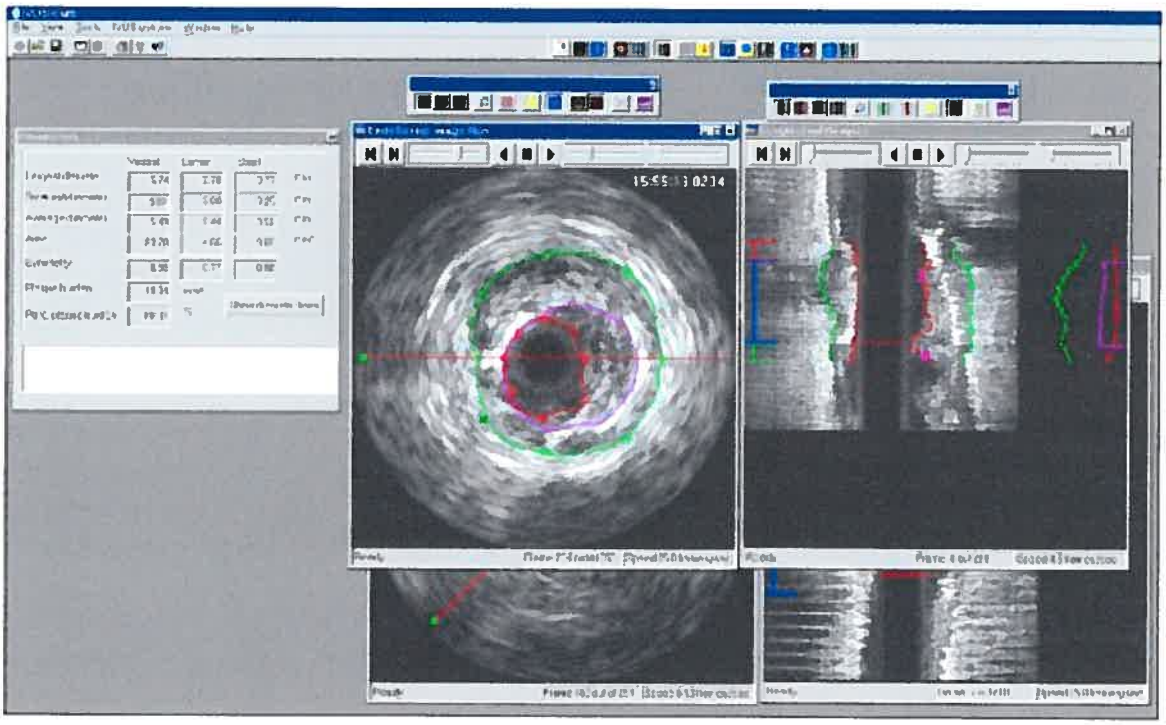

FIG. 5.1. **Exemple d'empilement d'images IVUS aux fins de reconstruction 3D. D'après Dijkstra [38].**

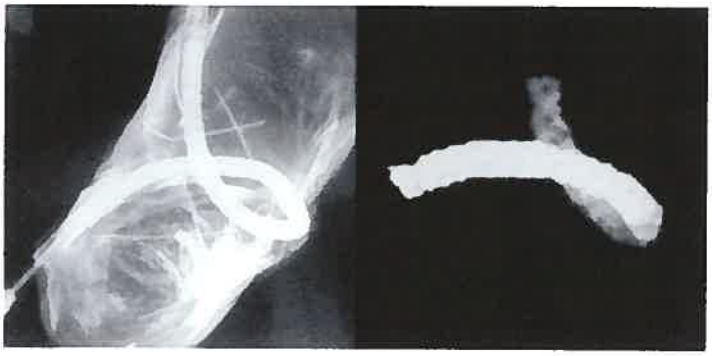

FIG. 5.2. **Exemple de reconstruction 3D par fusion des images IVUS et angiographiques. A : Fantôme ; B : reconstruction du chemin du cathéter. D'après Evans *et al.* [19].**

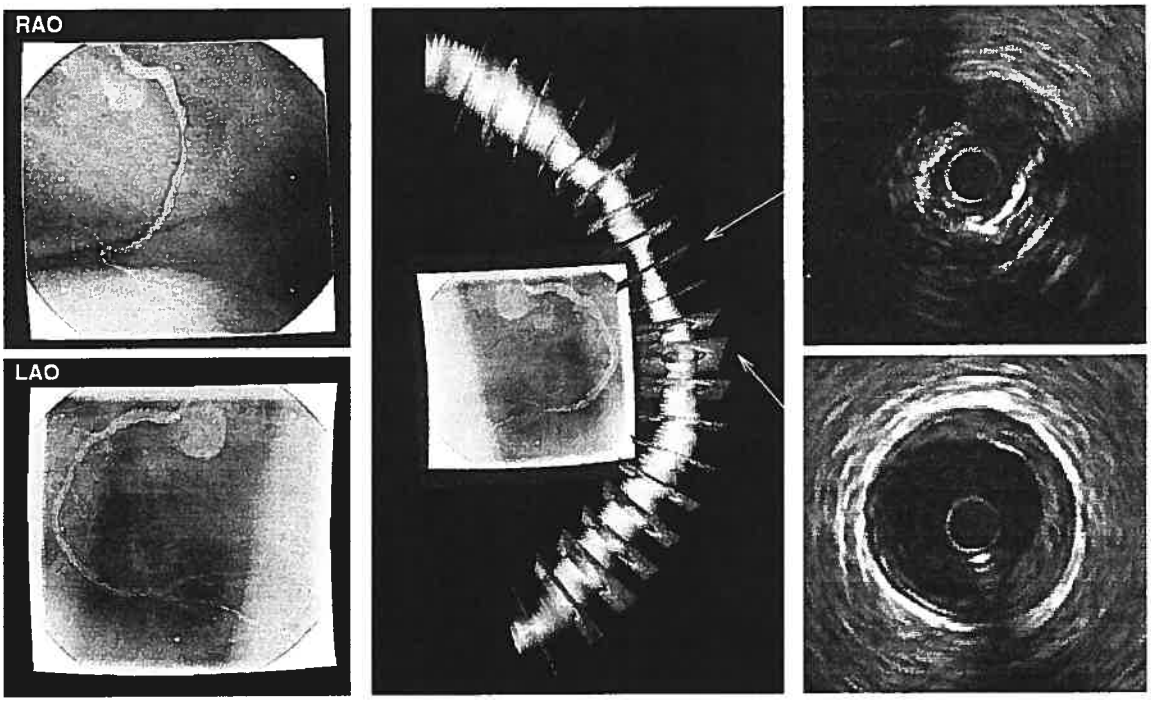

FIG. **5.3. Alignement des images IVUS par rapport à la courbure des vaisseaux. À gauche : angiogrammes ; à droite : images IVUS ; au centre : fusion des deux modalités. D'après Wahle** *et al.* **[82].**

Un autre groupe d'étude développe une méthode de reconstruction ANGUS (ANGiography ivUS) qui ne requiert qu'une prise d'angiogrammes au début du retrait du cathéter. Le système angiographique biplan a quand même besoin d'être calibré à l'aide d'un cube de calibrage. L'orientation tout au long du retrait, est estimée à l'aide d'une fonction 3D de Fourier. Leur méthode requiert une vitesse constante de retrait du transducteur [36, 75, 5, 76].

Un groupe rattaché à l'université d'Iowa développe une approche qui utilise le système biplan, mais ne requiert pas de calibrage. Des résultats sont obtenus, où l'erreur dans l'ajustement des images IVUS sont de l'ordre de 2.5% en relation avec la distance parcourue du retrait [87, 58, 57, 84, 83, 86, 45], Fig. 5.3.

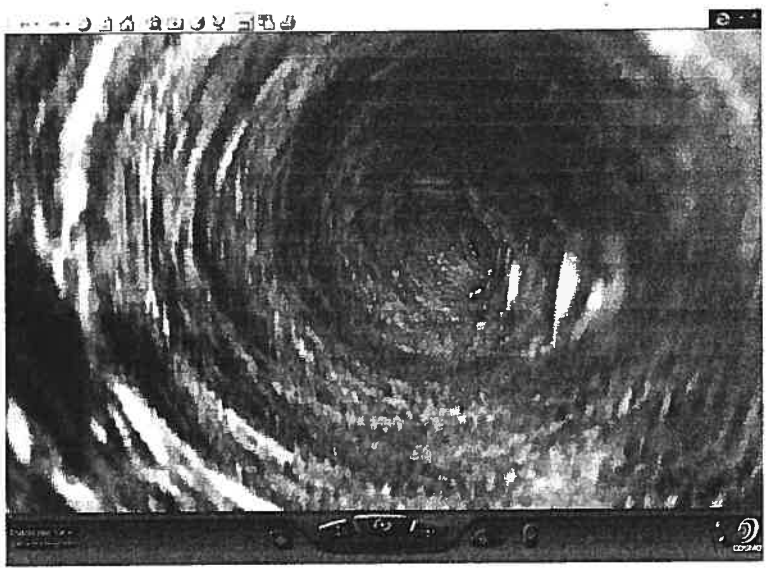

FIG. **5.4. Parcour endoscopique virtuel. D'après Wahle** *et al.* **[82].**

Cothren *et al.* [67, 68, 15] ont mis au point une méthode basée sur l'angiographie biplan, mais qui ne nécessite pas un retrait constant du transducteur.

D'autres problèmes dans la fusion des modes d'imagerie IVUS et angiographique portent sur la torsion et la position axiale des images IVUS par rapport au vaisseau. Le cathéter subit des torsions axiales si le vaisseau, dans lequel se produit le retrait, n'est pas sur un même plan. De plus, la position du cathéter dans le vaisseau dépend de la courbure de ce dernier. Le cathéter étant quelque peu rigide, occupera le plus long rayon dans la courbure du vaisseau. Des corrections sont donc nécessaires et ont été adressées dans diverses recherches [85, 76].

Les recherches récentes sur la reconstruction 3D des images IVUS, ajoutent l'aspect temporel, ce qui permet d'aborder une étude hémodynamique. En effet, la relation entre zone de stress et présence de plaques vasculaires est un sujet d'intérêt grandissant pour l'étude des maladies vasculaires [54, 53, 81, 88]. Pour ce faire, Whale *et al.* ont développé un système de réalité virtuelle où l'opérateur peut se déplacer à l'intérieur des vaisseaux [82]. Le système permet l'étude de la dynamique des fluides

et du stress de cisaillement subi par les vaisseaux, en donnant une teinte aux surfaces selon les valeurs de cisaillement ; Fig. 5.4.

Toutes ces méthodes nécessitent l'utilisation de systèmes angiographiques biplans. Ces systèmes sont de manipulation complexe et peu accessibles dans le milieu clinique. Une approche novatrice de reconstruction 3D du chemin parcouru par le transducteur IVUS lors de son retrait endovasculaire, n'utilisant qu'un système angiographique monoplan, est décrite dans le chapitre suivant.

Chapitre 6

3D TRAJECTORY ASSESSMENT OF AN IVUS TRANSDUCER FROM SINGLE-PLANE CINEANGIOGRAMS : A PHANTOM STUDY

Cet article a été soumis le 14 janvier 2004, aux fins de publication dans la revue IEEE Transactions on Biomedical Engineering

Denis Sherknies, Jean Meunier, Rosaire Mongrain et Jean-Claude Tardif

Soumis à : IEEE Transactions on Biomedical Engineering

Abstract

The recovery of the 3D path of the transducer used during an Intravascular Ultrasound (IVUS) examination is of primary importance to assess the exact 3D shape of the vessel under study. Traditionally, the reconstruction is done by simply stacking the images during the pullback, or more recently using biplane angiography to recover the vessel curvature. In this paper we explain, how single-plane angiography can be used with two projection models, to perform this task.

Two types of projection geometry are analyzed : weak-perspective and full-perspective. In weak-perspective projection geometry, the catheter path can be reconstructed without prior transducer depth information. With full-perspective projection geometry, precise depth location of reference points are needed in order to minimize the error of the recovered transducer angle of incidence.

The transducer angulation reconstruction is based on the foreshortening effect as

seen from the X-ray images. By comparing the measured to the true transducer length, we are able to get its incidence angle. The transducer trajectory is reconstructed by stitching together the different estimated angulations obtained from each image in a cineangiogram sequence.

The method is described and validated on two helical vessel phantoms, giving on average a reconstructed path that is less than $2mm$ distant from the true path when using full-perspective projection.

Keywords : IVUS, single-plane angiography, phantom, 3D reconstruction.

6.1 INTRODUCTION

Because of their complementary nature, the two imaging modalities, X-ray angiography and intravascular ultrasound (IVUS), are increasingly being studied and used together. Angiography provides a means to display the overall vessel morphology but provides limited assessment of plaque distribution [48], while IVUS gives an accurate composition of the vessel cross-section [93] without producing knowledge on absolute orientation.

In order to provide a more informative assessment of the vessel lumen and plaque dimensions, the 2D IVUS images are reconstructed in 3D by stacking the different images taken during the pullback of the transducer. In early research efforts, the images were stacked so as to create a straight tube [61]. By neglecting the vessel curvature this method introduced incorrect volumetric representation, mainly where vessel curvature is high [5]. Biplane cineangiography was later used to recover the transducer orientation and precise 3D localization [76, 81, 45], but these apparatus are complicated to operate and are not always available in clinical centers.

In this paper, we extend a method previously developed [71, 70] that enables the recovery of an IVUS transducer orientation from a single-plane projection (monocular vision), thus permitting reconstruction of the catheter path curvature. The process of

incidence angle recovery is based on the foreshortening effect of the IVUS transducer as seen on the angiogram. By comparing the known length of the transducer with the measured length of its projection, it is possible to obtain the incidence angle of the transducer. By combining a sequence of images, the 3D catheter (transducer) path can then be reconstructed.

First, we lay out the mathematical foundations for the 3D localization of a segment based on its projection. Then we describe the method used for the 3D path reconstruction from 3D segments. Results from helical phantom path reconstructions are later presented with experimental and theoretical error analysis.

6.2 MATERIAL AND METHODS

6.2.1 Depth recovery method using different camera models

We analyze the recovery of the IVUS transducer from a full-perspective projection, a weak-perspective projection and an orthographic projection model. The conventions used in this article are as follows (Fig. 6.1) : the origin of the coordinate system axes is placed at the X-ray emission source of the imaging system; the axes are oriented so that the projection plane is perpendicular and centered along the z axis; the projection plane is coincident with the angiogram; the segment $S = [\mathbf{P}_1, \mathbf{P}_2]$ represents the transducer location at a certain moment during a pullback and the segment $s = [\mathbf{p}_1, \mathbf{p}_2]$ is the projection of the transducer on the angiogram. The angulation of the transducer is defined in relation to the projection plane, a transducer parallel to the projection plane is said to be at 0°, and at 90° when perpendicular to the projection plane.

Full-perspective projection model

In order to derive the mathematical formulation for the 3D recovery based on the 2D projection, we first define some fundamental equations.

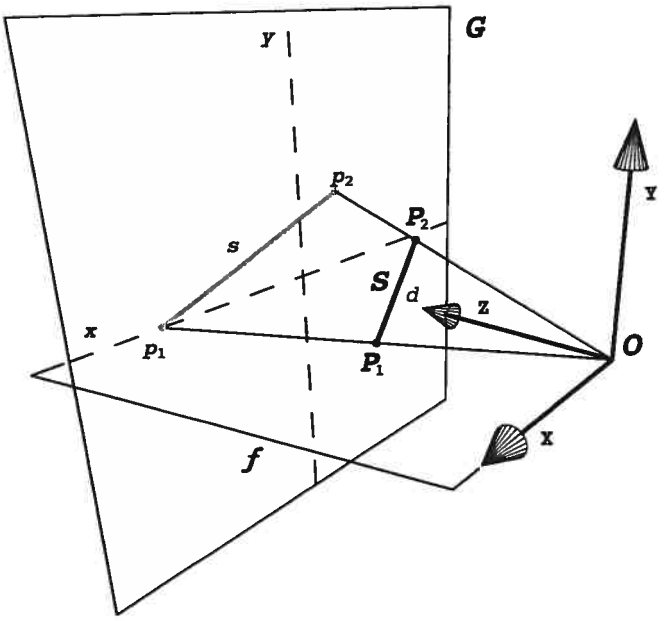

FIG. **6.1. Full-perspective projection geometry. Segment S is projected on the projection plane G as segment s. In full-perspective, all projectors originate from the origin O.**

If we define $\mathbf{P}_i = [X_i, Y_i, Z_i]$ as a 3D point and $\mathbf{p}_i = [x_i, y_i]$ a 2D point, the relation between $\mathbf{P}_i$ and its projection $\mathbf{p}_i$, for a pinhole camera model, is given by

$$x_i = f\frac{X_i}{Z_i} \tag{6.1}$$

and

$$y_i = f\frac{Y_i}{Z_i}, \tag{6.2}$$

where f is the focal distance. We assume here that the camera is placed at the origin in the 3D space, that the projection plane is perpendicular to the Z axis and centered on it (Fig. 6.1). Another fundamental equation is the euclidean distance formula which states that the distance between two points $\mathbf{P}_1 = [X_1, Y_1, Z_1]$ and $\mathbf{P}_2 = [X_2, Y_2, Z_2]$ can be found with

$$d = \sqrt{(X_2 - X_1)^2 + (Y_2 - Y_1)^2 + (Z_2 - Z_1)^2}. \tag{6.3}$$

Expressing (6.1) as a function of Z_2, we obtain

$$Z_2 = f\frac{X_2}{x_2}. \tag{6.4}$$

Using (6.4) to substitute Z_2 in (6.2) and expressing it as a function of Y_2 gives

$$Y_2 = y_2\frac{X_2}{x_2}. \tag{6.5}$$

Substituting (6.4) and (6.5) in (6.3) gives

$$d = \sqrt{(X_2 - X_1)^2 + (y_2\frac{X_2}{x_2} - Y_1)^2 + (f\frac{X_2}{x_2} - Z_1)^2}, \tag{6.6}$$

which solved for X_2 gives

$$X_2 = \frac{x_2 a \pm \sqrt{x_2^2(a^2 + bc)}}{b}, \tag{6.7}$$

where

$$\begin{aligned} a &= x_2X_1 + y_2Y_1 + fZ_1, \\ b &= f^2 + x_2^2 + y_2^2, \\ c &= d^2 - X_1^2 - Y_1^2 - Z_1^2. \end{aligned}$$

Knowing the location of two projected points $\mathbf{p}_1, \mathbf{p}_2$, the location of a 3D point $\mathbf{P}_1$ and the distance d between the two 3D points, we are able to find the 3D coordinates of $\mathbf{P}_2$. The abscissa is found using (6.7) and by substituting (6.7) in (6.4) and (6.5), the depth and ordinate coordinates are found.

Since a square root is involved in the resolution of the abscissa of $\mathbf{P}_2$ (6.7), two solutions are possible. The choice between the two is based on an *a priori* knowledge of the problem and is discussed in section 6.4.2.

Weak-perspective projection model

As in the case of full-perspective projection, we assume that the projection plane is perpendicular to the Z axis and centered on it (Fig. 6.2). The weak-perspective

camera model approximates the full-perspective camera model by linearizing it. The projection of each 3D point is not affected by their respective depth coordinates but rather by the average scene depth. Equations (6.1) and (6.2) become

$$x_i = f' X_i \tag{6.8}$$

and

$$y_i = f' Y_i, \tag{6.9}$$

where $f' = \frac{f}{\overline{Z}}$ and $\overline{Z} = \frac{1}{n}\sum_{i=1}^{n} Z_i$, n is the number of points.

Using (6.8) and (6.9), we are able to rewrite (6.3) as

$$Z_2 = Z_1 \pm \sqrt{d^2 - \frac{[(x_2 - x_1)^2 + (y_2 - y_1)^2]}{f'^2}}, \tag{6.10}$$

which gives the depth coordinate of point $\mathbf{P}_2$, X_2 and Y_2 being found from (6.8) and (6.9).

The error introduced by the weak-perspective approximation becomes insignificant when $\overline{Z}$ is 20 times greater than the object depth [79].

Orthographic projection model

In an orthographic projection, discarding the depth coordinate of a 3D point converts it in its projection :

$$x_i = X_i \quad \text{and} \quad y_i = Y_i. \tag{6.11}$$

Using a process similar to the weak-perspective projection model, with the help of (6.11) we rewrite (6.3) as

$$Z_2 = Z_1 \pm \sqrt{d^2 - [(x_2 - x_1)^2 + (y_2 - y_1)^2]}. \tag{6.12}$$

The full and weak perspective camera models were used to recover the 3D path of an IVUS transducer from single-plane angiogram, but the orthographic projection was not used, because it is a crude approximation.

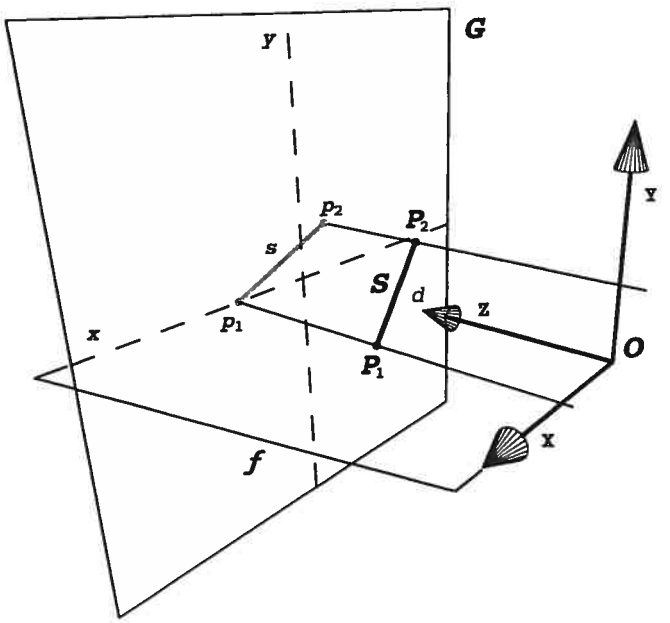

FIG. **6.2. Orthographic and weak-perspective projection geometry. In orthographic and weak-perspective projections, projectors are parallel. Weak-perspective projection can be described as an orthogonal projection followed by an isotropic scaling factor.**

6.2.2 Material

Helical phantoms consisting of a 0.64 *cm* exterior diameter silicon tubing wrapped around beakers were constructed. Wire markers were placed on the phantom, 2 *cm* apart, to provide radio-opaque landmarks. *Phantom A* consisted of a single loop helix of 13 *cm* in height and 10.9 *cm* in diameter, Fig. 6.3(a). *Phantom B* was a double loop helix of 10 *cm* in height and 6.6 *cm* in diameter, Fig. 6.3(b). We selected an helical phantom configuration because it is the simplest geometric entity that presents curvature and torsion. It can be shown that the curvature κ and torsion τ are respectively given by

$$\kappa = \frac{\rho}{\rho^2 + h^2}, \tau = \frac{h}{\rho^2 + h^2} \tag{6.13}$$

where ρ is the radius of the helicoid and h the pitch of the lead of the screw. This allows to assess the method by calculating the curvature and torsion from the 3D

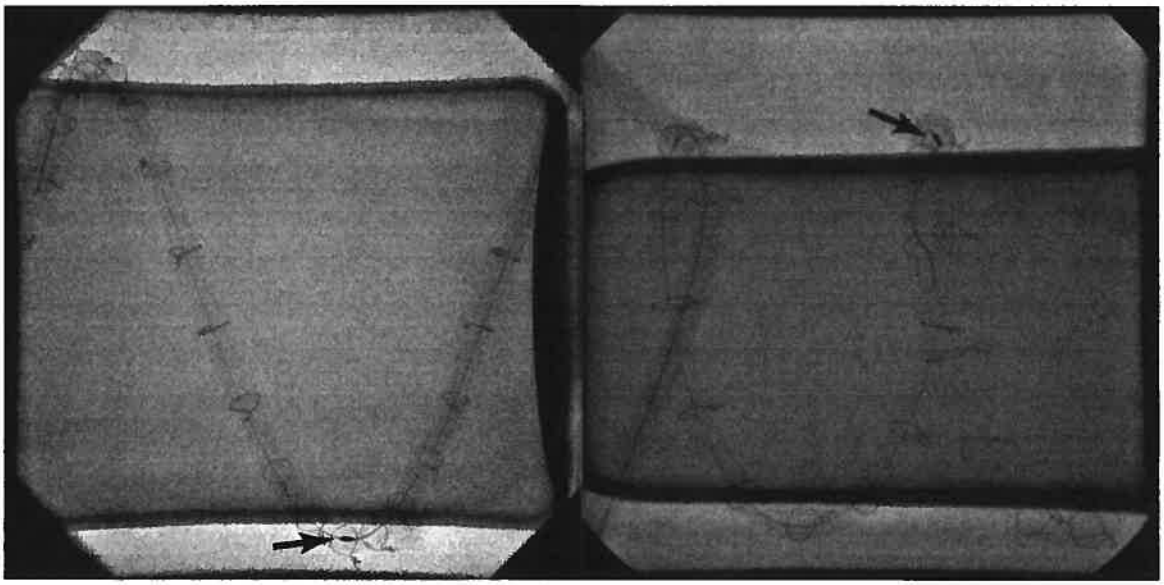

(a) Angiogram of phantom A (b) Angiogram of phantom B

FIG. **6.3. Phantoms Images. Note the transducer presence at the bottom of (a) and at the top of (b). Radio-opaque markers and the catheter guide wire are also visible.**

reconstruction and comparing them to the *a priori* known values.

The IVUS catheter (JOMED Avanar F/X) used for this experiment, measured 2.9 F (0.097 *cm*) in diameter and the transducer length was 0.7 *cm*.

The pullback was done using a JOMED TrackBack II catheter pullback device at a speed of 0.1 *cm*/s over a guide wire of 0.036 *cm* in diameter.

The single-plane cineangiograms were taken on a Siemens AXIOM ARTIS FC X-ray imaging system. The digital images were saved in the DICOM format using the Syngo clinical information system.

The images were obtained by placing the phantom in water to attenuate X-ray intensity. The automatic pullback was recorded on the X-ray imaging system at a rate of 4 fps (frames per second) and at a resolution of 1 024 pixels x 1 024 pixels.

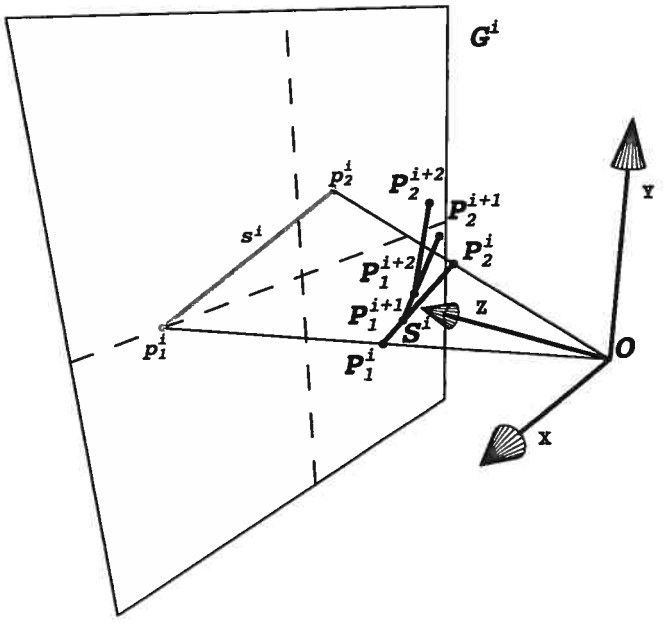

FIG. **6.4. 3D path reconstruction simulation. See text for details.**

The focal distance f was 100 *cm.*

The pullback recorded on *phantoms A and B* was composed of 821 and 818 frames respectively.

6.2.3 3D Path reconstruction method

The first step in the *3D path reconstruction method* is to find the orientation of a 3D segment from its projection, as explained in the description of our *depth recovery method.* In order to reconstruct the 3D path completely, the different reconstructed 3D segments must be stitched together. To describe the *3D reconstruction method,* let us define each image in a cineangiogram as $\mathbf{G}^i$ (Fig. 6.4), where i goes from 1 to n, the number of frame in the cineangiogram sequence. To each image corresponds a segment $\mathbf{S}^i = [\mathbf{P_1}^i, \mathbf{P_2}^i]$, the 3D localization of the transducer tips, and a segment $\mathbf{s}^i$, the transducer projection. The distal extremity, in relation to the transducer pullback direction, is labeled as $\mathbf{p_1}^i$ and the proximal extremity as $\mathbf{p_2}^i$.

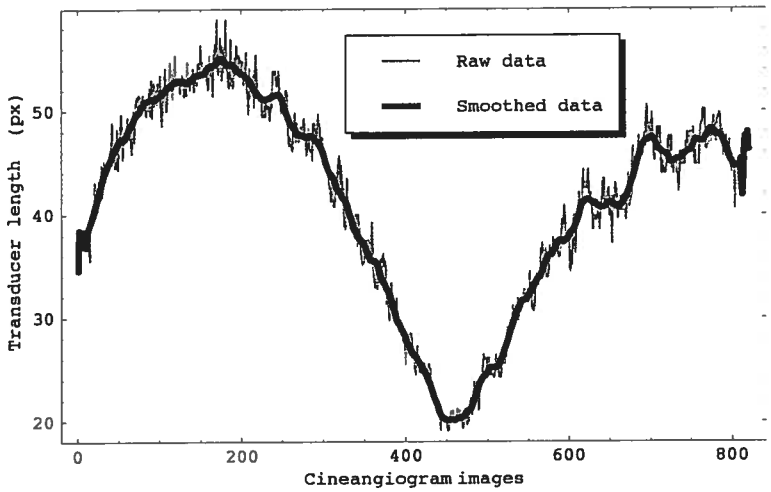

FIG. **6.5. Transducer length. Variation in raw and smoothed measured transducer length for each frame in the cineangiogram of phantom A during the catheter pullback.**

For each X-ray image, each extremity of the transducer was manually registered on the angiograms using a custom program. The point locations of the transducer extremities and data lengths were then smoothed to attenuate the manipulation errors using a 21-image moving average filter, Fig. 6.5.

In order to apply our previously described *depth recovery method* on each segment $\mathbf{s}^i$, we need a good estimation of the depth coordinate of the first point $\mathbf{P_1}^i$ in the recovered sequence. Since the phantom is helical, at one point there exists a frame that represents the transducer at 0° with the projection plane. The frame $\mathbf{G}^i$ containing the longest segment $\mathbf{s}^i$, corresponds to a transducer 3D orientation that is assumed to be parallel to the projection plane. For that frame, the depth coordinate of point $\mathbf{P_1}^i$ is set equal to the depth coordinate of point $\mathbf{P_2}^i$. This allows estimation of the depth coordinate of points $\mathbf{P_1}^i$ and $\mathbf{P_2}^i$.

To estimate the next depth coordinate $\mathbf{P_1}^{i+1}$, on frame $\mathbf{G}^{i+1}$, we approximated the transducer 3D trajectory in a piecewise linear manner and displaced $\mathbf{P_1}^{i+1}$ along the segment $\mathbf{S}^i$ in concordance with the transducer pullback speed. The point $\mathbf{P_2}^{i+1}$

is found using the *depth recovery method.* The process is repeated for every image in the cine-angiographic sequence.

6.2.4 Helical mathematical model

In order to assess the validity of our reconstruction method, we created numerical models of our phantoms. The *helical mathematical models* were positioned by translations and rotations along the three axes, to correctly localize them in the virtual 3D environment. The transformation parameters were found by minimizing the average euclidean distances between the *helical mathematical model* projections and the centerline projection of the phantoms, which correspond to the intersection between the guide wire and the radio-opaque landmarks, measured on image $\mathbf{G}^1$ of each phantom cineangiogram.

6.3 RESULTS

6.3.1 Experimental reconstruction results

Using the previously defined method of reconstruction, we reconstructed the transducer path for the two phantoms using full and weak perspective projection geometry. The reconstructed path length was approximately 25 *cm* for both phantoms. Figure 6.6 shows the 3D representation of the reconstruction in full-perspective for *phantom B.* Once reconstructed the transducer 3D trajectories were compared to the *helical mathematical models* using an average euclidean distance measure in order to assess the precision of reconstruction. Tab. 6.1 gives descriptive statistics of the euclidean distances of the different reconstructions expressed in *cm*, where *WP* and *FP* signifies weak and full-perspective and *% Mean / Diameter* is the average euclidean distances expressed as the percentage of the phantom diameter. The reconstructed paths were also characterized using curvature and torsion curve descriptors, Tab. 6.2.

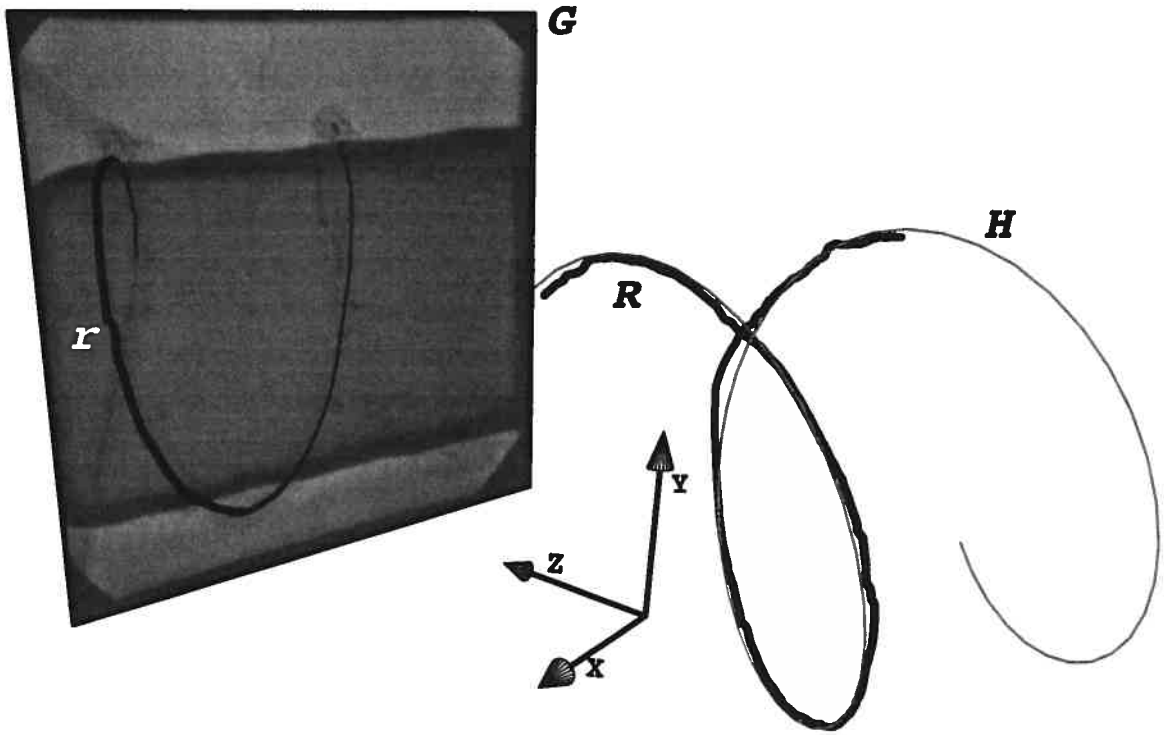

FIG. 6.6. **Reconstruction of the catheter pullback path of phantom B using full-perspective projection. G : angiogram; H : Helical mathematical model; r : 2D measured transducer localization throughout the recorded pullback; R : 3D reconstructed catheter path. Here the axis origin does not represent the center of projection.**

6.4 DISCUSSION

6.4.1 Theoretical error analysis

The precision in the transducer path reconstruction is dependent on the estimated or measured values of many parameters. Here the effects of an error, in the measured projection foreshortening length or in the initial depth localisation in full and weak perspective geometry, is briefly discussed.

Because of the trigonometric nature of the projection geometry, for a constant foreshortening effect, the estimated angular variation of the transducer will depend

TAB. **6.1. Descriptive statistics of the euclidean distances in *cm*, measured between the reconstructed catheter path and the helical mathematical model.**

Phantom	Projection model	% Mean / Diameter	Mean	Median	SD	Min	Max
A	FP	2.10%	0.23	0.16	0.16	0.01	0.57
	WP	4.94%	0.54	0.58	0.23	0.08	0.90
B	FP	1.74%	0.11	0.11	0.07	0.01	0.32
	WP	3.96%	0.26	0.24	0.14	0.04	0.62

FP : Full-perspective ; WP : Weak-perspective.

on its initial angle. In Fig. 6.7, one can see that an error of 10% on the measured projected length of the transducer placed parallel to the projection plane, gives an angular variation of 25.8 ° compared to an angular variation of only 7.6 ° when the transducer is placed at an initial angle of 45 ° with the projection plane. So whatever technique is used to recover the 3D orientation from a projection, the error margin will be greater as the transducer tends to be parallel to the projection plane. This effect can be estimated for an angiogram where the continuous nature of the projected length of the transducer is quantized by the pixel representation. Using typical values for width of view of 10 *cm*, transducer length of 0.5 *cm* and an angiogram resolution of 1 024 x 1 024 pixels, the variation of the projected length would be less than 2% of the transducer length for a ±1 pixel error. At worst, for a transducer oriented at 0 °, this would produce an angular variation of 11 °.

In the full-perspective geometry (Fig. 6.8), a back-projection of two fixed points $s = [\mathbf{p}_1, \mathbf{p}_2]$, for a constant length d of segment $\mathbf{S}$ and for different depth coordinates of point $\mathbf{P}_1$, gives different solutions for point $\mathbf{P}_2$. Each of these segments has a different angulation. The result is that the angulation of segment $\mathbf{S}$ will be underestimated if

TAB. **6.2. Reconstructed catheter path and phantom average curve descriptors.**

Phantom	Projection model	κ	τ
A	FP	0.15	0.05
	WP	0.15	0.05
B	FP	0.27	0.05
	WP	0.28	0.04
A	phantom	0.15	0.06
B	phantom	0.26	0.06

FP : Full-perspective; WP : Weak-perspective; κ : Curvature coefficient (cm^{-1}); τ : Torsion coefficient (cm^{-1}).

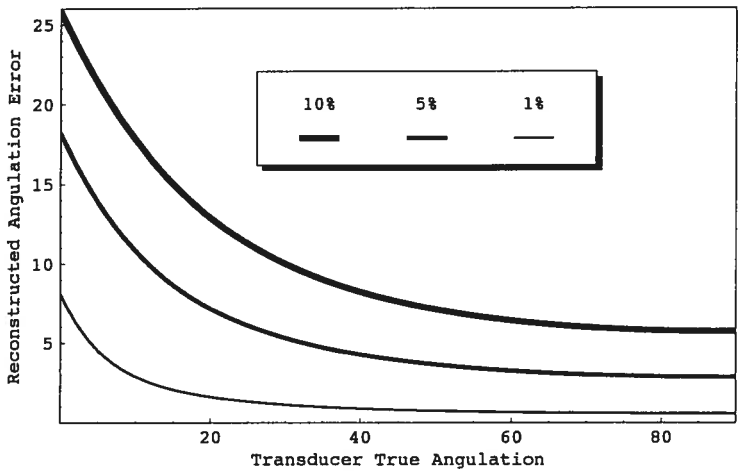

FIG. **6.7. Effect of the measured projected transducer length error on the reconstructed transducer angulation error at different angulation. The measured projected transducer length error is represented as a percentage in relation to the length of the transducer projection at 0°. Angles are represented in degrees.**

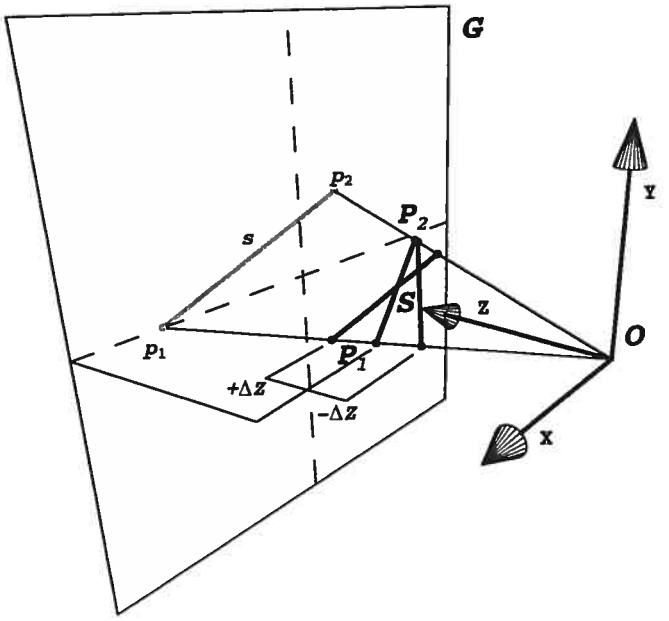

FIG. **6.8. Multiple solutions of back-projection in the full-perspective projection geometry. Back-projecting segment s by using different depth coordinates for point $\mathbf{P}_1$ gives solutions with different angulation.**

the depth location of point $\mathbf{P}_1$ is overestimated. By using typical values of 100 *cm* and 75 *cm*, for the localization of the projection plane and object plane respectively, a depth of view of 10 *cm* (the normal heart size), and a transducer length of 0.5 *cm*, it is possible to determine the worst case error in angulation estimation. An error of ± 5 *cm* in the estimated depth coordinate, with a transducer placed at 0° results in a variation of estimated angulation of $\pm 20^\circ$, decreasing rapidly to $\pm 3^\circ$ when the transducer is placed at 45°.

In the case of weak-perspective or orthographic projections (Fig. 6.9), the angulation of the 3D segments $\mathbf{S}$, found by back-projection of segment $\mathbf{s}$, is irrelevant to the initial 3D point depth estimation $\mathbf{P}_1$. This is an interesting aspect of the weak-perspective geometry, besides simplified calculations. In the worst case, comparing the full-perspective to the weak-perspective geometry, gives the same angular variation as when an initial 3D point location is misestimated, in full-perspective geometry

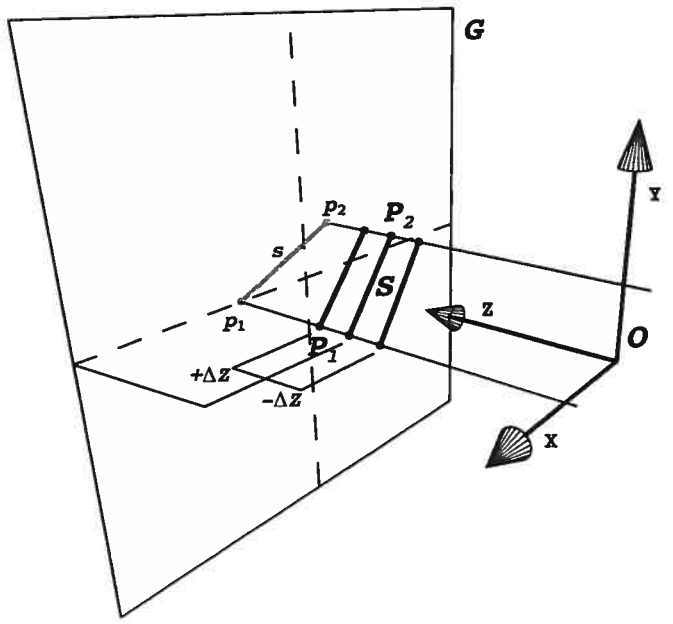

FIG. **6.9. Multiple solutions of back-projection in orthographic and weak-perspective projection geometries. The angulation of the multiple solutions of the back-projecting segment s is not dependent on the selected depth coordinate of point P_1.**

alone.

6.4.2 Experimental reconstruction

When comparing the catheter path reconstruction of each phantom, the best reconstruction was obtained for *phantom B*, independently of the projection geometry, with an absolute average euclidean distance errors less than half those of *phantom A*, Tab. 6.1. To take into account the phantom shapes, the average euclidean distance errors was expressed as the percentage of the phantom diameters. Even though phantom B still has a better path reconstruction, the reconstruction errors become comparable, being slightly less than 5% and 2% for weak and full perspective projection respectively.

Comparing the projection model used for the path reconstruction, on average

the full-perspective projection model presents an absolute average euclidean distance error of 0.17 *cm*, which is 2.4 times less compared to the weak-perspective projection. The difficulties encountered in path reconstruction using weak-perspective might come from the fact that the approximation error inherent to weak-perspective overwhelms its depth independent angulation reconstruction advantage, Sect. 6.4.1. In fact, the ratio of the average object depth to scene depth is approximately 1 :10, instead of the prescribed 1 :20, Sect. 6.2.1. A pullback done over a segment covering less depth might give better results with weak-perspective.

The differences in reconstruction error between each phantom might be explained by the fact that our reconstruction method depends on the pullback speed. Underestimating the pullback speed gives a compressed reconstruction along the Z-axis, and vice versa. Informal tests have shown that the catheter speed, assumed constant, could vary slightly with the pullback device used in this study.

Using curvature κ and torsion τ coefficients as curve descriptors, enables us to compare the fantoms values to in-vivo coronary curvatures values. They represent also a mean to validate the transducer reconstructed paths in relation to the phantom shapes. For the phantoms, κ and τ were calculated using Eq. 6.13, see Tab. 6.2. For the transducer reconstructed paths, the following formulation [39] were used :

$$\kappa = \frac{\|\vec{s}'(t) \times \vec{s}''(t)\|}{\|\vec{s}'(t)\|^3} \tag{6.14}$$

and

$$\tau = \frac{[\vec{s}'(t) \times \vec{s}''(t)] \cdot \vec{s}'''(t)}{\|\vec{s}'(t) \times \vec{s}''(t)\|^2}, \tag{6.15}$$

where $\vec{s}(t)$ is a cubic spline fitted on the reconstructed path and $'$, $''$ and $'''$ represent first, second and third order derivatives respectively. Table 6.2 presents the average curvature and torsion of 100 equidistant points along the fitted spline on the reconstructed path.

The curvature and torsion of the phantoms are within the lower range measured by Zhu *et al.* [94] along the right coronary artery. Zhu *et al.* curvature coefficients

vary from 0.05 to 1.2 compared to 0.15 and 0.26 for phantom A and B respectively. Zhu *et al.* torsion coefficient vary from 0 to 10 compared to 0.06 for both phantoms.

When using the curvature and torsion coefficients to compare the transducer reconstructed path in relation to the phantom shape, independently of the projection model we obtain good results.

With regard to the length of the moving average filter applied on the measured transducer length, as previously stated, the reconstruction results are not much affected by the filter length variations, although, a short filter will produce noisy reconstructions. On the other hand, too much filtering will flatten the reconstruction along the depth axis. The 21-images length filter was chosen for its intermediate value. Different lengths were tested, giving sub-millimeter variations in the average euclidean distances between the reconstructed path and the *helical mathematical models* with filter length variations of ± 10 images.

Another aspect of the reconstruction method is that any mirror reflection of the catheter path, parallel to the projection plane, will give the same projection. When reconstructing, a heuristic must be used in order to choose among the possible solutions. Since the phantoms were helical, the reconstructions were constrained to create curved-in shapes. Using our method *in vivo* would imply a similar heuristic since, depending on the projection angle, the heart shape can be simplified as an ellipsoid.

There is a need in clinical research and in the clinical setting for spatially correct three-dimensional IVUS images. Novel anti-atherosclerotic approaches are being assessed with IVUS as the primary efficacy assessment measure and reliable assessment of plaque volume changes is critical. Although spatially correct 3-D images have been generated using the fusion of IVUS and biplane angiography, the availability of biplane systems in modern cardiac catheterization laboratories is very limited. Obtaining spatially correct 3-D IVUS using the widely available single-projection angiographic systems is a presently unmet medical need [27].

In clinical environment, applying our reconstruction method requires no special manipulations other than those already performed during an IVUS examination, since the placement and pullback of the IVUS catheter is usually supervised by fluoroscopy.

As demonstrated by Waligora *et al.* [89], straight stacking reconstruction methods introduce substantial geometric error in vessels with small radii of curvature. Our method should do well in such condition since, as noted in the theoretical analysis, the error in reconstruction process does not depend on the vessel curvature but rather on the vessel relative angle in relation to the projection plane.

6.5 CONCLUSION

A method to recover the 3D trajectory of a catheter transducer, based on single-plane angiogram of helical phantoms using full and weak perspective projection models, was applied and assessed. The path curvature was in good part recovered, being on average less than 2 *mm* distant from the true path when using full-perspective projection. Expressed as the percentage of the phantom diameter, the reconstruction error is less than 2%. When comparing the projection geometry models, the full-perspective projection produces reconstruction errors that are less than 2.5 times than the weak-projection model.

ACKNOWLEDGMENTS

The authors thank the technicians, Colette Desjardins and Joanne Vincent, the engineer, Pierre Le Guyader, and Dr. Jacques Lesperance from the Montreal Heart Institute, for their help in the acquisition of the phantom images.

Chapitre 7

DISCUSSION ET CONCLUSION

La reconstruction 3D du réseau vasculaire est essentielle pour permettre au médecin d'établir un bon diagnostic. Appliqué à la coronarographie, l'apport d'une information 3D est aussi important d'un point de vue morphologique, que fonctionnel. Traditionnellement, la reconstruction 3D du réseau vasculaire se fait à l'aide d'appareils angiographiques biplans. Parce qu'ils demandent des manipulations complexes et considérant leur coût élevé, ces derniers sont de plus en plus remplacés par des appareils monoplans.

L'objectif visé par le présent travail de recherche est de pouvoir réaliser une reconstruction 3D à partir uniquement d'une seule vue. Le concept de base repose sur l'utilisation d'information *a priori* sur la structure à l'étude. Deux approches ont été développées : la reconstruction 3D du réseau vasculaire coronarien et la reconstruction 3D du chemin emprunté par la caméra IVUS lors d'examens endoscopiques.

La reconstruction 3D des artères coronaires à partir d'une seule vue est rendue possible grâce à l'utilisation d'un modèle coronarien. Le modèle provient de données biométriques fournies par Dodge *et al.*, auxquelles nous avons fait subir des transformations qui normalisent les variations intra et inter sujets composants le modèle. La reconstruction 3D de l'arbre coronarien fut réalisée à partir de l'ajustement entre la projection du modèle et les mesures au niveau des angiogrammes. Une fois, le modèle ajusté, il fut possible de suivre les contractions cardiaques des divers cas cliniques. Notre reconstruction a pu être validée par l'entremise d'une comparaison entre notre indice de contraction et la mesure standard de fraction d'éjection obtenue en ventriculographie (angiographie des ventricules) ou en échographie.

L'autre approche fut la reconstruction 3D du chemin emprunté par une caméra

IVUS lors d'examens endovasculaires. Pour comprendre l'utilité d'une telle reconstruction 3D, il faut se mettre dans un contexte de fusion des modes d'imagerie vasculaire qu'est l'imagerie ultrasonore endovasculaire et angiographique. En effet, l'apport de ces 2 modes est complémentaire : l'angiographie excelle au niveau de la résolution des images et donne une information précise au niveau de la morphologie et de la dynamique des artères coronaires. Par contre, les images angiographiques présentent des lacunes au niveau des mesures de volumes et de composition des vaisseaux, ce que viennent pallier les images ultrasonores. Les images IVUS n'apportent, quant à elles, aucune information sur la localisation spatiale globale, ce que permet l'angiographie. Faire une reconstruction 3D du chemin de la caméra IVUS permet d'orienter les images IVUS dans un espace global et ainsi obtenir des mesures plus précises.

Notre méthode de reconstruction 3D utilise la taille et la forme de la caméra IVUS. On compare cette information à la projection observée sur les angiogrammes, afin d'établir l'orientation de la caméra. Comme on utilise ici la cinéangiographie, une reconstruction complète du chemin de la caméra IVUS est possible en rattachant bout à bout les orientations de la caméra sur une séquence d'images. Nous avons validé cette méthode de reconstruction à l'aide de fantômes hélicoïdaux.

Bien qu'ayant donné des résultats satisfaisants, certains aspects du présent travail de recherche pourraient bénéficier de raffinements et d'améliorations. Par exemple, dans la partie de reconstruction 3D de l'arbre coronarien, nous n'avons considéré que des transformations rigides : rotation, translation, mise à l'échelle isotropique. Comme les coronaires et l'épicarde auquel elles se rattachent sont composés de tissus mous, des déformations non rigides pourraient être envisagées : torsions, mise à l'échelle anisotropique, etc. De plus, pour augmenter la robustesse et la précision de notre méthode, il serait aussi certainement souhaitable d'incorporer la coronaire droite (CD) dans notre méthodologie. Cela nécessitera cependant l'ajout d'une étape de recalage avec l'artère coronaire gauche et ses deux principales artères soient l'interventriculaire antérieure (IVA) et la circonflexe (Cx).

En ce qui concerne la reconstruction 3D du chemin de la caméra IVUS, la reconstruction du chemin repose en grande partie sur la vitesse du retrait de la caméra. Cette dernière est supposée constante, mais dans les faits des variations existent. Une méthode de reconstruction indépendante de la vitesse du retrait serait à approfondir.

La reconstruction 3D réalisée à partir d'une seule vue ne peut certainement pas surclasser, au niveau de la précision, les reconstructions réalisées à partir de 2 ou plusieurs vues, puisque le niveau d'information d'une seule image est moindre. Par contre, là où l'appareillage n'offre que l'option d'imagerie monoplan, le vaste domaine de la reconstruction 3D est maintenant ouvert.

RÉFÉRENCES

[1] J. K. Aggarwal, Q. Cai, W. Liao, et B. Sabata. Nonrigid motion analysis : Articulated and elastic motion. *Computer Vision and Image Understanding*, 70(2) :142–156, MAY 1998.

[2] K.S. Arun, T.S. Huang, et S.D. Blostein. Least-squares fitting of two 3-D point sets (computer vision). *IEEE Transactions on Pattern Analysis and Machine Intelligence*, PAMI-9 :698–700, 1987.

[3] R. Basri et D. Weinshall. Distance metric between 3D models and 2D images for recognition and classification. *IEEE Transactions on Pattern Analysis and Machine Intelligence*, 18 :465–79, 1996.

[4] P.J. Besl et H.D. McKay. A method for registration of 3-D shapes. *IEEE Transactions on Pattern Analysis and Machine Intelligence*, 14 :239–56, 1992.

[5] C. von Birgelen, E. A. de Vrey, G. S. Mintz, A. Nicosia, N. Bruining, W. Li, C. J. Slager, J. R. Roelandt, P. W. Serruys, et P. J. de Feyter. Ecg-gated three-dimensional intravascular ultrasound : feasibility and reproducibility of the automated analysis of coronary lumen and atherosclerotic plaque dimensions in humans. *Circulation*, 96(9) :2944–52, 1997.

[6] C. Blondel, R. Vaillant, F. Devernay, G. Malandais, et N. Ayache. Automatic trinocular 3D reconstruction of coronary artery centerlines from rotational X-ray angiography. Dans *Proceedings of 16th International Symposium on Computer Assisted Radiology and Surgery CARS 2002*, pages 832–837. Springer-Verlag, 2002.

[7] R. S. Burington. *Handbook of mathematical tables and formulas.* McGraw-hill Book Company, 1965.

[8] P.S. Calhoun, B.S. Kuszyk, D.G. Heath, J.C. Carley, et E.K. Fishman. Three-dimensional volume rendering of spiral ct data : theory and method. *Radiographics*, 19(3) :745–64, May-Jun 1999.

[9] C. Chalopin, G. Finet, et I. E. Magnin. Modeling the 3D coronary tree for labeling purposes. *Medical Image Analysis*, 5(4) :301–315, 2001.

[10] S. J. Chen et J. D. Carroll. 3-D reconstruction of coronary arterial tree to optimize angiographic visualization. *IEEE Trans Med Imaging*, 19(4) :318–36., 2000.

[11] S. Y. Chen, J. D. Carroll, et J. C. Messenger. Quantitative analysis of reconstructed 3-D coronary arterial tree and intracoronary devices. *IEEE Trans Med Imaging*, 21(7) :724–40., 2002.

[12] S.-Y.J. Chen et J.D. Carroll. Kinematic and deformation analysis of 4-D coronary arterial trees reconstructed from cine angiograms. *Medical Imaging, IEEE Transactions on*, 22(6) :710– 721, June 2003.

[13] S.Y. Chen et C.E. Metz. Improved determination of biplane imaging geometry from two projection images and its application to three-dimensional reconstruction of coronary arterial trees. *Med Phys*, 24(5) :633–54, 1997.

[14] F. Cheriet. Détermination de la contraction de la surface cardiaque en coronarographie biplan. Mémoire de maîtrise, Laboratoire de Vision et Modélisation Géométrique, Département d'Informatique et de recherche opérationnelle, Université de Montréal., 1996.

[15] R. M. Cothren, R. Shekhar, E. M. Tuzcu, S. E. Nissen, J. F. Cornhill, et D. G. Vince. Three-dimensional reconstruction of the coronary artery wall by image fusion of intravascular ultrasound and bi-plane angiography. *Int J Card Imaging*, 16(2) :69–85, 2000.

[16] J. T. Dodge, B. G. Brown, E. L. Bolson, et H. T. Dodge. Lumen diameter of

normal human coronary arteries. influence of age, sex, anatomic variation, and left ventricular hypertrophy or dilation. *Circulation*, 86(1) :232–46, 1992.

[17] J. T. Dodge Jr, B. G. Brown, E. L. Bolson, et H. T. Dodge. Intrathoracic spatial location of specified coronary segments on the normal human heart. applications in quantitative arteriography, assessment of regional risk and contraction, and anatomic display. *Circulation*, 78(5) :1167–80, 1988.

[18] J. Esthappan, M.A. Kupinski, Li Lan, et K.R. Hoffmann. A method for the determination of the 3D orientations and positions of catheters from single-plane X-ray images. Dans *Proceedings of the 22nd Annual International Conference of the IEEE Engineering in Medicine and Biology Society (Cat. No.00CH37143) p. 4 vol. xxiii+3272*, pages 2029–32. Proceedings of the 22nd Annual International Conference of the IEEE Engineering in Medicine and Biology Society, IEEE ; Piscataway, NJ, USA, 2000.

[19] J. L. Evans, K. H. Ng, S. G. Wiet, M. J. Vonesh, W. B. Burns, M. G. Radvany, B. J. Kane, C. J. Davidson, S. I. Roth, B. L. Kramer, S. N. Meyers, et D. D. McPherson. Accurate three-dimensional reconstruction of intravascular ultrasound data. spatially correct three-dimensional reconstructions. *Circulation*, 93(3) :567–76, 1996.

[20] T.L. Faber, E.M. Stokely, R.M. Peshock, et J.R. Corbett. A model-based four-dimensional left ventricular surface detector. *IEEE Transactions on Medical Imaging*, 10 :321–9, 1991.

[21] O. D. Faugeras. What can be seen in three dimensions with an uncalibrated stereo rig ? Dans *Computer Vision - ECCV '92. Second European Conference on Computer Vision Proceedings p. xv+909*, pages 563–78. Springer-Verlag ; Berlin, Germany, 1992.

[22] J. D. Foley, A. van Dam, S. K. Feiner, et J. F. Hughes. *Computer Graphics Principles and Practice.* Addison-Wesley, 1996.

[23] A. F. Frangi, W. J. Niessen, et M. A. Viergever. Three-dimensional modeling for functional analysis of cardiac images : a review. *IEEE Trans Med Imaging*, 20(1) :2–25, 2001.

[24] M. Garreau, J.L. Coatrieux, R. Collorec, et C. Chardenon. A knowledge-based approach for 3-D reconstruction and labeling of vascular networks from biplane angiographic projections. *IEEE Transactions on Medical Imaging*, 10 :122–31, 1991.

[25] G. Germano, J. Erel, H. Kiat, P. B. Kavanagh, et D. S. Berman. Quantitative lvef and qualitative regional function from gated thallium-201 perfusion spect. *J Nucl Med*, 38(5) :749–754, 1997.

[26] j. Gu, C. Toumoulin, et H. Chu. Spatio-temporal registration in coronary angiography. Dans *IEEE Engineering in Medicine and Biology Society 2003*, 2003.

[27] A. Guedes et J.C. Tardif. Intravascular ultrasound assessment of atherosclerosis. *Current Atherosclerosis Reports*, 66(3) :219–24, May 2004.

[28] Y. Hel-Or et M. Werman. Absolute orientation from uncertain point data : a unified approach. Dans *Proceedings. 1992 IEEE Computer Society Conference on Computer Vision and Pattern Recognition (Cat. No.92CH3168-2) p. xvi+870*, pages 77–82. IEEE Comput. Soc. Press ; Los Alamitos, CA, USA, 1992.

[29] K.R. Hoffmann, A. Sen, L. Lan, K.G. Chua, J. Esthappan, et M. Mazzucco. A system for determination of 3d vessel tree centerlines from biplane images. *International Journal of Cardiac Imaging*, 16(5) :315–30, 2000.

[30] B.K.P. Horn. Closed-form solution of absolute orientation using unit quaternions. *Journal of the Optical Society of America A*, 4 :629–42, 1987.

[31] B.K.P. Horn, H.M. Hilden, et S. Negahdaripour. Closed-form solution of absolute orientation using orthonormal matrices. *Journal of the Optical Society of America A*, 5 :1127–35, 1988.

[32] N.B. Ingels, Jr, G.T. Daughters, 2nd, E. B. Stinson, et E. L. Alderman. Evaluation of methods for quantitating left ventricular segmental wall motion in man using myocardial markers as a standard. *Circulation*, 61(5) :966–72, May 1980.

[33] JOMED. Site JOMED : Avanar F/X IVUS Catheter. http ://www.jomed.com/products/avanar/productinfo/avanar-us.html, 2003/07/01.

[34] K.R. Karsch, U. Lamm, H. Blanke, et K.P. Rentrop. Comparison of nineteen quantitative models for assessment of localized left ventricular wall motion abnormalities. *Clin Cardiol*, 3(2) :123–8, 1980.

[35] Y. Kong, J.J. Morris, Jr, et H. D. McIntosh. Assessment of regional myocardial performance from biplane coronary cineangiograms. *Am J Cardiol*, 27(5) :529–37, May 1971.

[36] M. Laban, J.A. Oomen, C.J. Slager, J.J. Wentzel, R. Krams, J.C.H. Schuurbiers, A. den Beer, C. von Birgelen, P.W. Serruys, et P.J. de Feijter. Angus : a new approach to three-dimensional reconstruction of coronary vessels by combined use of angiography and intravascular ultrasound. Dans *Computers in Cardiology 1995*, pages 325–8, 1995.

[37] A. K. Law, H. Zhu, et Chan F. H. Y. 3D reconstruction of coronary artery using biplane angiography. Dans *IEEE Engineering in Medicine and Biology Society 2003*, 2003.

[38] Université Leiden. Site Leiden University Medical Center, Départment de Radiologie, Division du Traitement d'Image, J. Dijkstra. http ://www.lumc.nl/1010/LKEBHome/english/research/IVUS/IVUS_STW/LKEB_IVUS_STW.html, 2003/12/30.

[39] R. Liao, S.-Y. J. Chen, J.C. Messenger, B. M. Groves, J.E.B. Burchenal, et J.D. Carroll. Four-dimensional analysis of cyclic changes in coronary artery shape. *Catheterization and Cardiovascular Interventions*, 55 :344–54, 2002.

[40] K.J. Liu, J.M. Rubin, M.J. Potel, A. Aisen, S.A. MacKay, R.E. Sayre, et C.E. Anagnostopoulos. Left ventricular wall motion : its dynamic transmural characteristics. *Journal of Surgical Research*, 36(1) :25–34, 1984.

[41] D.G. Lowe. Three-dimensional object recognition from single two-dimensional images. *Artificial Intelligence*, 31 :355–95, 1987.

[42] SA MacKay, MJ Potel, et JM Rubin. Graphics methods for tracking three-dimensional heart wall motion. *Computers & Biomedical Research*, 15(5) :455–73, 1982.

[43] J. Maehle, K. Bjoernstad, S. Aakhus, H.G. Torp, et B.A. Angelsen. Three-dimensional echocardiography for quantitative left ventricular wall motion analysis : a method for reconstruction of endocardial surface and evaluation of regional dysfunction. *Echocardiography*, 11(4) :397–408, 1994.

[44] R. Medina, M. Garreau, C. Navarro, J.L. Coatrieux, et D. Jugo. Reconstruction of three-dimensional cardiac shapes in biplane angiography : a fuzzy and evolutionary approach. Dans *Computers in Cardiology 1999. Vol.26 (Cat. No.99CH37004) p. xxiii+724*, volume 26, pages 663–6. Computers in Cardiology 1999. Vol. 26, IEEE ; Piscataway, NJ, USA, 1999.

[45] R. Medina, A. Wahle, M. E. Olszewski, et M. Sonka. Volumetric quantification of coronary arteries reconstructed by fusion between intravascular ultrasound and biplane angiography. *Biomedical Imaging, 2002. Proceedings. 2002 IEEE International Symposium on*, pages 891–894, 2002.

[46] G. D. Meier, M. C. Ziskin, W. P. Santamore, et A. A. Bove. Kinematics of the beating heart. *IEEE Trans Biomed Eng*, 27(6) :319–29, Jun 1980.

[47] J.C. Messenger, S.Y.J. Chen, J.D. Carroll, J.E.B. Burchenal, K. Kioussopoulos, et B.M. Groves. 3D coronary reconstruction from routine single-plane coronary angiograms : clinical validation and quantitative analysis of the right coronary

artery in 100 patients. *International Journal of Cardiac Imaging*, 16(6) :413–27, Dec. 2000.

[48] G. S. Mintz, J. J. Popma, A. D. Pichard, K. M. Kent, L. F. Satler, Y. C. Chuang, R. A. DeFalco, et M. B. Leon. Limitations of angiography in the assessment of plaque distribution in coronary artery disease : a systematic study of target lesion eccentricity in 1446 lesions. *Circulation*, 93(5) :924–31., 1996.

[49] C. C. Moore, C. H. Lugo-Olivieri, E. R. McVeigh, et E. A. Zerhouni. Three-dimensional systolic strain patterns in the normal human left ventricle : characterization with tagged mr imaging. *Radiology*, 214(2) :453–66, 2000.

[50] Victor Mor-Avi, Philippe Vignon, Rick Koch, Lynn Weinert, Maria J. Garcia, Kirk T. Spencer, et Roberto M. Lang. Segmental analysis of color kinesis images : New method for quantification of the magnitude and timing of endocardial motion during left ventricular systole and diastole. *Circulation*, 95(8) :2082–2097, 1997.

[51] F. H. Netter. *Heart : a compilation of paintings on the normal and pathologic anatomy and physiology, embryology, and diseases*, volume 5. The Ciba collection of medical illustrations, 1969.

[52] T.V. Nguyen et J. Sklansky. Reconstructing the 3-D medial axes of coronary arteries in single-view cineangiograms. *IEEE Transactions on Medical Imaging*, 13(1) :61–73, 1994.

[53] M.E. Olszewski, R.M. Long, S.C. Mitchell, A. Wahle, et M. Sonka. Quantitative measurements in geometrically correct representations of coronary vessels in 3-D and 4-D. Dans *Proceedings 4th IEEE Southwest Symposium on Image Analysis and Interpretation*, pages 259–63, 2000.

[54] ME Olszewski, RM Long, SC Mitchell, A Wahle, et M Sonka. A quantitative study of coronary vasculature in four dimensions. Dans *World Congress 2000*

- *22nd Annual International Conference of the IEEE Engineering in Medicine and Biology Society (EMBS)*, pages 2621–2624, 2000.

[55] M.J. Potel, S.A. MacKay, J.M. Rubin, A.M. Aisen, et R.E. Sayre. Three-dimensional left ventricular wall motion in man. coordinate systems for representing wall movement direction. *Investigative Radiology*, 19(6) :499–509, Nov-Dec 1984.

[56] M.J. Potel, J.M. Rubin, S.A. MacKay, A.M. Aisen, J. Al-Sadir, et R.E. Sayre. Methods for evaluating cardiac wall motion in three dimensions using bifurcation points of the coronary arterial tree. *Investigative Radiology*, 18(1) :47–57, Jan-Feb 1983.

[57] G. P. Prause, S. C. DeJong, C. R. McKay, et M. Sonka. Towards a geometrically correct 3-D reconstruction of tortuous coronary arteries based on biplane angiography and intravascular ultrasound. *Int J Card Imaging*, 13(6) :451–62, 1997.

[58] G.P.M. Prause, S.C. DeJong, C.R. McKay, et M. Sonka. Geometrically correct 3-D reconstruction of coronary wall and plaque : combining biplane angiography and intravascular ultrasound. Dans *Computers in Cardiology 1996*, pages 325–8, 1996.

[59] J. Puentes, C. Roux, M. Garreau, et J.L. Coatrieux. Dynamic feature extraction of coronary artery motion using dsa image sequences. *IEEE Transactions on Medical Imaging*, 17 :857–71, 1998.

[60] R.A. Robb, E.L. Ritman, et L.D. Harris. *Cardiac Imaging and Image Processing*, chapter 14 Digital image processing in x-ray computed tomography : high-speed volume imaging with the DSR., pages 361–406. McGraw-Hill Book Co., New York, 1986.

[61] J. R. Roelandt, C. di Mario, N. G. Pandian, L. Wenguang, D. Keane, C. J. Slager, P. J. de Feyter, et P. W. Serruys. Three-dimensional reconstruction of in-

tracoronary ultrasound images. rationale, approaches, problems, and directions. *Circulation*, 90(2) :1044–55, 1994.

[62] K Rosenfield, DW Losordo, K Ramaswamy, JO Pastore, RE Langevin, S Razvi, BD Kosowsky, et JM Isner. Three-dimensional reconstruction of human coronary and peripheral arteries from images recorded during two-dimensional intravascular ultrasound examination. *Circulation*, 84(5) :1938–1956, 1991.

[63] T. Saito, M. Misaki, K. Shirato, et T. Takishima. Three-dimensional quantitative coronary angiography. *IEEE Transactions on Biomedical Engineering*, 37(8) :768–77, 1990.

[64] A. Sarwal et A. P. Dhawan. Three dimensional reconstruction of coronary arteries from two views. *Comput Methods Programs Biomed*, 65(1) :25–43, 2001.

[65] I. Schnittger, P.J. Fitzgerald, E.P. Gordon, E.L. Alderman, et R.L. Popp. Computerized quantitative analysis of left ventricular wall motion by two-dimensional echocardiography. *Circulation*, 70(2) :242–254, 1984.

[66] G. Shechter, F. Devernay, E. Coste-Maniere, A. Quyyumi, et E.R. McVeigh. Three-dimensional motion tracking of coronary arteries in biplane cineangiograms. *Medical Imaging, IEEE Transactions on*, 22(4) :493– 503, April 2003.

[67] R. Shekhar, R.M. Cothren, D.G. Vince, et J.F. Cornhill. Fusion of intravascular ultrasound and biplane angiography for three-dimensional reconstruction of coronary arteries. Dans *Computers in Cardiology 1996*, pages 5–8, 1996.

[68] R. Shekhar, R.M. Cothren, D.G. Vince, et J.F. Cornhill. Spatio-temporal localization of intravascular ultrasound data for accurate 3D reconstruction of coronary arteries. Dans *Proceedings of 18th Annual International Conference of the IEEE Engineering in Medicine and Biology Society*, vol.2, pages 668–9, 1997.

[69] D. Sherknies et J. Meunier. A numerical 3D coronary tree model. Dans *Proceedings of 16th International Symposium on Computer Assisted Radiology and Surgery CARS 2002*, pages 814–818. Springer-Verlag, 2002.

[70] D. Sherknies, J. Meunier, R. Mongrain, et J. C. Tardif. 3D trajectory assessment of an IVUS transducer from single-plane cineangiograms : a phantom study. Dans *Proceedings of the 25th Annual International Conference of the IEEE Engineering in Medicine and Biology Society*, volume 1, pages 690–693. IEEE ; Piscataway, NJ, USA, 2003.

[71] D. Sherknies, J. Meunier, et J. C. Tardif. 3D path recovery of an IVUS transducer with single-plane angiography. Dans *IEEE Canadian Conference On Electrical And Computer Engineering, CCECE 2003*, volume 3, pages 1489–1492, May 2003.

[72] D. Sherknies, J. Meunier, et J. C. Tardif. 3D heart motion from single-plane angiography of the coronary vasculature : a model-based approach. Dans *Proceedings of the SPIE - The International Society for Optical Engineering, Medical Imaging 2004 : Image Processing*, volume 5370, pages 381-389. SPIE Press, Mai. 2004.

[73] Siemens Axiom Artis. Site Siemens Clinical Solution : Axiom Artis. http ://www.medical.siemens.com/webapp/wcs/stores/servlet/ CategoryDisplay, 2003/06/06.

[74] D.J. Skorton, S.M. Collins, E. Garcia, E.A. Geiser, W. Hillard, W. Koppes, D. Linker, et G. Schwartz. Digital signal and image processing in echocardiography. the american society of echocardiography. *Am Heart J*, 110(6) :1266–83, 1985.

[75] C. J. Slager, J. J. Wentzel, J. A. Oomen, J. C. Schuurbiers, R. Krams, C. von Birgelen, A. Tjon, P. W. Serruys, et P. J. de Feyter. True reconstruction of vessel geometry from combined x-ray angiographic and intracoronary ultrasound data. *Semin Interv Cardiol*, 2(1) :43–7, 1997.

[76] C. J. Slager, J. J. Wentzel, J. C. Schuurbiers, J. A. Oomen, J. Kloet, R. Krams, C. von Birgelen, W. J. van der Giessen, P. W. Serruys, et P. J. de Feyter. True 3-

dimensional reconstruction of coronary arteries in patients by fusion of angiography and ivus (angus) and its quantitative validation. *Circulation*, 102(5) :511–6, 2000.

[77] M. Tafforeau. Site de Michel Tafforeau. http ://users.skynet.be/taf/Tabac/fumee/coeur/coronaro.html, 2003/12/30.

[78] T.S.Y. Tang, R.E. Ellis, et G. Fichtinger. Fiducial registration from a single x-ray image : a new technique for fluoroscopic guidance and radiotherapy. Dans *Medical Image Computing and Computer-Assisted Intervention - MICCAI 2000. Third International Conference. Proceedings (Lecture Notes in Computer Science Vol.1935) p. xxv+1244*, volume 1935, pages xxv+1244,. Medical Image Computing and Computer-Assisted Intervention - MICCAI 2000. Third International Conference. Proceedings, Springer-Verlag ; Berlin, Germany, 2000.

[79] E. Trucco et A. Verri. *Introductory Techniques for 3-D Computer Vision.* Prentice Hall, 1998.

[80] M. Verreault. Analyse de la dynamique épicardique en coronarographie monoplan. Mémoire de maîtrise, Département de Génie Biomédical, Ecole Polytechnique, Université de Montréal, 1994.

[81] A. Wahle, S. C. Mitchell, S. D. Ramaswamy, K. B. Chandran, et M. Sonka. Four-dimensional coronary morphology and computational hemodynamics. Dans M. Sonka et K. M. Hanson, editeurs, *Medical Imaging 2001 : Image Processing*, volume 4322, pages 743–754, Bellingham WA, 2001. SPIE Proceedings.

[82] A. Wahle, S. C. Mitchell, S. D. Ramaswamy, K. B. Chandran, et M. Sonka. Virtual angioscopy in human coronary arteries with visualization of computational hemodynamics. Dans C. Chen et A. V. Clough, editeurs, *Medical Imaging 2001 : Physiology and Function from Multidimensional Images*, volume 4321, pages 32–43, Bellingham WA, 2001. SPIE Proceedings.

[83] A. Wahle, G. P. M. Prause, S. C. DeJong, et M. Sonka. Geometrically correct

3-D reconstruction of intravascular ultrasound images by fusion with biplane angiography–methods and validation. *IEEE Trans Med Imaging*, 18(8) :686–99, 1999.

[84] A. Wahle, G.P.M. Prause, S.C. DeJong, et M. Sonka. 3-D fusion of biplane angiography and intravascular ultrasound for accurate visualization and volumetry. Dans *Medical Image Computing and Computer-Assisted Intervention - MICCAI'98. First International Conference. Proceedings*, pages 146–55, 1998.

[85] A. Wahle, G.P.M. Prause, S.C. DeJong, et M. Sonka. Determination of the absolute axial orientation of intracoronary ultrasound images in fusion with biplane angiography. Dans *Computers in Cardiology 1998. Vol. 25*, pages 153–6, 1998.

[86] A. Wahle, G.P.M. Prause, S.C. DeJong, et M. Sonka. A comprehensive method for geometrically correct 3-D reconstruction of coronary arteries by fusion of intravascular ultrasound and biplane angiography. Dans *Proceedings of the First International Workshop on Computer Aided Diagnosis in Medical Imaging*, pages 363–8, 1999.

[87] A Wahle, E. Wellnhofer, et I. Mugaragu. Quantitative analysis of coronary morphology based upon 3-D reconstruction from biplane angiograms. *IEEE Trans Med Imaging*, 1995.

[88] A. Wahle, S. C. Mitchell, M. E. Olszewski, R. M. Long, et M. Sonka. Accurate visualization and quantification of coronary vasculature by 3D/4D fusion from biplane angiography and intravascular ultrasound. *SPIE Proceedings*, 4158 :144–155, 2001.

[89] M. J. Waligora, M. J. Vonesh, S. P. Wiet, et D. D McPherson. Effect of vascular curvatures on three-dimensional reconstruction of intravascular ultrasound images. *Circulation*, 90(suppl I) :I–227, 1994.

[90] P. Windyga, M. Garreau, M. Shah, H. Le Breton, et J.L. Coatrieux. Three-

dimensional reconstruction of the coronary arteries using a priori knowledge. *Medical & Biological Engineering & Computing*, 36 :158–64, 1998.

[91] S. Young, B. Movassaghi, J. Weese, et V. Rasche. 3D vessel axis extraction using 2D calibrated x-ray projections for coronary modeling. Dans J. Michael Fitzpatrick Milan Sonka, editeur, *The International Society for Optical Engineering*, pages 1491–1498. The International Society for Optical Engineering, May 2003.

[92] E.A. Zerhouni, D.M. Parish, W.J. Rogers, A. Yang, et E.P. Shapiro. Human heart : tagging with MR imaging–a method for noninvasive assessment of myocardial motion. *Radiology*, 169(1) :59–63, 1988.

[93] X. Zhang, C. R. McKay, et M. Sonka. Tissue characterization in intravascular ultrasound images. *Medical Imaging, IEEE Transactions on*, 17(6) :889–899, 1998.

[94] H. Zhu et M.H. Friedman. Relationship between the dynamic geometry and wall thickness of a human coronary artery. *Arterioscler Thromb Vasc Biol*, 23(12) :2260–5, Dec 2003.

ANNEXES

Les documents en annexe sont les articles et *poster* publiés au cours de ce travail de recherche et présentés en format original.

Annexe A

A NUMERICAL 3D CORONARY TREE MODEL

Référence [69] : D. Sherknies et J. Meunier. A numerical 3D coronary tree model. Dans *Proceedings of 16th International Symposium on Computer Assisted Radiology and Surgery CARS 2002*, pages 814–818. Springer-Verlag, 2002.

CARS 2002 – H.U. Lemke, M.W. Vannier; K. Inamura, A.G. Farman, K. Doi & J.H.C. Reiber (Editors)

A numerical 3D coronary tree model

Denis Sherknies[a], Jean Meunier[b]
[a]University of Montreal, [redacted]
[b]University of Montreal

Abstract

We present a method that defines a numerical 3D model of the main coronary arteries of the human heart at end-diastole. The data used in this article are a subset of the data used in two articles by Dodge et al. [1, 2]. 26 subjects with normal hearts, having measures for the 3 main arteries (right coronary artery, left anterior descending artery and left circumflex artery), were chosen. The method used to obtain the heart model can be summarized as follows: A well-formed subject is chosen as the reference. Subsequently, each of the other subjects is fitted to the reference with affine transformations (translation, rotation and scaling). The model is obtained by applying the mean of the inverse affine transformations back on the reference coronary tree. This model is the first step for the 3D construction of an atlas of the structure and motion of coronary arteries for cardiac contraction analysis.

Keyword: 3D, coronary, model

1. Introduction

When confronted with the task of recovering 3D information of the coronary arteries from angiographic images, one can use multiple views [3, 4], but due to the structure of the coronary tree, there exist a large number of possible ambiguities. The use of a priori knowledge in the form of a qualitative model [5], quantitative model [6], or a combination of both [7], helps alleviate these ambiguities. The use of a model can also help in the reconstruction of coronary arteries from a single view cineangiogram [8, 7]. Qualitative models can contain information in the form of a graph structure used for labeling purposes, quantitative models can be expressed with global shape descriptors as in a parametrically deformable model [9] or with more local attributes, like the location and variation of branching points [1]. It is an accepted fact that the location of the coronary arteries is variable, nonetheless certain constancy exists. And even if numerical models do not capture all the subtleties of the coronary tree, they offer certain advantages over the qualitative models, if only for anatomical visualization purposes.

In 1988 Dodge et al. published an article in which they describe the 3D location of branching points, among others, of the coronary tree [1]. An article published in 1992, added information about the lumen diameter at the different reference points [2].

Dodge's articles are often cited in the literature (32, 54 respectively [10]) and a phantom called *Coronix* [11], used in various simulation studies, has also been constructed based on Dodge's data.

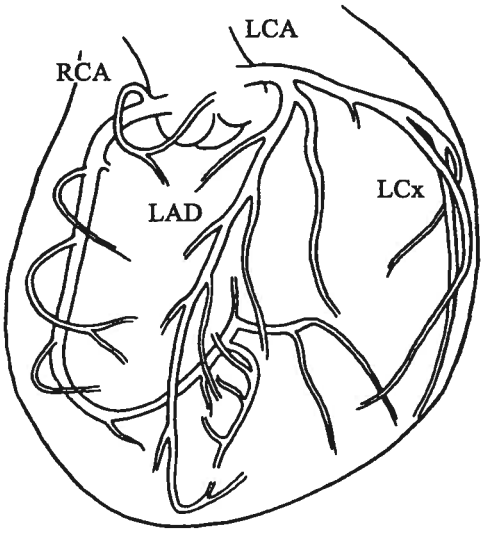

Figure 1. Right coronary artery dominance anatomy. RCA: Right coronary artery; LCA: Left coronary artery; LAD: Left anterior descending; LCx: Left circonflex. *From Dodge [1]*

Starting with Dodge's data we made some transformations in order to obtain a model less dependent on certain parameters like the absolute position of the coronary tree or the relative heart size. We are interested in the spatial location of reference points along the coronary tree in order to construct a model that will be used for tracking the motion of coronary arteries.

2. Data

The coronary tree present itself as a hierarchical structure divided in 3 main sections according to the heart region irrigated. We use here a nomenclature devised by Dodge et al. [1], see Figure 1. The left coronary artery (LCA) starts at the left of the aorta as the left main artery (LM) and divides itself into the left anterior descending artery (LAD) and the left circumflex artery (LCx). The right coronary artery (RCA) starts at the right of the aorta and irrigates the right side of the heart. Each of these main arteries divides themselves into smaller ramifications. The artery that irrigates the heart's anterior wall is said to define the dominance anatomy. There are three dominance anatomies: the right dominance, left dominance and the balanced anatomy.

The original data comes from the 3D location of 102 points along the coronary tree of 37 normal subjects. The measurements were taken at the end diastole by a biplane angiographic apparatus and were corrected for optical magnification and X-ray beam divergence, see Dodge's et al. articles for more details [1, 2].

For the elaboration of our model, a subset of the original data was selected, based on certain criteria. We kept only the subjects where the three main arteries were present. Also, the reference points from secondary branches and those having sporadic presence were dropped. We ended up with 26 subjects having a coronary tree composed of 36 reference points. See Table 1 for the demographic description of the subjects.

Age	Gender		Coronary dominance		
	M	F	Left	Balanced	Right
26 to 77 (mean, 48)	23	3	2	22	2

Table 1. Demographic summary

3. Methodology

In order to construct a *coronary tree model* that is immune to certain influences, we allow some transformations of the selected subset data. For example, scaling attenuates the inter-subject variation of the overall size of the coronary tree, translation and rotation

bring the coronary tree in a reference space that is less dependent on the relative position between the body and the measuring apparatus.

In a way similar to Guimond et al. [12], the method used for obtaining the heart model can be summarized as follow:

- First, a well-formed subject is chosen as a reference, the *reference subject*;
- Subsequently, the reference subject is fitted to each of the other subjects with affine transformations (translation, rotation and scaling);
- An average of the affine transformations is then computed;
- Finally, the *coronary tree model* is obtained by applying the average transformation on the *reference subject*.

The choice of the well-formed subject is based ... on its well-form! Without large variations to what could be described as an ideal normal subject.

Next, to find the affine transformations we consider this problem as a classic computer vision problem known, among various aliases, as *model-based object location*. It can be stated as follow: knowing the correspondence between two 3D points sets and their locations, find the best geometric transformation that minimize a cost function with respect to certain constraints. Different analytical and numerical techniques exist that solve such problems. Closed form solutions solved by singular value decomposition [13] or represented by orthonormal matrices [14] or unit quaternions [15] exist and they all give similar results [16].

The problem can be formulated as follows: given the relation between two point sets $\{m_i\}$ and $\{d_i\}$, $i = 1..N$ as $d_i = s\mathbf{R}m_i + \mathbf{T} + \mathbf{V}_i$ where s is a scaling factor, $\mathbf{R}$ is a 3×3 rotation matrix, $\mathbf{T}$ is a translation vector and $\mathbf{V}_i$ is a noise vector. We want to find $\hat{s}$, $\hat{\mathbf{R}}$ and $\hat{\mathbf{T}}$ that minimize the sum of the Euclidean distances between corresponding points $\sum_{i=1}^{N} \left\| d_i - \left(\hat{s}\hat{\mathbf{R}}m_i + \hat{\mathbf{T}}\right)\right\|^2$. We solve the scaling factor using Horn method [15] and the translation and rotation using the Arun method [13]. The three transformation components can be solved independently. By expressing the points sets by their respective centroids $\overline{m} = 1/N \sum_{i=1}^{N} m_i$ and $\overline{d} = 1/N \sum_{i=1}^{N} d_i$ as $m_i' = m_i - \overline{m}$ and $d_i' = d_i - \overline{d}$, the translation component is simplified and we are left with the scaling and rotation components only. The scaling is independent from the rotation and can be defined as $\hat{s} = \sqrt{\sum_{i=1}^{N} \left\|d_i'\right\|^2 / \sum_{i=1}^{N} \left\|m_i'\right\|^2}$. The solution to the rotation matrix is $\hat{\mathbf{R}} = \mathbf{V}\mathbf{U}^t$ where the singular value decomposition of the correlation matrix $\mathbf{H} = \sum_{i=1}^{N} m_i' d_i'^t$ is $\mathbf{H} = \mathbf{U}\mathbf{L}\mathbf{V}^t$. The translation component can then be found by using the rotation matrix on the centroids $\hat{\mathbf{T}} = \overline{d} - \hat{\mathbf{R}}\overline{m}$.

As previously stated, the *coronary tree model* results from the application of the average transformations on the *reference subject*.

4. Results

After applying the outlined method on the 26 coronary trees, we obtain the *coronary tree model*, see Figure 2. The average coefficients of transformation found after fitting the *reference subject* to the other subjects are:

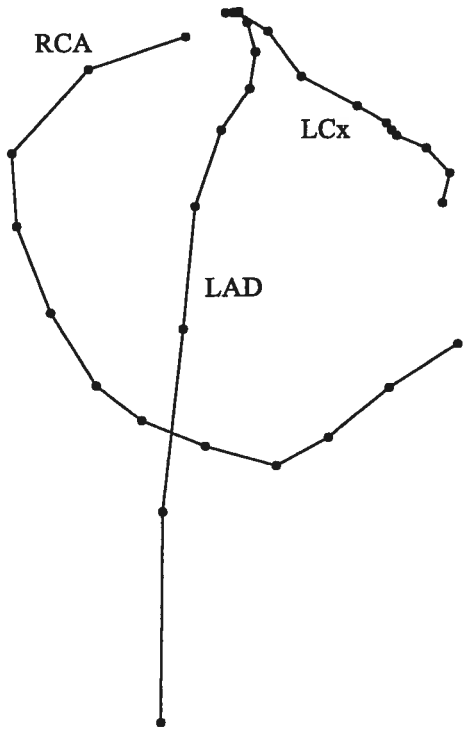

Figure 2. Wire-frame of the *coronary tree model* with an angle of view similar to Figure 1. *See Figure 1 for definitions.*

- for the scaling factor, s = 1.08;
- for the rotation expressed as the angles of rotation about the x, y, and z axes respectively, α = -0.04, β = 0.09, γ = -0.31 and
- for the translation component, $\mathbf{T}_x$ = 0.59, $\mathbf{T}_y$ = 0.18 and $\mathbf{T}_z$ = -0.04, corresponding to the translation on the specific axes.

The average distance between the matching points of the *coronary tree model* and the other subjects is 0.84 cm (0.15 SD). This average distance was 1.42 cm (0.45 SD) before applying the mean transformation.

5. Conclusions

We have presented a method that composes a model of the main coronary arteries of the human heart based on 3D reconstructions of 26 normal hearts. Although the reference system used by Dodge et al. was adequate for their study, the proposed method focuses on the morphological variations and considerably reduces the variability observed by their group by eliminating heart size, orientation and position variations. This model is the first step for a more general 3D atlas of the structure and motion of coronary arteries that will help cardiac contraction analysis and understanding.

Acknowledgements

The authors express their gratitude to Dr J. Theodore Dodge Jr. for having so generously shared his data.

References

1. Dodge JT, Brown BG, Bolson EL, Dodge HT: "Intrathoracic spatial location of specified coronary segments on the normal human heart." *Circulation* 78: 1167-1180, 1988.
2. Dodge JT, Brown BG, Bolson EL, Dodge HT: "Lumen diameter of normal human coronary arteries: influence of age, gender, anatomic variation and left ventricular hypertrophy or dilation." *Circulation* 86: 232-246, 1992.
3. MacKay, SA and Potel, MJ and Rubin, JM. "Graphics methods for tracking three-dimensional heart wall motion." *Computers & Biomedical Research*, 15(5), pp. 455-73, Oct 1982.
4. Saito T. and Misaki M. and Shirato K. and Takishima T. "Three-dimensional quantitative coronary angiography." *IEEE Transactions on Biomedical Engineering*, 37(8), pp. 768-77, Aug 1990.
5. P. Windyga, M. Garreau, M. Shah, H. Le Breton, and J.L. Coatrieux. "Three-dimensional reconstruction of the coronary arteries using a priori knowledge." *Medical & Biological & Computing*, 36:158–64, 1998.
6. Sarwal, A. and Dhawan, A. P. "Three dimensional reconstruction of coronary arteries from two views." *Comput Methods Programs Biomed*, 65(1), pp. 25-43, Apr 2001.
7. Chalopin, C. and Finet, G. and Magnin, I. E.. "Modeling the 3D coronary tree for labeling purposes." *Medical image analysis*, 5(4), pp. 301-315, Dec 2001.
8. Nguyen, T.V. and Sklansky, J. "Reconstructing the 3-D medial axes of coronary arteries in single-view cineangiograms." *IEEE Transactions on Medical Imaging*, 13, pp. 61-73, 1994.
9. Sarry, L. and Boire, J.-Y. "Three-dimensional tracking of coronary arteries from biplane angiographic sequences using parametrically deformable models. " *IEEE Transactions on Medical Imaging*, 20, pp. 1341-51, 2001.
10. ISI Web of Knowledge. http://woscanada.isihost.com/. 2002
11. Renaudin CP, Barbier B, Roriz R, Revel D, and Amiel M. "Coronary arteries : new design for three-dimensional arterial phantoms." *Radiology*, 190(2) :579–82, February 1994.
12. Guimond, A., Meunier, J. and Thirion, J.-P. "Average brain models : a convergence study." *Computer Vision and Image Understanding* (77) : 192-210. 2000.
13. Arun, K.S. and Huang, T.S. and Blostein, S.D. "Least-squares fitting of two 3-D point sets." *IEEE Transactions on Pattern Analysis and Machine Intelligence*, PAMI-9, pp. 698-700, 1987
14. Horn B.K.P., H.M. Hilden, and S. Negahdaripour. "Closed-form solution of absolute orientation using orthonormal matrices." *Journal of the Optical Society of America* A, 5 :1127-35, 1988.
15. Horn, B.K.P. "Closed-form solution of absolute orientation unit quaternions." *Journal of the Optical Society of A*, 4 :629–42, 1987.
16. Eggert, D.W. and Lorusso, A. and Fisher, R.B. "Estimating 3-D rigid body transformations: a comparison of four major algorithms." *Machine Vision and Applications*, 9, pp. 272-90, 1997.

Annexe B

3D PATH RECOVERY OF AN IVUS TRANSDUCER WITH SINGLE-PLANE ANGIOGRAPHY

Référence [71] : D. Sherknies, J. Meunier, et J. C. Tardif. 3D path recovery of an ivus transducer with single-plane angiography. Dans *IEEE Canadian Conference On Electrical And Computer Engineering, CCECE 2003*, volume 3, pages 1489–1492, Mai 2003.

3D PATH RECOVERY OF AN IVUS TRANSDUCER WITH SINGLE-PLANE ANGIOGRAPHY

Denis Sherknies
Université de Montréal
[redacted]

Jean Meunier
Université de Montréal
[redacted]

Jean-Claude Tardif
Montreal Heart Institute
[redacted]

Abstract

The recovery of the 3D path of the transducer used during an IntraVascular UltraSound (IVUS) examination is of primary importance to assess the exact 3D shape of the vessel under study. Traditionally, the reconstruction is done using biplane angiography. In this paper we explain, with three projection models, how single-plane angiography can be used to perform this task.

Three types of projection geometry are analyzed: orthographic, weak perspective and full perspective. In orthographic and weak perspective projection geometries, the catheter path can be reconstructed without prior transducer depth informations. With full perspective projection geometry, precise depth location of reference points are needed in order to minimize the error of the recovered transducer's angle of incidence.

We present the mathematical foundation and some simulations of the catheter path reconstruction. While reconstructing the 3D catheter path from a single-view projection is shown to be feasible, some heuristics are needed in order to obtain a path simulating the curvature of the heart pericardium vessels.

Keywords: *IVUS, Angiography, 3D-Reconstruction.*

1. INTRODUCTION

In recent years, the combination of two well-known medical image modalities, X-ray angiography and intravascular ultrasound (IVUS), has given spectacular results. This is mainly due to the fact that the two imaging techniques complement themselves well: IVUS gives accurate information on the vessels cross-section and angiography provides a mean to reconstruct the vessels 3D curvature.

The 3D reconstruction of the IVUS images gives a more accurate assessment of the vessel lumen and plaque morphology. The first 3D reconstructions were done by straight stacking the images one on top of the other [1]. This method creates incorrect volumetric representation because the images are not parallel from one another but they are rather perpendicular to the catheter centerline, which follows the curvature of the vessels.. The use of biplane angiography enables more precise IVUS image orientations and 3D localization [2], [3], [4], but these apparatus are complicated to operate and are not always available in many clinical centers.

In this paper, we present a method for recovering the IVUS transducer orientation from a single-plane projection (monocular vision), thus permitting to reconstruct the catheter path curvature. The whole process of the incidence angle recovery is based on the foreshortening effect of the IVUS transducer as seen on the angiogram. By comparing the known length of the transducer with the measured length of its projection, it is possible to obtain the incidence angle of the transducer. By combining a sequence of images, we can reconstruct the 3D catheter (transducer) path.

2. PROJECTION MODELS

We analyze the recovery of the IVUS transducer from a full perspective projection, an orthographic projection and a weak perspective projection. The conventions used in this article are as follows (see figure 1): the origin of the coordinate system axes is placed at the X-ray emission source of the imaging system; the axes are oriented so that the projection plane is perpendicular centered along the z axis; the projection plane is coincident with the angiogram; the segment $S = [\mathbf{P_1}, \mathbf{P_2}]$ represents the transducer location during a pull-back and the segment $s = [\mathbf{p_1}, \mathbf{p_2}]$ is the projection of the transducer on the angiogram. The angulation of the transducer is define in relation to the projection plane, a transducer parallel to the projection plane is said to be at $0\,^\circ$, and at $90\,^\circ$ when perpendicular to the projection plane.

2.1 Full perspective projection

If we define $\mathbf{P}_i = [X_i, Y_i, Z_i]$ as a 3D point and $\mathbf{p}_i = [u_i, v_i]$ a 2D point, the relation between $\mathbf{P}_i$ and its projection $\mathbf{p}_i$, for a pin-hole camera model, is given by

$$u_i = f\frac{X_i}{Z_i} \quad \text{and} \quad v_i = f\frac{Y_i}{Z_i} \tag{1}$$

where f is the focal distance. We assume here that the camera is placed at the origin in the 3D space, that the projection plane is perpendicular to the z_i axis and centered on it

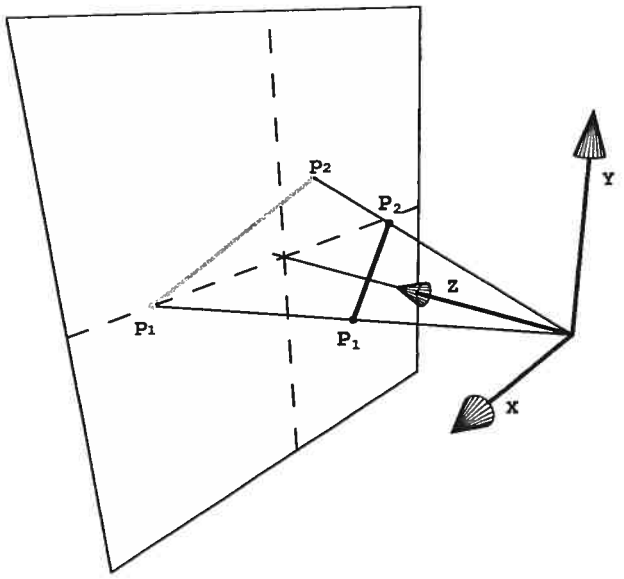

Figure 1. Full perspective projection geometry.

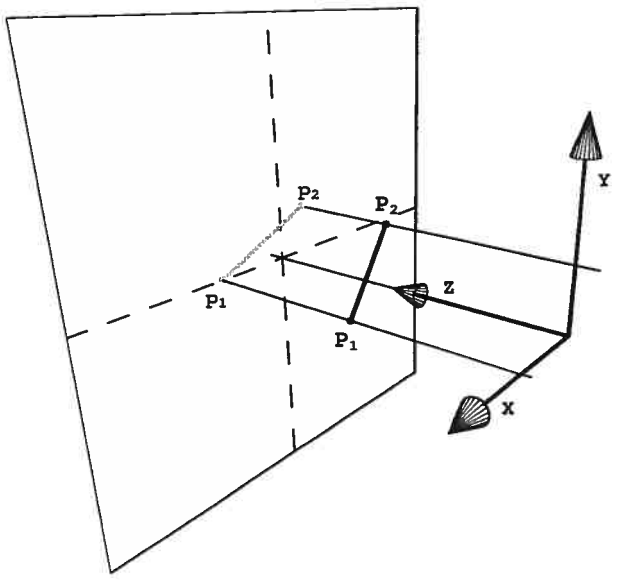

Figure 2. Orthographic projection geometry.

(see figure 1). The Euclidean distance between two points $\mathbf{P}_1 = [X_1, Y_1, Z_1]$ and $\mathbf{P}_2 = [X_2, Y_2, Z_2]$ can be found with

$$d = \sqrt{(X_2 - X_1)^2 + (Y_2 - Y_1)^2 + (Z_2 - Z_1)^2}. \quad (2)$$

Expressing equation 1a as a function of Z_2, we obtain

$$Z_2 = f\frac{X_2}{u_2}, \quad (3)$$

using equation 3 to substitute Z_2 in equation 1b and expressing it as Y_2 gives

$$Y_2 = v_2\frac{X_2}{u_2}. \quad (4)$$

Substituting equations 3 and 4 in 2 gives

$$d = \sqrt{(X_2 - X_1)^2 + (v_2\frac{X_2}{u_2} - Y_1)^2 + (f\frac{X_2}{u_2} - Z_1)^2}, \quad (5)$$

which solved for X_2 gives

$$X_2 = \frac{u_2 a \pm \sqrt{u_2^2\,[a^2 + b(d^2 - X_1^2 - Y_1^2 - Z_1^2)]}}{b}, \quad (6)$$

where $a = u_2X_1 + v_2Y_1 + fZ_1$ and $b = f^2 + u_2^2 + v_2^2$.

By substituting equation 6 in equations 3 and 4 we are able to find the 3D coordinates of $\mathbf{P}_2$ knowing the location of two projected points $\mathbf{p}_1, \mathbf{p}_2$, the location of a 3D point $\mathbf{P}_1$ and the distance between two 3D points d.

2.2 Orthographic projection

In an orthographic projection, the relation between a 3D point $\mathbf{P}_i = [X_i, Y_i, Z_i]$ and its projection $\mathbf{p}_i = [u_i, v_i]$, is given by

$$u_i = X_i \quad \text{and} \quad v_i = Y_i. \quad (7)$$

As in the case of full perspective projection, we assume that the projection plane is perpendicular to the z_i axis and centered on it (see figure 2). By using the equivalences found in equations 7, we are able to rewrite equation 2 as

$$Z_2 = Z_1 \pm \sqrt{d^2 - [(u_2 - u_1)^2 + (v_2 - v_1)^2]}, \quad (8)$$

which gives the depth coordinate of point $\mathbf{P}_2$.

2.3 Weak perspective projection

A weak perspective projection is realized by having an orthogonal projection followed by an isotropic scaling factor [5]. The scaling factor is in fact, the ratio of the focal distance on the average depth of the scene, defined by $f' = \frac{f}{\overline{Z}}$, where $\overline{Z} = \frac{1}{n}\sum_{i=1}^{n} Z_i$. The relation between the 3D points and their projections are $u_i = f'X_i$ and $v_i = f'Y_i$. Equation 8 can thus be rewritten as

$$Z_2 = Z_1 \pm \sqrt{d^2 - \frac{[(u_2 - u_1)^2 + (v_2 - v_1)^2]}{f'^2}}. \quad (9)$$

3. 3D Path Reconstruction Method

The steps involved in our method of 3D path transducer recovery are as follows. First, in order to simulate a projection, we created a 3D path, the 3D spiral in figure 3, which

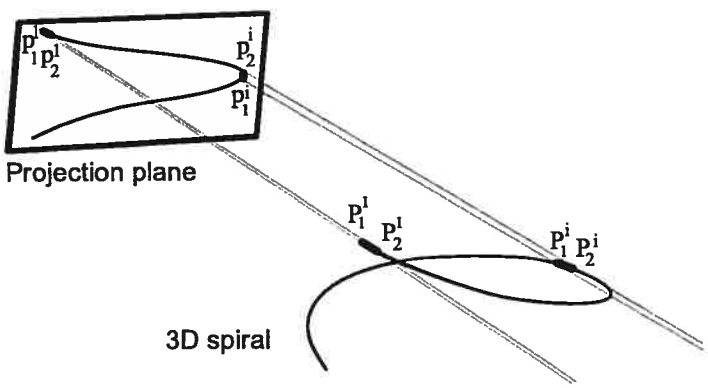

Figure 3. 3D path recovery simulation. See text for details.

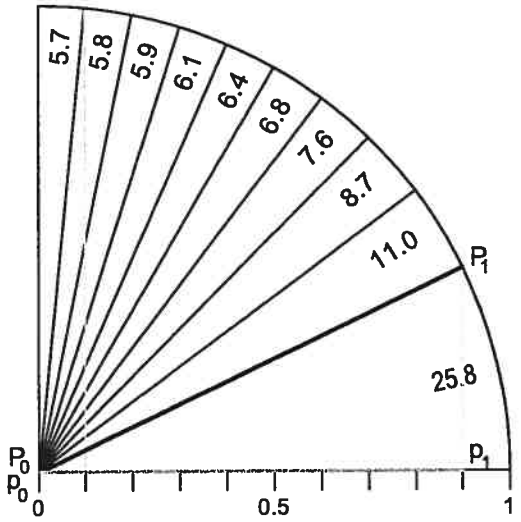

Figure 4. Effect of the projection foreshortening by step of 10% on the angulation variation. Segment $[p_1, p_2]$ represents the projection of segment $[P_1, P_2]$ (the transducer) on the projection plane, which is coincident with the abscissa.

was divided in segments of 0.5 cm, corresponding to the transducer length. In figure 3 only segments S_1 and S_i are shown. Each of the segments were projected using one of the projection geometry previously described. The resulting data simulate the cine-angiographic images of the IVUS transducer during a pull-back.

From this point on, the real reconstruction procedure begins. For the first frame, we take the projection plane coordinates $[p_1^1, p_2^1]$ and an estimated depth coordinate P_1^1 in order to derive the depth coordinate for point P_2^1. For frame $i+1$, the procedure is repeated with $P_1^{i+1} = P_2^i$. By using the recovered depth coordinates at once, we are able to represent the path in 3D. Although there exist two solutions for each frame, since a square root is involved in the depth recovery, selecting the correct solution is facilitated by the fact that for two adjacent frames, the path cannot reverse direction. An ambiguity still exist when the path becomes parallel to the projection plane, at which point it is numerically impossible to know if the transducer, on the next frame, will go away or toward the projection plane. Using heuristics like the heart maximum size or the general shape of the vessels can help alleviate such ambiguities.

4. Error analysis

The precision in the transducer path reconstruction is dependent on the estimated or measured values of many parameters. Here we briefly discuss the effects that have an error in the measured projection foreshortening length or in the initial depth localisation in full and weak perspective geometry.

Because of the trigonometric nature of the projection geometry, for a constant foreshortening effect, the estimated angular variation of the transducer will depends on its initial angle. In figure 4, we can see that a variation of 10% on the projected length of the transducer placed parallel to the projection plane, gives an angular variation of 25.8 ° compared to an angular variation of only 5.7 ° when the transducer is placed at an angle of 84.3 ° from the projection plane. This expresses the fact that whatever technique is used to recover the 3D orientation from a projection, the error margin will be greater as the transducer tends to be parallel to the projection plane. This effect can be found on the angiogram where the continuous nature of the projected length of the transducer is quantized by the pixel representation. If we use typical values for field of view of 10 cm, transducer length of 0.5 cm and an angiography image resolution of 1024 x 1024 pixels, the variation of the projected length would be less than 2% the transducer length. At worst, for a transducer oriented at 0 °, this would produce an angular variation of 11 °.

In the full perspective geometry (see figure 5), when we do a back-projection of two fixed points $[p_1, p_2]$, for a constant length d and for different fixed 3D points P_1^i, we get different solutions for points P_2^i. Each of these segments has a different angulation. The relation between the 3D points P_1^i and the resulting segment's angulation is that, if we over estimate the 3D location of a point, the angulation will be underestimated. By using typical values for the location of the projection plane and object plane of 100 cm and 75 cm respectively, a depth of view of 10 cm (the normal heart size), and a transducer length of 0.5 cm, it is possible to determine the worst case error in angulation estimation. An error of ±5 cm in the estimated depth coordinate, with

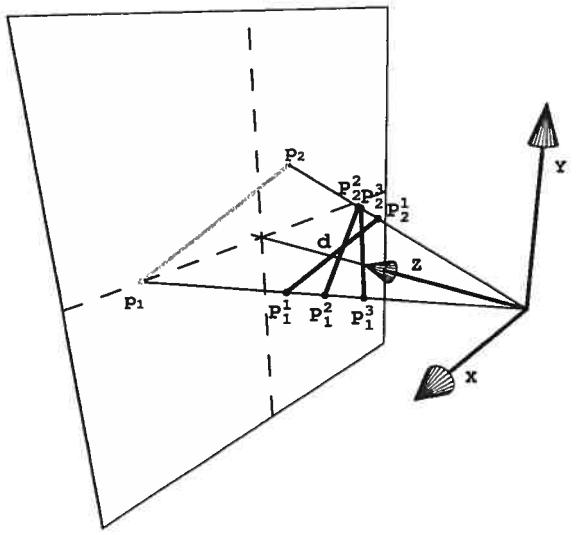

Figure 5. Multiple solutions of back-projection in the full perspective projection geometry. See text for details.

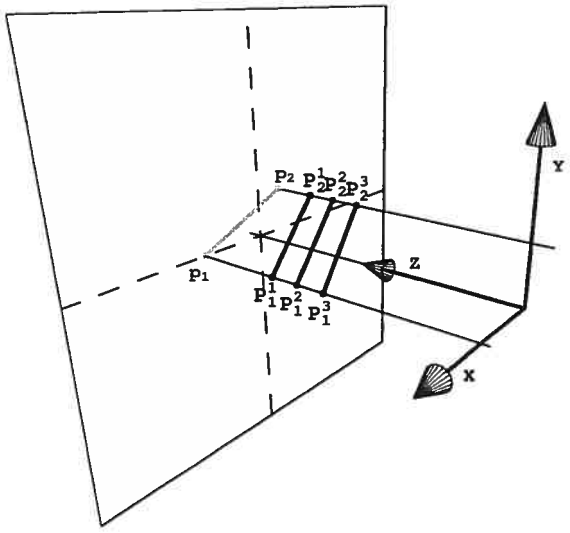

Figure 6. Multiple solutions of back-projection in the orthographic projection geometry. See text for details.

a transducer placed at 0° results in a variation of estimated angulation of $\pm 20^\circ$, decreasing rapidly to $\pm 3^\circ$ when the transducer is placed at 45°.

In the case of weak perspective or orthographic projections (figure 6), the angulation of the 3D segments $[P_1^i, P_2^i]$, found by back-projection of segment $[\mathbf{p}_1, \mathbf{p}_2]$, is irrelevant on the initial 3D point estimation P_1^i. This is an interesting aspect of the weak perspective geometry, besides simplified calculations. In the worst case, if we compare the full perspective to the weak perspective geometry, we get the same angular variation than when an initial 3D point location is miss estimated, in the full perspective geometry alone.

5. Conclusion

We have sketch a solution to get 3D information about the angle of the transducer of an IVUS catheter from a single-plane angiographic image. Analytical formulations were derived. Three projection geometries were examined, and we found that the weak perspective geometry being a simplified approximation, shows worst case value errors similar to the full perspective geometry, despite the fact that no depth information is necessary. Depth recoveries were done on simulated projections and found to be conclusive. The validation of the method using a phantom is underway and will be presented in a future article.

References

[1] J. R. Roelandt, C. di Mario, N. G. Pandian, L. Wenguang, D. Keane, C. J. Slager, P. J. de Feyter, and P. W. Serruys, "Three-dimensional reconstruction of intracoronary ultrasound images. rationale, approaches, problems, and directions," *Circulation*, vol. 90, no. 2, pp. 1044–55, 1994.

[2] C. J. Slager, J. J. Wentzel, J. C. Schuurbiers, J. A. Oomen, J. Kloet, R. Krams, C. von Birgelen, W. J. van der Giessen, P. W. Serruys, and P. J. de Feyter, "True 3-dimensional reconstruction of coronary arteries in patients by fusion of angiography and ivus (angus) and its quantitative validation," *Circulation*, vol. 102, no. 5, pp. 511–6, 2000.

[3] A. Wahle, S. C. Mitchell, S. D. Ramaswamy, K. B. Chandran, and M. Sonka, "Four-dimensional coronary morphology and computational hemodynamics," in *Medical Imaging 2001: Image Processing*, M. Sonka and K. M. Hanson, Eds., Bellingham WA, 2001, vol. 4322, pp. 743–754, SPIE Proceedings.

[4] R. Medina, A. Wahle, M. E. Olszewski, and M. Sonka, "Volumetric quantification of coronary arteries reconstructed by fusion between intravascular ultrasound and biplane angiography," *Biomedical Imaging, 2002. Proceedings. 2002 IEEE International Symposium on*, pp. 891–894, 2002.

[5] E. Trucco and A. Verri, *Introductory Techniques for 3-D Computer Vision*, Prentice Hall, 1998.

Annexe C

3D TRAJECTORY ASSESSMENT OF AN IVUS TRANSDUCER FROM SINGLE-PLANE CINEANGIOGRAMS : A PHANTOM STUDY

Référence [70] : D. Sherknies, J. Meunier, R. Mongrain, et J. C. Tardif. 3D trajectory assessment of an ivus transducer from single-plane cineangiograms : a phantom study. Dans *Proceedings of the 25th Annual International Conference of the IEEE Engineering in Medicine and Biology Society,* volume 1, pages 690–693. IEEE ; Piscataway, NJ, USA, 2003.

3D Trajectory Assessment of an IVUS Transducer from Single-Plane Cineangiograms: a Phantom Study

D. Sherknies[1], J. Meunier[1], R. Mongrain[2], J. C. Tardif[2]
[1]Department of Computer Science and Operations Research, University of Montreal, Quebec, Canada
[2]Montreal Heart Institute, Quebec, Canada

Abstract—**The recovery of the 3D path of the transducer used during an Intravascular Ultrasound (IVUS) examination is of primary importance to assess the exact 3D shape of the vessel under study. Traditionally, the reconstruction is done simply by stacking the images during the pullback, or more recently using biplane angiography to recover the vessel curvature.**

In this paper, we apply the formulation of a perspective projection model, which enables us to determine the angulations of an IVUS transducer from single-plane angiogram only.

The transducer angulation reconstruction is based on the foreshortening effect as seen from the X-ray images. By comparing the measured to the true transducer length, we are able to get its incidence angle. The transducer trajectory is reconstructed by stitching together the different estimated angulations obtained from each image in a cineangiogram sequence.

The method is described and validated on a helical vessel phantom.

Keywords—**3D reconstruction, IVUS, phantom, single-plane angiography**

I. Introduction

Because of their complementary nature, the two imaging modalities, X-ray angiography and intravascular ultrasound (IVUS), are increasingly being studied and used together. Angiography provides a mean to display the overall vessel morphology, while IVUS gives an accurate composition of the vessel cross-section [1].

In order to provide a more informative assessment of the vessel lumen and plaque dimensions, the 2D IVUS images are reconstructed in 3D by stacking the different images taken during the pullback of the transducer. At first the images were stacked as to create a straight tube [2]. By neglecting the vessel curvature this method introduced incorrect volumetric representation. Biplane cineangiography was later used to recover the transducer orientation and precise 3D localization [3-5], but these apparatus are complicated to operate and are not always available in clinical centers.

In this article we summarize the formulation previously developed in [6], that enables us to determine the 3D orientation of a segment from its perspective projection. The method is validated on a helical phantom in which the pullback of an IVUS transducer was recorded on a single-plane cineangiogram.

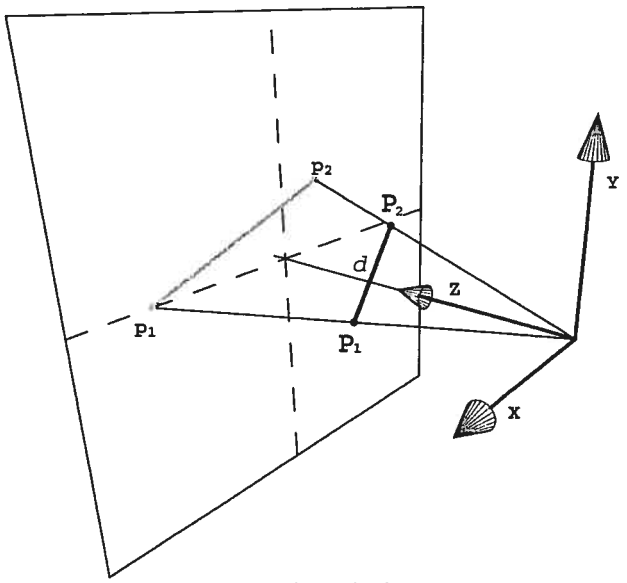

Fig. 1. Full perspective projection geometry. $[P_1,P_2]$: Catheter transducer 3D segment; $[p_1,p_2]$: Transducer projection 2D segment; d : Known length of $[P_1,P_2]$.

II. Methodology

A. Depth Recovery Method

If we define $P_i=[X_i,Y_i,Z_i]$ as a 3D point and $p_i=[u_i,v_i]$ a 2D point, the relation between P_i and its projection p_i, for a pin-hole camera model, is given by

$$u_i=f\frac{X_i}{Z_i} \text{ and } v_i=f\frac{Y_i}{Z_i}, \quad (1)$$

where f is the focal distance [7]. We assume here that the camera is placed at the origin in the 3D space, that the projection plane is perpendicular to the *Z-axis* and is centered on it (Fig.1).

Using $P_2=[X_2,Y_2,Z_2]$ and its projection $p_2=[u_2,v_2]$, (1) can be rewritten with some manipulation as

$$Z_2=f\frac{X_2}{u_2} \text{ and } Y_2=v_2\frac{X_2}{u_2}. \quad (2)$$

The Euclidian distance of segment $[P_1, P_2]$

$$d=\sqrt{(X_2-X_1)^2+(Y_2-Y_1)^2+(Z_2-Z_1)^2}, \quad (3)$$

can be rewritten, using (2), as

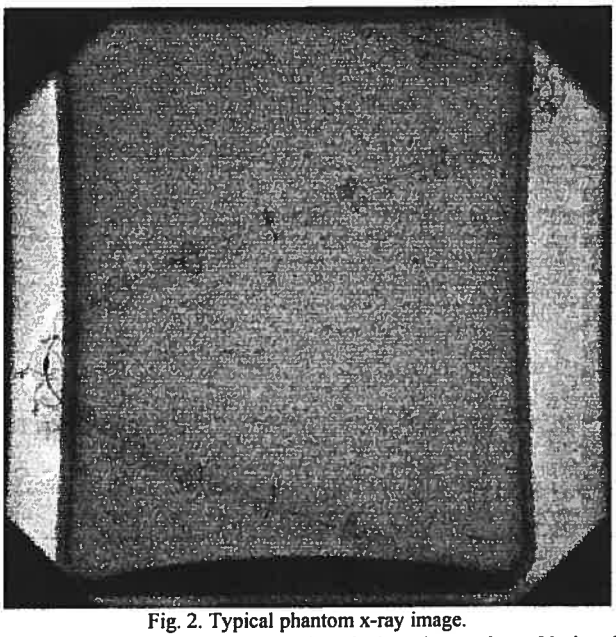

Fig. 2. Typical phantom x-ray image.
The guide wire is visible, passing though the wire markers. Notice the transducer projection on the left of the image.

$$d=\sqrt{(X_2-X_1)^2+(v_2\frac{X_2}{u_2}-Y_1)^2+(f\frac{X_2}{u_2}-Z_1)^2}, \quad (4)$$

which solved for X_2 gives

$$X_2=\frac{u_2 a\pm\sqrt{u_2^2\,[a^2+b(d^2-X_1^2-Y_1^2-Z_1^2)]}}{b}, \quad (5)$$

where $a=u_2X_1+v_2Y_1+fZ_1$ and $b=f^2+u_2^2+v_2^2$.

By substituting (5) in (2) we are able to find the 3D coordinates of $\boldsymbol{P}_2$ knowing the location of two projected points $\boldsymbol{p}_1$, $\boldsymbol{p}_2$, the location of a 3D point $\boldsymbol{P}_1$ and the distance between two 3D points d. This method is called the *depth recovery method.*

B. Material

A helical phantom was constructed consisting of a 0.32cm silicon tubing wrapped around a beaker of 13cm in height and 10.9cm in diameter. Wire markers were placed on the phantom, 2cm apart, to provide radiopaque landmarks (Fig. 2).

The IVUS catheter (*Endosonics Avanar F/X*) used for this experiment, measured 0.097cm in diameter and the transducer length was 0.7cm.

The pullback was done using a *JOMED TrackBack II* catheter pullback device at a speed of 0.1cm/s over a guide wire of 0.036cm in diameter.

The single-plane cineangiograms were taken on a *Siemens AXIOM ARTIS FC* X-ray imaging system. The digital images were saved in the *DICOM* format using the *Syngo* clinical information systems.

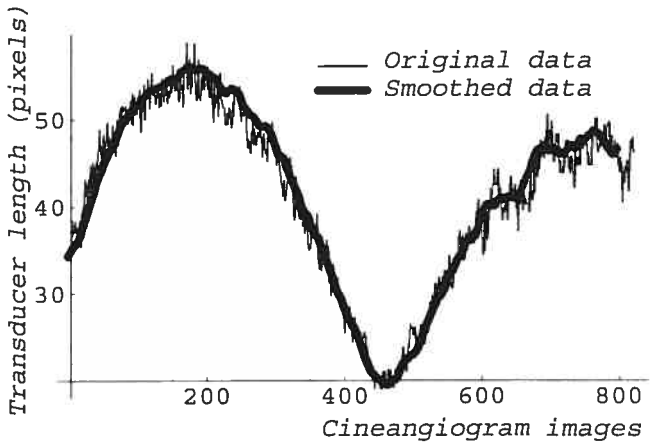

Fig. 3. Original and smoothed data of the measured transducer length.

C. Images

The images were obtained by placing the phantom in water to attenuate X-ray intensity. The automatic pullback was recorded on the X-ray imaging system at a frame rate of 4 fps (frame per second) and at a resolution of 1,024 pixels x 1,024 pixels (Fig. 2). The focal distance f was 94.5 cm.

D. Transducer 3D Trajectory Reconstruction

Let us define each image in a cineangiogram as $\boldsymbol{G}^J$. For each image corresponds a segment $\boldsymbol{S}^J=[\boldsymbol{P}_1^J,\boldsymbol{P}_2^J]$, the 3D localization of the transducer tips, and a segment $\boldsymbol{s}^J$, the transducer's projection. The distal extremity, in relation to the transducer pullback direction, is labeled as $\boldsymbol{p}_1^J$, the proximal extremity as $\boldsymbol{p}_2^J$.

For each X-ray image, each extremity of the transducer was manually registered using a custom program. The data lengths were then smoothed to attenuate the manipulation errors (Fig. 3) using an exponential weighted average with a smoothing constant of 0.5.

In order to apply our previously described *depth recovery method* on each segment $\boldsymbol{s}^J$, we need a good estimation of the depth coordinate of $\boldsymbol{P}_1^J$. That is because, in full perspective projection model, the depth coordinate of $\boldsymbol{P}_1^J$ influences the recovered orientation (see [6] for detail). Since the phantom is helical, the frame $\boldsymbol{G}^a$ containing the longest segment $\boldsymbol{s}^a$, corresponds to a transducer 3D orientation that is parallel to the projection plane. In order to find the best starting configuration, on frame $\boldsymbol{G}^a$, the depth coordinate of $\boldsymbol{P}_1^a$ was constrained so that it be equal to $\boldsymbol{P}_2^a$ (Fig. 4).

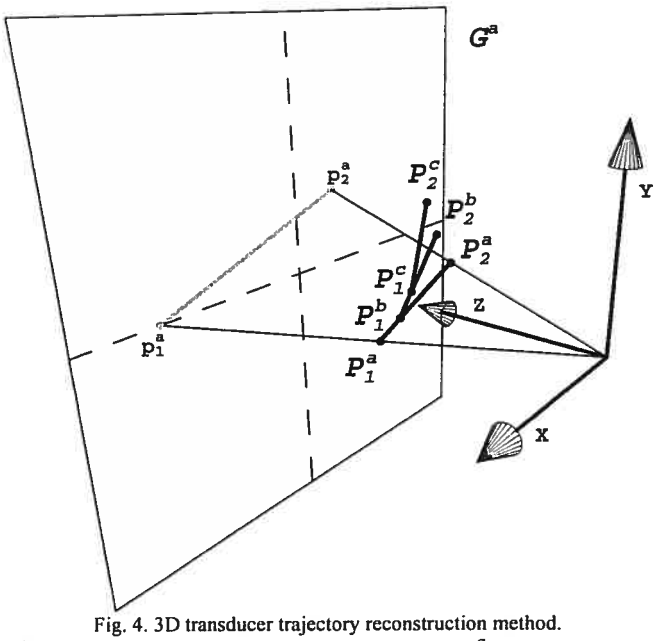

Fig. 4. 3D transducer trajectory reconstruction method.
P_i^J: Extremities of reconstructed 3D localization; p_i^a: Projected points. Only the projection plane G^a is shown. See text for detail.

To estimate the next depth coordinate P_i^b, where $b=a+1$, we simplified the transducer's 3D trajectory in a piecewise linear manner and displaced P_i^b along the segment S^a in concordance with the transducer pullback speed. P_i^b was found using the *depth recovery method* (Fig. 4). The process was repeated for the other S^J.

E. Helical Phantom Model

In order to assess the validity of our reconstruction method, we created a computer model of our phantom. The *helical phantom model* was positioned by translations and rotations along the three axes, to correctly localize it in the virtual 3D environment. The transformation parameters were found by minimizing the RMS distance between the *helical phantom model* projection and the centerline projection of the phantom, which correspond to the guide wire, measured on image G^1 (Fig. 5).

III. Results and Discussion

Once reconstructed the transducer 3D trajectory was compared to the *helical phantom model* using a RMS distance measure (Fig. 5). Expressed in cm the average RMS distance value is 0.5656 (SD ± 0.2316), with a median of 0.6272, a minimum and maximum value of 0.1687 and 0.8779, respectively. The reconstructed trajectory expresses the overall shape of the phantom, but generally underestimates the curvature. This might be explained by the fact that our reconstruction method depends on the pullback speed. Underestimating the pullback speed gives a

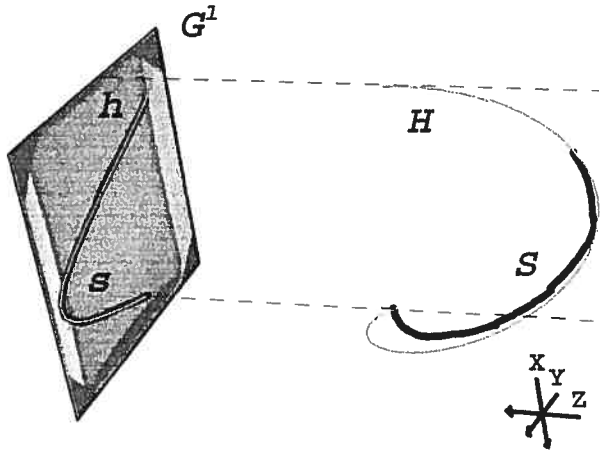

Fig. 5. Transducer 3D trajectory reconstruction assessment.
H: Helical phantom model; h: Phantom centerline projection (guide wire); S: Transducer 3D trajectory reconstruction; s: Stacked measured transducer projections; G^1: First frame in the cineangiogram.

compressed reconstruction along the *Z*-axis, and vice versa. Informal tests have shown us that the catheter speed, assumed constant, could vary slightly with the pullback device used in this study.

Another aspect of the reconstruction method is that any mirror reflection of a segment, parallel to the projection plane, will give the same projection (Fig. 6). When reconstructing, a heuristic must be used in order to choose among the possible solutions. Since our phantom was helical, we constrained the reconstruction to create a concave shape. Using our method *in vivo* would imply a similar heuristic since, depending on the projection angle, the heart shape can be simplified as an ellipsoid.

Because of the trigonometric nature of our reconstruction method, it is sensible to foreshortening errors

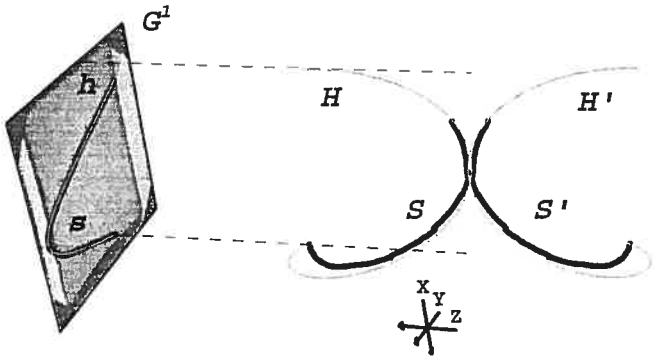

Fig. 6. Possible solutions for the transducer 3D trajectory reconstruction.
H': Helical phantom model reflection; S': Transducer 3D trajectory reconstruction reflection. Every combinations of the top and bottom part of S *and* S' would yield acceptable solutions based on their projection only.

especially when the transducer orientation is parallel to the projection plane (see [6]). However, since we noted typical transducer maximum length of approximately 50 pixels, this implies a relatively small theoretical minimum error of 11.5 deg., decreasing rapidly as the transducer orientation becomes less parallel to the projection plane.

IV. Conclusion

We have applied and assessed a method to recover the 3D trajectory of a catheter transducer, based on single-plane angiogram of a helical phantom using full perspective projection model. The path curvature was in good part recovered, being on average less than 6 mm distant from the true path. Our method could be improved by alleviating its dependency on the knowledge of the transducer pullback speed.

Acknowledgment

The authors thank the technicians, Colette Desjardins and Joanne Vincent, the engineer, Pierre Le Guyader, and Dr. Jacques Lesperance from the *Montreal Heart Institute*, for their help in the acquisition of the phantom images.

References

[1] X. Zhang, C. R. McKay, and M. Sonka, "Tissue characterization in intravascular ultrasound images," *IEEE Trans. Med. Imag.*, vol. 17, pp. 889–899, Dec. 1998.

[2] J. R. Roelandt, C. di Mario, N. G. Pandian, L. Wenguang,D. Keane, C. J. Slager, P. J. de Feyter, and P. W. Serruys, "Three-dimensional reconstruction of intracoronary ultrasound images. rationale, approaches, problems, and directions," *Circulation*, vol. 90, no. 2, pp. 1044–55, 1994.

[3] C. J. Slager, J. J. Wentzel, J. C. Schuurbiers, J. A.Oomen, J. Kloet, R. Krams, C. von Birgelen, W. J.van der Giessen, P. W. Serruys, and P. J. de Feyter,"True 3-dimensional reconstruction of coronary arteries in patients by fusion of angiography and ivus (angus) and its quantitative validation," *Circulation*, vol.102, no. 5, pp. 511–6, 2000.

[4] A. Wahle, S. C. Mitchell, S. D. Ramaswamy, K. B.Chandran, and M. Sonka, "Four-dimensional coronary morphology and computational hemodynamics,"in *Medical Imaging 2001: Image Processing*, M. Sonkaand K. M. Hanson, Eds., Bellingham WA, 2001, vol.4322, pp. 743–754, SPIE Proceedings.

[5] R. Medina, A. Wahle, M. E. Olszewski, and M. Sonka, "Volumetric quantification of coronary arteries reconstructed by fusion between intravascular ultrasound andbiplane angiography," *Biomedical Imaging, 2002. Proceedings.2002 IEEE International Symposium on*, pp.891–894, 2002.

[6] D. Sherknies, J. Meunier, and J. C. Tardif, "3D path recovery of an ivus transducer with single-plane angiography," in Proc. *IEEE CCECE2003, Canadian Conference on Electrical and Computer Engineering*, in press.

[7] E. Trucco and A. Verri, *Introductory techniques for 3-D computer vision*. Prentice Hall, 1998

Annexe D

3D TRAJECTORY ASSESSMENT OF AN IVUS TRANSDUCER FROM SINGLE-PLANE CINEANGIOGRAMS : A PHANTOM STUDY

Poster présenté à la conférence [70] : D. Sherknies, J. Meunier, R. Mongrain, et J. C. Tardif. 3D trajectory assessment of an ivus transducer from single-plane cineangiograms : a phantom study. Dans *Proceedings of the 25th Annual International Conference of the IEEE Engineering in Medicine and Biology Society,* volume 1, pages 690–693. IEEE ; Piscataway, NJ, USA, 2003.

3D Trajectory Assessment of an IVUS Transducer from Single-Plane Cineangiograms: a Phantom Study

D. Sherknies[1], J. Meunier[1], R. Mongrain[2], J. C. Tardif[2]

[1]Department of Computer Science and Operations Research, University of Montreal, Quebec, Canada
[2]Montreal Heart Institute, Quebec, Canada

Université de Montréal

Abstract

The recovery of the 3D path of the transducer used during an Intravascular Ultrasound (IVUS) examination is of primary importance to assess the exact 3D shape of the vessel under study. Traditionally, the reconstruction is done simply by stacking the images during the pullback [1], or more recently using biplane angiography to recover the vessel curvature [2].

In this paper, we apply the formulation of a perspective projection model, which enables us to determine the angulations of an IVUS transducer from single-plane angiogram only.

The transducer angulation reconstruction is based on the foreshortening effect as seen from the X-ray images. By comparing the measured to the true transducer length, we are able to get its incidence angle. The transducer trajectory is reconstructed by stitching together the different estimated angulations obtained from each image in a cine-angiogram sequence.

The method is described and validated on a helical vessel phantom.

Depth recovery equation

If we define a 3D point, $\mathbf{P}_i=[X_i, Y_i, Z_i]$, and its projection, $\mathbf{p}_i=[u_i, v_i]$. By combining the perspective camera fundamental equations [3]

$$u_i = f\frac{X_i}{Z_i}, v_i = f\frac{Y_i}{Z_i}$$

and the Euclidian distance equation of segment $S=[\mathbf{P}_1, \mathbf{P}_2]$

$$d = \sqrt{(X_2-X_1)^2+(Y_2-Y_1)^2+(Z_2-Z_1)^2},$$

we obtain a depth recovery equation

$$\mathbf{P}_2 = \left[\frac{u_2 a \pm \sqrt{u_2^2\left[a^2+b(d^2-X_1^2-Y_1^2-Z_1^2)\right]}}{b}, v_2\frac{X_2}{u_2}, f\frac{X_2}{u_2}\right],$$

where $a = u_2X_1 + v_2Y_1 + fZ_1$, $b = f^2+u_2^2+v_2^2$. This states that knowing the length d of segment S, the location of its projected extremities $\mathbf{p}_1$, $\mathbf{p}_2$ and the location of one of its extremity $\mathbf{P}_1$, it is possible to recover the location of its other extremity $\mathbf{P}_2$ [4].

Transducer 3D Trajectory Reconstruction

1) For each X-ray image in the cineangiogram sequence, each extremity $[\mathbf{p}_1, \mathbf{p}_2]$ of the transducer is manually registered;
2) On the first image, the depth coordinate of point $\mathbf{P}_1$ is estimated, based on information in the DICOM file;
3) Point $\mathbf{P}_2$ is localized using our depth recovery equation;
4) For the next frame, point $\mathbf{P}_1$ position is based on the previous frame's calculated transducer location and on the pullback speed;
5) Goto step 3.

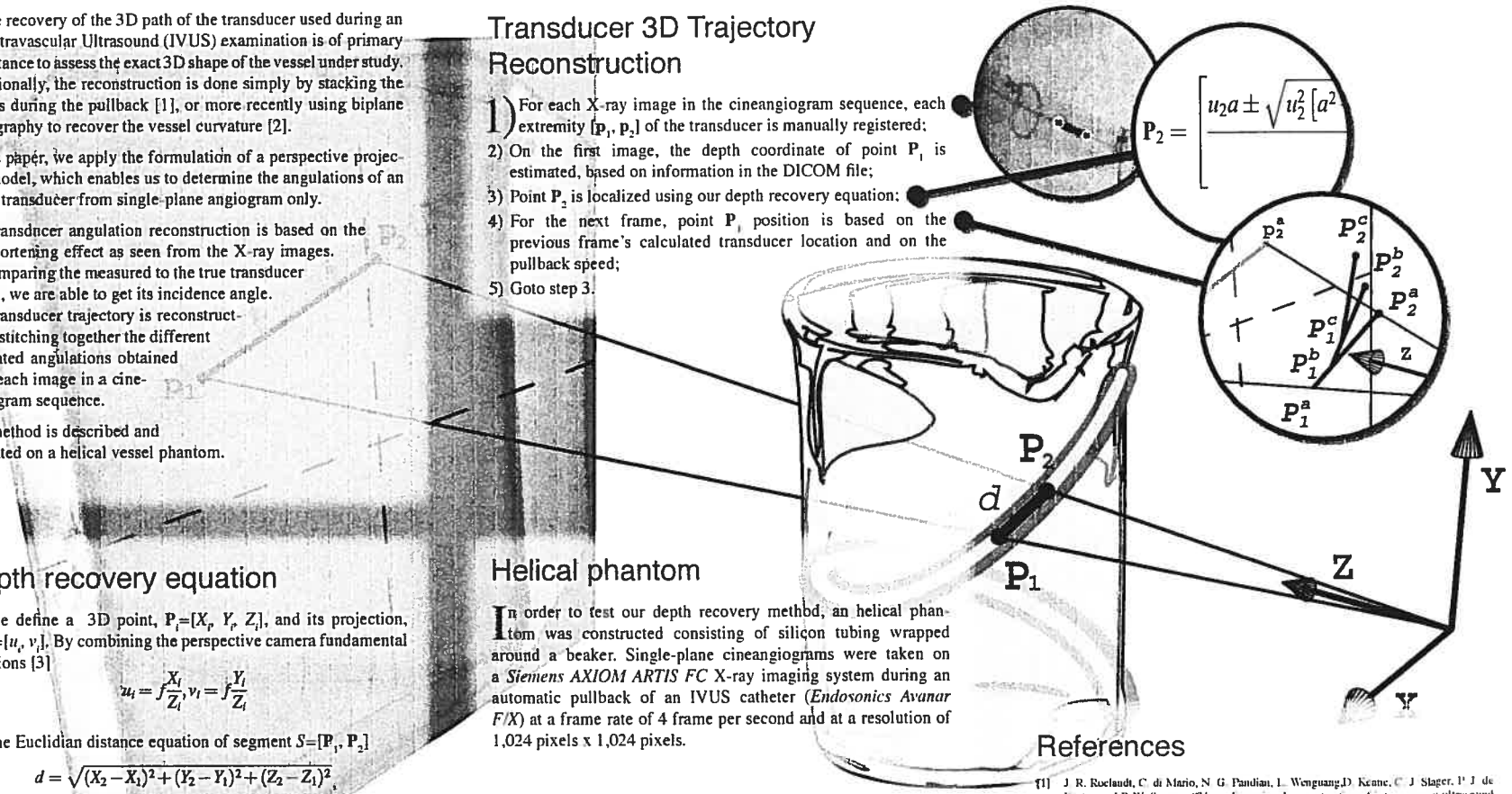

Helical phantom

In order to test our depth recovery method, an helical phantom was constructed consisting of silicon tubing wrapped around a beaker. Single-plane cineangiograms were taken on a *Siemens AXIOM ARTIS FC* X-ray imaging system during an automatic pullback of an IVUS catheter (*Endosonics Avanar F/X*) at a frame rate of 4 frame per second and at a resolution of 1,024 pixels x 1,024 pixels.

Conclusion

We have applied and assessed a method to recover the 3D trajectory of a catheter transducer, based on single-plane angiogram of a helical phantom using full perspective projection model. The path curvature was in good part recovered, being on average less than 6 mm distant from the true path (5.656 mm ± 2.316 mm). Our method could be improved by alleviating its dependency on the knowledge of the transducer pullback.

References

[1] J. R. Ruelandt, C. di Mario, N. G. Pandian, L. Wenguang, D. Keane, C. J. Slager, P. J. de Feyter, and P. W. Serruys, "Three dimensional reconstruction of intracoronary ultrasound images. rationale, approaches, problems, and directions," *Circulation*, vol. 90, no. 2, pp. 1044–55, 1994.

[2] R. Medina, A. Wahle, M. E. Olszewski, and M. Sonka, "Volumetric quantification of coronary arteries reconstructed by fusion between intravascular ultrasound and biplane angiography," *Biomedical Imaging, 2002. Proceedings.2002 IEEE International Symposium on*, pp 891–894, 2002.

[3] E. Trucco and A. Verri, Introductory techniques for 3-D computer vision, Prentice Hall, 1998.

[4] D. Sherknies, J. Meunier, and J. C. Tardif, "3D path recovery of an IVUS transducer with single-plane angiography," in *Proc. IEEE CCECE2003 Canadian Conference on Electrical and Computer Engineering*, in press.

Annexe E

3D HEART MOTION FROM SINGLE-PLANE ANGIOGRAPHY OF THE CORONARY VASCULATURE : A MODEL-BASED APPROACH

Référence [72] : D. Sherknies, J. Meunier, et J. C. Tardif. 3D heart motion from single-plane angiography of the coronary vasculature : a model-based approach. Dans *Proceedings of the SPIE - The International Society for Optical Engineering, Medical Imaging 2004 : Image Processing*, volume 5370, pages 381–389. SPIE Press, Mai 2004.

3D Heart Motion from Single-Plane Angiography of the Coronary Vasculature: a Model-Based Approach

Denis Sherknies[a], Jean Meunier[a] and Jean-Claude Tardif[b]

[a]Department of Computer Science and Operations Research,
University of Montreal, Montreal, Canada;
[b]Montreal Heart Institute, Montreal, Canada

ABSTRACT

In order to complete a thorough examination of a patient heart muscle, physicians practice two common invasive procedures: the ventriculography, which allows the determination of the ejection fraction, and the coronarography, giving among other things, information on stenosis of arteries. We propose a method that allows the determination of a contraction index similar to ejection fraction, using only single-plane coronarography. Our method first reconstructs in 3D, selected points on the angiogram, using a 3D model devised from data published by Dodge *et al.*[1,2] We then follow the point displacements through a complete heart contraction cycle. The objective function, minimizing the RMS distances between the angiogram and the model, relies on affine transformations, i.e. translation, rotation and isotropic scaling. We validate our method on simulated projections using cases from Dodge *et al.* data. In order to avoid any bias, a leave-one-out strategy was used, which excludes the reference case when constructing the 3D coronary heart model. The simulated projections are created by transforming the reference case, with scaling, translation and rotation transformations, and by adding random 3D noise for each frame in the contraction cycle. Comparing the true scaling parameters to the reconstructed sequence, our method is quite robust ($R^2 = 96.6\%, P < 1\%$), even when noise error level is as high as 1 cm. Using 10 clinical cases we then proceeded to reconstruct the contraction sequence for a complete cardiac cycle starting at end-diastole. A simple heart contraction mathematical model permitted us to link the measured ejection fraction of the different cases to the maximum heart contraction amplitude ($R^2 = 57\%$ with $P < 1\%$) determined by our method.

Keywords: 3D model, 3D reconstruction, coronarography, ejection fraction, single-plane angiography

1. INTRODUCTION

The 3D representation of the coronary arteries is an effervescent research topic aiming at morphological and functional analysis. The 3D reconstruction usually involves two or more views, the views can be acquired simultaneously by biplane X-ray acquisition apparatus[3–5] or sequentially by rotating a single-plane acquisition device.[6–8] Some reconstructions have also been made by using non-rotating single-plane angiograms only.[9]

Reconstructions made with multiple views are mainly realized by finding feature correspondences between images using epipolar geometry constraint.[10,11] With non-rotating single-view reconstruction, since the depth information is lost, the process must rely on other means. In the case of Nguyen *et al.* the depth information was extrapolated by fitting together features from sequential view of the cineangiogram with a center of contraction constraint. The method we propose, infer depth information by using a 3D coronary tree model. Even if variations exist in the tortuosity and localization of coronary arteries, certain structural characteristics exist, as expressed by the existence of anatomical heart atlas.[12] These structural characteristics are also used in the 3D reconstruction process.[13–15] Our 3D reconstruction method relies on inter-patient similarities for fitting the projection of a coronary tree model to selected points along arteries.

Kong *et al.*[16] were the first to propose the use of variations in the coronary tree length, measured from 3D reconstruction, to quantify heart contractions. We use the 3D reconstruction to extract a contraction amplitude index from coronarography, similar to the ventriculography ejection fraction index used in the diagnostic of the overall heart health. The conception of the model and the method used to acquire a contraction index from simulated and clinical data is presented and discussed.

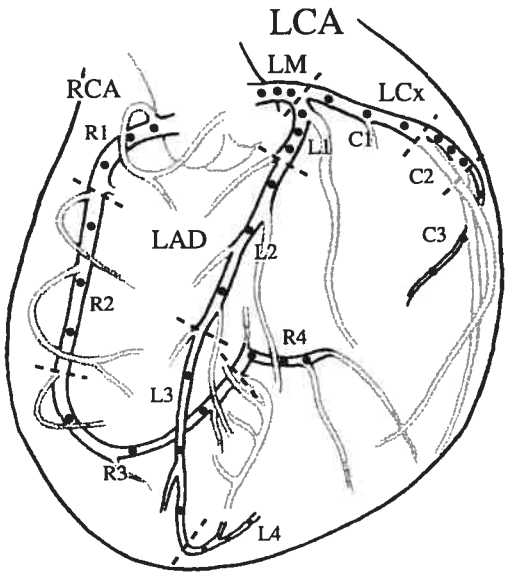

Figure 1. Reference point locations along the right and left primary coronary arteries. From Dodge *et al.* original data (gray section), only the right coronary artery (RCA), the left main (LM), left circumflex (LCx) and left anterior descending (LAD) arteries were considered in our 3D coronary tree model (dark section). See text for details.

2. MATERIAL AND METHODS

2.1. 3D coronary tree model

The central element in our reconstruction method from single-plane images is the *3D coronary tree model.* This coronary tree model is based on the data used in two articles by Dodge *et al.*[1,2] where the 3D location of 102 points along the coronary tree of 37 normal subjects using bi-plane angiography were measured. The point locations are based on trisected artery segments. The segments are delimited by anatomical landmarks like artery bifurcations. The different reference points were distributed along the right and left coronary arteries and also along the main branches and their secondary tributaries.

We constructed our 3D coronary tree model using a subset of Dodge *et al.* data. Only the reference points along the major left coronary branches (LCA) and right coronary branches (RCA) were considered because the selected points had to be present for every subjects. We ended up with 26 subjects matching our selection criteria, the *subject models* . Using the nomenclature defined by Dodge *et al.* the distribution of the 36 points along the coronary branches is as follows, Fig. 1:

- 12 points on the RCA subdivided as the R1, R2, R3 and R4 segments;
- 3 points on the left main artery (LM), the joint base between the left anterior descending artery (LAD) and the left circumflex artery (LCx);
- 12 points on the LAD subdivided as L1, L2, L3 and L4 segments;
- and 9 points on the LCx subdivided as C1, C2 and C3 segments.

Refining the method described in a previous article,[17] the model definition of the 3D coronary tree model is realized using global and local components. The global component refers to a transformation that is applied to all the points composing the model, the local component is a more subtle transformation specific to each of the model points.

The global component attenuates inter-subject variations, like heart size, and relative body position during data acquisition. Local component attenuates the specific characteristics caused by the choice of the *reference subject.*

Table 1. Clinical cases demographic details

Patient	Sex	Age	Ejection fraction (%)
JO	M	80	24
ME	F	58	25
RA	M	65	32
MA	M	61	50
LE	F	61	55
BI	M	79	60
EL	M	60	60
AL	M	62	60
CL	F	70	65
CH	M	55	75

2.1.1. Global component

The steps involved in the elaboration of the global component can be described as follows:

A well-formed subject is chosen as a *reference subject*. Well-formed being defined as a subject with clearly defined arterial branches.

The *reference subject* is fitted, with affine transformations (translation, rotation and scaling), to each of the other subjects, the *target subjects*. We use a simulated annealing technique to minimize the sum of the Euclidean distances between the *reference subject* and the *target subject* corresponding points. The objective function used is $\sum_{i=1}^{n} \|\mathbf{P}_i^r \cdot \mathbf{M} - \mathbf{P}_i^t\|^2$, where $\mathbf{P}_i^r$ and $\mathbf{P}_i^t$ are respectively the 3D *reference subject* and *target subject* points and n is the total number of 3D reference points. $\mathbf{M}$ is the aggregated matrix made of the rotation matrices around the x, y and z axes, an isotropic scaling parameter and a translation vector along the 3 orientation axes.[18]

The global component in the definition of our model is obtained by applying on the *reference subject* the average rotation, scaling and translation parameters found in the minimization process. This gives us the *adjusted reference subject*.

2.1.2. Local component

The local component in our 3D coronary tree model is obtained by applying a specific displacement for each point of the model. This displacement corresponds to the average residual errors found between the *adjusted reference subject* and the *target subjects*.

2.2. Heart contraction simulation

To test our 3D heart motion reconstruction, we did some simulations. To simulate an angiogram, first we used one of the 26 *subject models*, the *simulated case*. The *3D coronary tree model* use to recover the 3D heart motion was then defined (see section 2.1) using a leave-one-out strategy, excluding the *simulated case* from the case pool.

The *simulated case* was then affected by rotation, scaling and translation transformations varying in time, to produce a simulated contraction. Different values were used ranging from $0 - 30°$ for rotations, $1 - 0.8$ for the scaling factor and $0 - 0.5$ cm for translation. This dynamic *simulated case* was projected frame by frame giving the *simulated case projection*, which was the starting point for our recovery method. To stress our recovery method, random noise varying from $0 - 1$ cm was also added around each reference point.

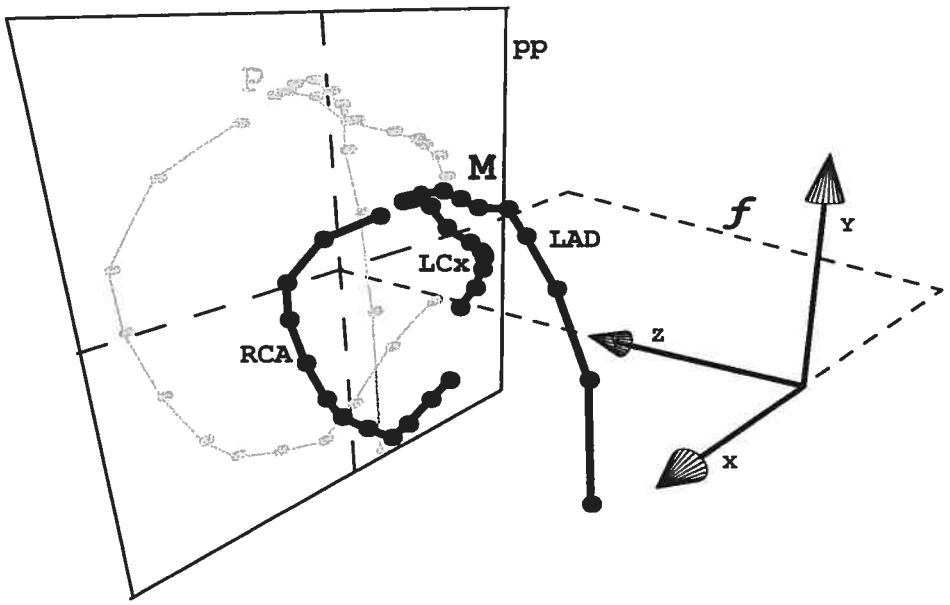

Figure 2. Projection geometry of heart contraction recovery method. The 3D model (M), composed of the RCA, LAD and LCx, is placed between the source of projection (O) and the projection plane (pp), on which we see the reference points projection (P). f: focal distance. See text for detail.

2.3. Angiographic images

The clinical cases used to test our 3D reconstruction method came from the Montreal Heart Institute, they consist of 7 men and 3 women between 55 and 80 years old (65 average) and with ejection fraction varying from 24% to 75% (50.6% average), see Tab. 1 for details. The single-plane cineangiograms were taken on two different X-ray imaging systems. Three cases were obtained with the Siemens AXIOM-Artis and seven with an Electromed Imaging system. The digital images were saved in the DICOM format. For each case, a complete contraction cycle starting at end-diastole was isolated visually with the help of a custom program, using slow-motion and scrubbing (back and forth) techniques, since no recorded synchronized ECG was available. During a coronarography examination, the injection of the contrast agent bolus is done separately for the left and right coronary angiogram. To use both the LCA and RCA together, the images must be registered. Since no registering was done with our clinical case angiograms, only images of the LCA were considered.

In all cases, the reference points used to track the epicardial surface movements were located along the LM, LAD (excluding segment L4) and LCx arteries, giving a total of 21 reference points, see Fig. 1. In some angiograms, a camera movement was detected and was corrected by lateral translations.

2.4. 3D heart contraction recovery method

To follow the 3D heart movement from the projected reference points along the coronaries, some assumptions are made on camera parameters. The center of projection is placed at the center of the projection plane, the angiogram.The focal distance f, distance between the projection plane and the X-ray source, is estimated using information either from the DICOM format when available or from specifications of the angiography apparatus, see Fig. 2. The projection plane was also scaled to remove heart size differences or magnification adjustments used on the angiographic apparatus. The projection plane scaling value was chosen so that the first frame in the contraction sequence had the same size than the adjusted projection of the *3D coronary tree model.*

In order to follow the heart motion, the projection of the model is fitted to the clinical cases with the simulated

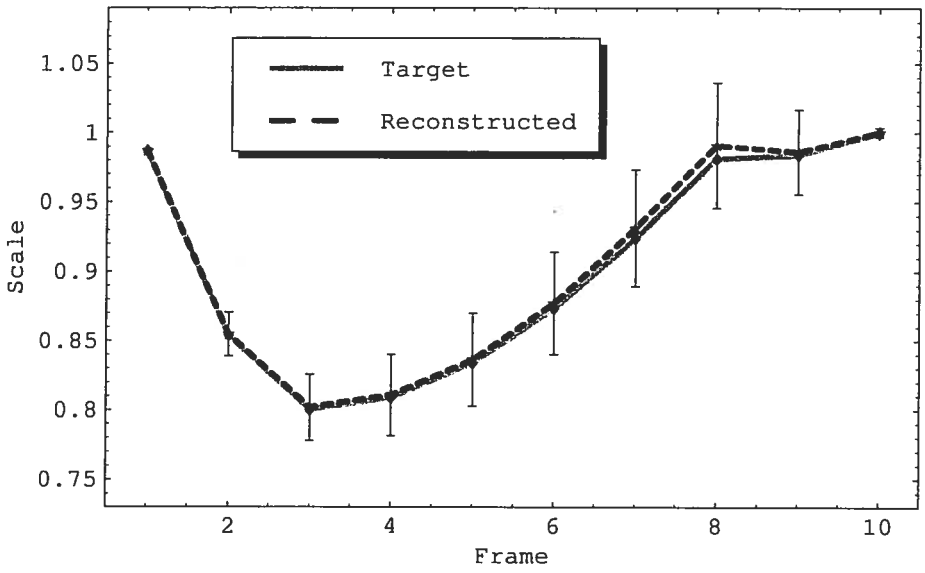

Figure 3. Reconstructed scaling parameter. Comparison between the simulated and the average reconstructed scaling parameter of 25 of the *subject models*. The error bar represents two standard deviations.

annealing technique. The objective function use is

$$\sum_{i=1}^{n} \mathbf{p_i^c} - \mathbf{p_i'} = 0, \tag{1}$$

where n, represent the number of reference points of a simulated or clinial image, $\mathbf{p_i^c}$ is the measured point location of a case, $\mathbf{p_i'}$ is a projected point location of the adjusted model. Two projections models were used, the full-perspective camera model ($\mathbf{p_i'^{FP}} = [fX_i'/Z_i', fY_i'/Z_i']^T$) and the weak-perspective camera model ($\mathbf{p_i'^{WP}} = [f/\overline{Z}X_i', f/\overline{Z}Y_i']^T$).[19] $\overline{Z}$ is define as $\frac{1}{n}\sum_{i=1}^{n} Z_i$ and the points $\mathbf{P_i'} = [X_i', Y_i', Z_i']^T$ are the results of the transformation $\mathbf{P_i'} = \mathbf{M}\mathbf{P}_i$. $\mathbf{P}_i$ beeing the *3D coronary tree model* point locations. Three combinations of transformations were used: $\mathbf{M^{RTS}} = \mathbf{RTS}$, $\mathbf{M^{TS}} = \mathbf{TS}$ and $\mathbf{M^{S}} = \mathbf{S}$. $\mathbf{R}$ denotes rotations around the three main axes, $\mathbf{T}$ the translation along the x and y axes and $\mathbf{S}$ represents an isotropic scaling factor. $\mathbf{p_i'}$ can then take the form of the two projection models, combined with the three transformation methods $\mathbf{p_i'^{(FP|WP,RTS|TS|S)}}$. Each combination is studied and discussed.

3. RESULTS

3.1. Heart contraction simulation

As explained in Sect. 2.2, we created *simulated case projections*. Our goal is to recover the scaling parameter which is our contraction index. Therefore, comparing the scaling factor, used in the construction of the *simulated cases*, to the recovered scaling parameter found by our method, gives a quantitative evaluation on the efficacy of our reconstruction method. For each of the 25 *subject models* (one of the subject was constituting the model), we created different *simulated case projections*. The simulated contractions were spread on 10 frames and were obtained by varying the value in the following parameter ranges: $\mathbf{R}_x$: $0-5°$; $\mathbf{R}_y$: $0-30°$; $\mathbf{R}_z$: $-5-0°$; $\mathbf{T}_x, \mathbf{T}_y, \mathbf{T}_z$: $0-0.5$ cm and $\mathbf{S}$: $1-0.8$. Figure 3 represents the average and the standard deviation of the reconstructed scaling parameter compared to the simulated scaling parameter. The quality of fit is expressed by an R^2 of 99.8% ($P < 1\%$).

To stress the reconstruction method we added random noise to every points in the *simulated case*. Using the same transformation parameters, the noise was spread over increasing circular surface : from 0 to 1 cm in

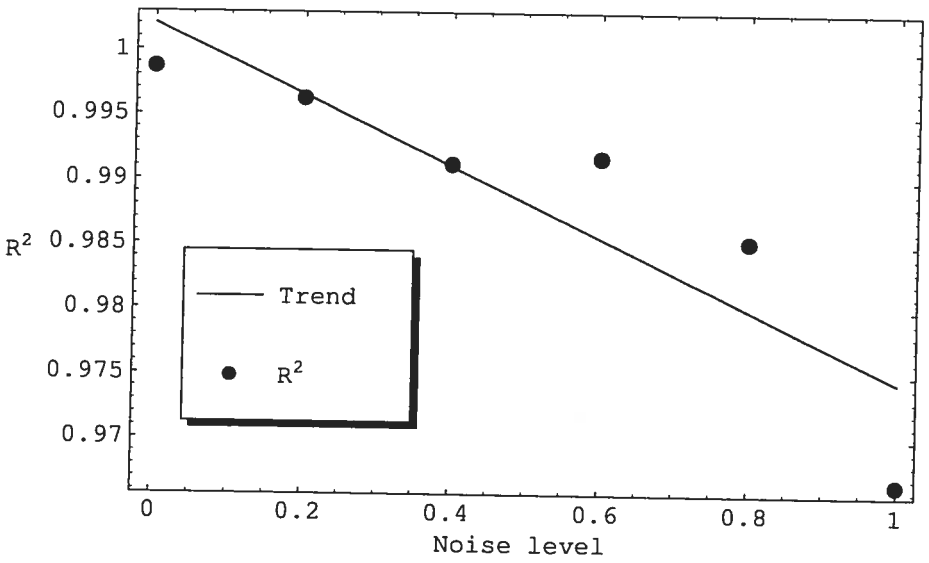

Figure 4. Evolution of the reconstructed scaling parameter over different noise level. The regression coefficient between the average reconstructed and simulated scaling parameter is plotted against increasing noise level. The average is done over the 25 *subject models*. As expected, the trend of the regressions decreases as the noise level increases.

diameter around the reference points along the coronaries. Figure 4 represents the variation, over increasing noise level, of the regression coefficient between the simulated and the average reconstructed scaling parameter. It can be seen that R^2 goes from 99.8% to 96.6% as the noise level goes from 0 to 1 cm.

3.2. Clinical cases

The application of our heart motion reconstruction method on clinical cases was similar to the simulated cases except for certain specificities.

During a coronarography examination, the injection of the contrast agent bolus is done separately for the left and right coronary angiogram. To use both the LCA and RCA together, the images must be registered. Since no registering was done with our clinical case angiograms, only the LCA was used when reconstructing the scaling parameter.

With clinical cases, the scaling parameter responsible for the heart contraction, is unknown, hence it cannot be directly compared to the reconstructed scaling parameter. To get an estimation of the clinical case scaling parameter we used instead, the ejection fraction measured by a physician for each case during a ventriculography examination. Using a simple *mathematical contraction model* we were able to linearize the relation between the ejection fraction and the scaling parameter. In our *mathematical contraction model* the heart is represented by an hollow ellipsoid and the pericardium volume is kept constant throughout the contraction cycle. Using rotation, translation and scaling transformation parameters, the reconstruction of the clinical cases heart movement was realized, giving satisfactory results for 5 out of 10 cases. In two cases, the scaling was reversed : instead of having a concave curve shape, contraction followed by dilation, the curve was convex. In three other cases, the scaling curve follows an erratic pattern. To alleviate such problems, a second round of reconstructions was undertaken by dropping the rotation and translation parameters, using only the scaling parameters.

Figure 5 represents the relation between the (minimum) reconstructed scaling parameter and the ejection fraction with the theoretical trend based on our heart contraction mathematical model. By linearizing the relation between the reconstructed scaling parameter and the measured ejection fraction, using a *mathematical contraction model*, we were able to obtain a correlation of $R^2 = 57\%$ with $P < 1\%$.

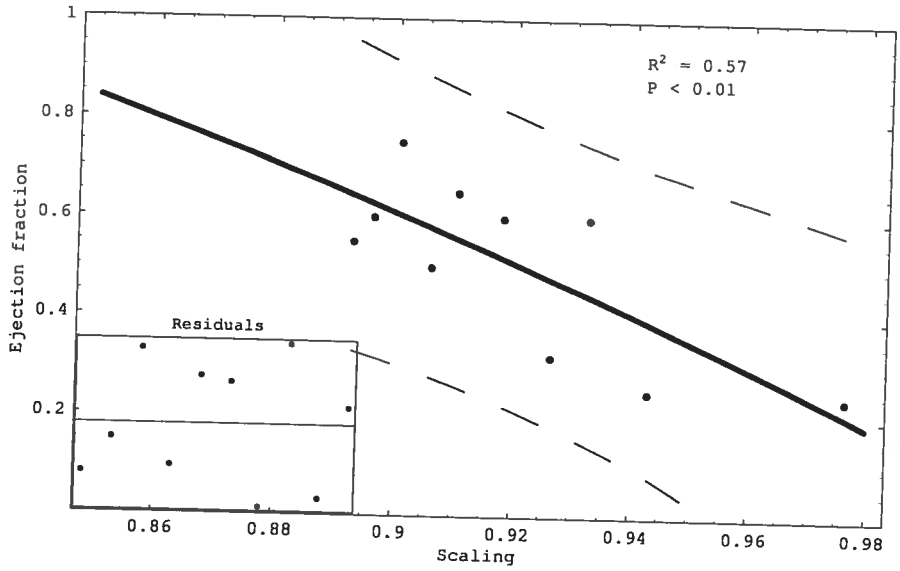

Figure 5. Correlation between the reconstructed scaling parameter and the ejection fraction. The thick line represents the relation according to our *mathematical contraction model.* Dashed lines delimit the 95% confidence region.

4. DISCUSSION

4.1. Comparison between weak perspective and full perspective projection model

When doing a reconstruction of the isotropic scaling parameter, the minimization process is based on the projection of our heart model, Sect. 2.4. Two geometric projection models were used: the full perspective camera model (FP) or pinhole model and the weak perspective camera model (WP). Contrary to FP, in WP the location of projected points do not depends on individual depth coordinates but rather on the average depth information. Even if this is an approximation, the WP has the advantage of linearizing the FP equation. Besides, when reconstructing the heart movement in FP using rotation, translation and scaling, the depth translation parameter $\mathbf{T}_z$ must be set to zero. This is because translating a point away or toward the center of projection gives the same result than applying a decreasing or increasing scaling factor respectively. For these reasons, the WP projection model was preferred over the FP model.

4.2. Heart contraction simulation

As expected the correlation, between the scaling factor used for the simulated contraction and the one obtained by the reconstruction, decreases with the noise level, from $R^2 = 99.8\%$ to 96.6% ($P < 1\%$), see Fig. 4. The average of the scaling parameters over the 25 *subject models* might explains partially the high correlation even in the presence of relatively high noise, the average smoothing out individual variations.

Since only the LCA was considered in the clinical cases, we tested the effects of reconstructing from the LCA versus RCA-LCA. Without adding noise, the correlation between the average reconstructed scaling parameter and the simulated target is still high ($R^2 = 98\%, P < 1\%$) when using only the LCA, compared to $R^2 = 99.8\%$ ($P < 1\%$) when using the LCA-RCA.

4.3. Clinical cases

The difficulties encountered during the reconstruction process undertaken from clinical cases when using all 6 parameters from rotation, translation and scaling transformations might be explained by the misregistration of reference points. In some cases, anatomical landmarks were difficult to identify. It might also be noted that the spatial distribution of reference points is more concentrated near the root of the arterial tree than the apex, see Fig. 1, probably creating an ill-conditioned reconstruction process.

During the reconstruction process, each of the 6 parameters have the same weight. Although constraints were imposed, for example rotations were limited to $\pm\pi/8$ radians and the scaling parameter was positive, no a priori information on the behavior of the parameters was given. In specific case, it has been observed that a shift in one parameter, inverse the scaling curve until the system finds a new stable configuration. As if, at certain moments a parameter becomes dominant in the minimization process. This is what happens when over-parameterizing a model. In such cases, it is well known that reducing the number of parameters could improve the conditioning of the problem and the robustness of the solution, this is why we focused on the scaling parameter afterward. Since the minimization process depends on the center of contraction, by placing it in the left ventricle slightly shifted toward the apex of the heart, in concomitance with Potel *et al.*,[3,20] we obtained the best scaling curve shapes and best relation between the scaling parameter and ejection fraction, Fig. 5. Although Potel *et al.* found that using a moving center of contraction best describes the radial heart wall motion, we used a fixed center of contraction.

5. CONCLUSION

We have presented a model-based method to recover a scaling index, similar to the ejection fraction index, from single-plane coronary cineangiograms. The method relies on the minimization of the RMS distances from reference points along the main arteries and the projected points of a model.

In simulations, our method recover more than 95% of the original contraction, expressed as a scaling parameter. Using 10 clinical cases, we compared our contraction index to the measured ejection fraction and found a coefficient of determination of 57% ($P < 1\%$).

Difficulties were encountered while reconstructing the 3D heart contraction of clinical cases. Some solutions might come from the use of more reference points on the epicardium with more LCA branches and/or a registered RCA. A moving-center-of-contraction model could also mimic more accurately the heart contraction. However, we believe that more complex deformation models (e.g. using torsion amongst others) would probably not be suitable because of the poor conditioning of this problem.

ACKNOWLEDGMENTS

The authors thank Dr. Jacques Lesperance from the Montreal Heart Institute, for his help in the selection of the clinical case images. The authors express their gratitude to Dr. J. Theodore Dodge Jr for having so generously shared his data used in the model elaboration.

REFERENCES

1. J. T. Dodge Jr, B. G. Brown, E. L. Bolson, and H. T. Dodge, "Intrathoracic spatial location of specified coronary segments on the normal human heart. applications in quantitative arteriography, assessment of regional risk and contraction, and anatomic display." *Circulation*, vol. 78, no. 5, pp. 1167–80, 1988.
2. J. T. Dodge, B. G. Brown, E. L. Bolson, and H. T. Dodge, "Lumen diameter of normal human coronary arteries. influence of age, sex, anatomic variation, and left ventricular hypertrophy or dilation," *Circulation*, vol. 86, no. 1, pp. 232–46, 1992.
3. M. Potel, S. MacKay, J. Rubin, A. Aisen, and R. Sayre, "Three-dimensional left ventricular wall motion in man. coordinate systems for representing wall movement direction." *Investigative Radiology*, vol. 19, no. 6, pp. 499–509, Nov-Dec 1984.
4. R. Medina, M. Garreau, C. Navarro, J. Coatrieux, and D. Jugo, "Reconstruction of three-dimensional cardiac shapes in biplane angiography: a fuzzy and evolutionary approach," in *Computers in Cardiology 1999. Vol.26 (Cat. No.99CH37004) p. xxiii+724*, vol. 26, Computers in Cardiology 1999. Vol. 26. IEEE; Piscataway, NJ, USA, 1999, pp. 663–6.
5. G. Shechter, F. Devernay, E. Coste-Maniere, A. Quyyumi, and E. McVeigh, "Three-dimensional motion tracking of coronary arteries in biplane cineangiograms," *Medical Imaging, IEEE Transactions on*, vol. 22, no. 4, pp. 493– 503, April 2003.

6. J. Messenger, S. Chen, J. Carroll, J. Burchenal, K. Kioussopoulos, and B. Groves, "3D coronary reconstruction from routine single-plane coronary angiograms: clinical validation and quantitative analysis of the right coronary artery in 100 patients," *International Journal of Cardiac Imaging*, vol. 16, no. 6, pp. 413–27, Dec. 2000.
7. S. J. Chen and J. D. Carroll, "3-D reconstruction of coronary arterial tree to optimize angiographic visualization," *IEEE Trans Med Imaging*, vol. 19, no. 4, pp. 318–36., 2000.
8. C. Blondel, R. Vaillant, F. Devernay, G. Malandais, and N. Ayache, "Automatic trinocular 3D reconstruction of coronary artery centerlines from rotational X-ray angiography," in *Proceedings of 16th International Symposium on Computer Assisted Radiology and Surgery CARS 2002.* Springer-Verlag, 2002, pp. 832–837.
9. T. Nguyen and J. Sklansky, "Reconstructing the 3-D medial axes of coronary arteries in single-view cineangiograms," *IEEE Transactions on Medical Imaging*, vol. 13, no. 1, pp. 61–73, 1994.
10. T. Saito, M. Misaki, K. Shirato, and T. Takishima, "Three-dimensional quantitative coronary angiography." *IEEE Transactions on Biomedical Engineering*, vol. 37, no. 8, pp. 768–77, 1990.
11. K. Hoffmann, A. Sen, L. Lan, K. Chua, J. Esthappan, and M. Mazzucco, "A system for determination of 3d vessel tree centerlines from biplane images." *International Journal of Cardiac Imaging*, vol. 16, no. 5, pp. 315–30, 2000.
12. F. H. Netter, *Heart : a compilation of paintings on the normal and pathologic anatomy and physiology, embryology, and diseases*, F. F. Yonkman, Ed. The Ciba collection of medical illustrations, 1969, vol. 5.
13. M. Garreau, J. Coatrieux, R. Collorec, and C. Chardenon, "A knowledge-based approach for 3-D reconstruction and labeling of vascular networks from biplane angiographic projections," *IEEE Transactions on Medical Imaging*, vol. 10, pp. 122–31, 1991.
14. P. Windyga, M. Garreau, M. Shah, H. Le Breton, and J. Coatrieux, "Three-dimensional reconstruction of the coronary arteries using a priori knowledge," *Medical & Biological Engineering & Computing*, vol. 36, pp. 158–64, 1998.
15. C. Chalopin, G. Finet, and I. E. Magnin, "Modeling the 3D coronary tree for labeling purposes," *Medical Image Analysis*, vol. 5, no. 4, pp. 301–315, 2001.
16. Y. Kong, J. Morris, Jr, and H. D. McIntosh, "Assessment of regional myocardial performance from biplane coronary cineangiograms." *Am J Cardiol*, vol. 27, no. 5, pp. 529–37, May 1971.
17. D. Sherknies and J. Meunier, "A numerical 3D coronary tree model," in *Proceedings of 16th International Symposium on Computer Assisted Radiology and Surgery CARS 2002.* Springer-Verlag, 2002, pp. 814–818.
18. J. D. Foley, A. van Dam, S. K. Feiner, and J. F. Hughes, *Computer Graphics Principles and Practice.* Addison-Wesley, 1996.
19. E. Trucco and A. Verri, *Introductory Techniques for 3-D Computer Vision.* Prentice Hall, 1998.
20. M. Potel, J. Rubin, S. MacKay, A. Aisen, J. Al-Sadir, and R. Sayre, "Methods for evaluating cardiac wall motion in three dimensions using bifurcation points of the coronary arterial tree." *Investigative Radiology*, vol. 18, no. 1, pp. 47–57, Jan-Feb 1983.

GLOSSAIRE

ANGIOGRAPHIE: Exploration radiographique du réseau vasculaire par injection d'un produit de contraste, opaque aux rayons X.

ANGIOGRAMME: Image résultant d'un examen angiographique.

CD: Artère coronaire droite.

CINÉANGIOGRAPHIE: Examen angiographique enregistré numériquement ou sur pellicule, à une fréquence pouvant atteindre 25 images par seconde.

CORONAROGRAPHIE: Angiographie appliquée aux artères coronaires.

CX: Artère coronaire circonflexe.

FANTÔME: Modèle composé de matériaux différents permettant de générer des images de diverses modalités : à rayons X, à ultrasons, etc.

IVA: Artère coronaire interventriculaire antérieure.

IVUS: *Intra Vascular UltraSound*, ultrasonographie endovasculaire, échographie endovasculaire. Caméra (transducteur) fixée à l'extrémité d'un cathéter et insérée à l'intérieur des artères. De modalité ultrasonore, les images renseignent sur le diamètre et la composition des vaisseaux.

VENTRICULOGRAPHIE: Exploration radiographique des ventricules par injection d'un produit de contraste, opaque aux rayons X.